KU LEUVEN

FACULTY OF SCIENCE

Investigating ^{225}Ac Production at CERN-MEDICIS:

Extraction Yield Estimation and Sample Purity

Max KEPPENS

Supervisor: Prof. T.E Cocolios
Institute for nuclear and radiation physics

Mentor: J.D. Johnson
Institute for nuclear and radiation physics

Thesis presented in
fulfillment of the requirements
for the degree of Master of Science
in Physics

Academic year 2023-2024

Preface

I was always fascinated about how physics could unravel the workings of nature, which is the reason why I studied physics at KU Leuven. In my third bachelor's year, professor Cocolios used a figure in his presentation, showing the potential of what physics can do in the fight against cancer. This started my interest in medical physics, which is why I chose to study nuclear physics in the master. Ironically enough, this figure was from the famous research which showed the clinical potential of ^{225}Ac, which is the topic of my thesis.

I wanted to thank professor Cocolios for providing the opportunity to work on this subject and to start my interest in this field. During the last year, I have learned a lot about the medical side of physics and the professional setting around it. I am grateful for the opportunity to have attended my first conference, where the potential in this field became even clearer to me.

Secondly, I wanted to thank my mentor Jake Johnson for guiding me throughout this thesis. Even though he had to finish his PhD in the same year, he still offered to help and give advice whenever I needed. This ranged from the understanding of the results to learning the very frustrating coding language ROOT. I learned a lot about the complexity of the separation process, the potential of ^{225}Ac and the life of an experimental physicist. This guidance definitely contributed to the nice experience of specializing myself into a subject. On top of this, I wanted to show gratitude to include me in the research project which will result in the very first paper with my name on it.

Contribution statement

I would like to thank the team at CERN-MEDICIS for their support in conducting the experiments that provided the crucial data and radioactive samples for my thesis. Special thanks go to C. Bernerd, F. Bruchertseiffer, M. Deseyn, C. Duchemin, L. Lambert, R. Mancheva, R. Rossel, and T. Stora.
The experiments in the ASET chamber were carried out under the guidance of J. D. Johnson, who also developed the correction factors for geometric efficiency, taking into account the 'ping pong' effect.
I am grateful to professor T. E. Cocolios and J. D. Johnson for their valuable feedback on my thesis and for their guidance and support throughout this academic year.

Summary

This thesis is focused on the separation process of actinium-225, a necessary step in the production method of high energy proton irradiation of a thorium-based target. ^{225}Ac is a promising candidate in targeted alpha therapy, which provides an alternative and selective way to fight the devastating disease of cancer. However, clinical research is rendered difficult due to insufficient supply of this medical isotope. Alternative pathways are considered to upscale the production of ^{225}Ac, but further research is needed to overcome the challenges associated with it. In the production method of high energy proton irradiation, many different isotopes are created in the target, including the long-lived isotope ^{227}Ac, which necessitates a separation process. This can happen via radiochemistry, but this method does not provide isotopic selectivity. The typical activity of the long-lived ^{227}Ac in the medical samples would cause problems for hospitals in terms of facility licensing and decommissioning, product licensing and waste disposal. This disadvantage requires the need of a mass separation process, where isotopes are filtered based on their mass-to-charge ratio. It is this particular step in the production process that is investigated in this work. Two separate analyses were performed in order to investigate the feasibility of the production method.

The first part of the thesis revolves around the ion beam current data of four experimental runs performed at CERN-MEDICIS. This current was measured at different parts in the experimental setup and can be retrieved in real-time during collection. The data are used to estimate the collected activity on the foils, which could serve as a real-time assessment of the activity during experiment. On top of this, the different sources of the collected ^{225}Ac could be separately identified, which can come from either the decay of the parent nucleus ^{225}Ra on the foil or directly collected ^{225}Ac from the ion beam. This analysis showed good agreement between the measured and estimated values, but showed a consistent underestimation of the activity. On top of these estimations, the influence of the laser ionization was investigated. Lasers are directed at the extracted isotopes of the target, which selectively ionize the element of interest. This results in a higher extracted amount of ^{225}Ac, which results in a higher collected ion beam current. By regularly blocking the laser, a drop in the collected current could be observed. This allowed to investigate the influence of the ionizing lasers by assessing the laser enhancement and the gain in activity due to the lasers alone. The laser enhancement is defined as the ratio of the collected activity of ^{225}Ac when the laser was on and blocked. The results of this work suggested a factor of approximately 2.

The second part of the thesis is a purity analysis on the collected activities of two runs performed at CERN-MEDICIS. In particular, the activity of ^{227}Ac served to calculate the separation enhancement factor. This factor signifies the ability to separate the long-lived isotope ^{227}Ac, which is defined as the ratio of ^{225}Ac to ^{227}Ac before and after separation. A separation factor of 150 ± 14 and 646 ± 59 were found for the two runs, where the large

difference is due to experimental conditions. Still, both runs enabled to suppress the activity of ^{227}Ac enough for medical purposes.
In conclusion, the two experimental runs performed at CERN-MEDICIS fulfilled the purpose of suppressing ^{227}Ac, although a large variability is seen due to experimental conditions. This makes the production method suitable for ^{225}Ac production, but the extraction efficiency should increase to reach global demand. The extraction efficiencies analyzed in this work were approximately 1% for ^{225}Ac. For its parent nucleus, ^{225}Ra, the efficiencies were approximately 20-40%. The typical higher efficiency of the latter is due to the lower boiling point and more efficient surface ionization. These values emphasize the need for further research and a deeper understanding of the extraction process is needed. By investigating the ion beam current data measured in the setup, an attempt is made to extract information which could benefit the insight in the conditions met of collection runs. Good agreement of the results are found w.r.t. the measured values of gamma spectroscopy, but a systematic underestimation is made.

Summary for general audience

According to the World Health Organization, cancer ranks among the top causes of death globally [1]. With almost 20 million new cancer cases and a mortality rate of 48%, the significance of further research is highlighted to fight this devastating disease. In the last century, it was realised that radioactivity could be used as an efficient tool to kill cancer cells. Radioactivity is the phenomenon where an unstable isotope emits a particle. This is a natural process where the resulting isotope becomes energetically more stable. In targeted radionuclide therapy, radioactivity is used to cure cancer. This is done by inserting the radioactive isotopes into the body, which are linked to a targeting molecule. This molecule finds the cancer cells via biological pathways, whereafter the radioactive isotopes damage the cancer cells by emission of a particle. As the isotope is in close proximity of the cancer cells, severe side effects are avoided as the damage to healthy cells is kept to a minimum. However, not all unstable isotopes can be used for this therapy, as certain properties should be met since it is inserted into the human body. Actinium-225 is a promising candidate for this therapy, especially since it decays via alpha emission. This type of decay has a higher damaging potential than other decay channels, which makes it promising to kill cancer cells. The use of alpha decay in this therapy is referred to as targeted alpha therapy. Research has shown great potential using ^{225}Ac, but before this medical isotope can be used commercially , production scale should be increased. Actinium-225 is an isotope which does not naturally occur on earth, which necessitates the production via different pathways. One pathway in particular is examined in this work, where a beam of high energy protons are directed onto a target material. These protons induce various nuclear reactions, which results in the production of new isotopes, under which ^{225}Ac. In order to make a pure medical product, separation processes are needed. This can be done effectively via radiochemistry. However, the big disadvantage is that no isotopic selectivity is reached in this method. As besides ^{225}Ac, ^{227}Ac is produced due to these nuclear reactions induced by the protons, a solution has to be found for this problem. This is because ^{227}Ac is a long-lived radioactive isotope, which is unwanted in a medical product. This is why mass separation is performed after irradiating the target with protons. Accelerating ions through a magnet bends the ion beam according to their mass-to-charge ratio. By choosing the right magnetic field strength, the isotope of interest can be filtered. In this work, this separating step of the production process is analyzed for two purposes: to gain a deeper understanding of the process and to check purity of the collected product. For the first part, results based on the ion beam current measured on the collection foils gave good agreement if compared to measured values, but a consistent underestimation is observed. An hypothesis is formed and can be checked by further research. The second part of the analysis in this work suggested that the separation ability suffices for medical endpoints. This indicates that the production pathway considered in this thesis could serve as a pathway to upscale the production of ^{225}Ac. However, further research is needed to reach this goal, as the separation technique is complex.

List of Acronyms and Symbols

Acronyms

ADC	Analog to Digital Converter
ARIEL	Advanced Rare Isotope Laboratory
ASET	Alpha Setup Decay Spectroscopy Chamber
BR	Branching Ratio
CT	Computed Tomography
DAMP	Damage-Associated Molecular Patterns
DNA	Deoxyribonucleic Acid
EOB	End of Bombardment
EOC	End of Collection
FC	Faraday Cup
FDA	Food and Drug Administration
FWHM	Full Width at Half Maximum
HPGe	High Purity Germanium
IKS	Institute for Nuclear and Radiation Physics
IP	Ionization Potential
ISOL	Isotope Separation on Line
ISOLDE	Isotope Separation on Line Device
JRC	Joint Research Center
KUL	Katholieke Universiteit Leuven
LANSCE	Los Alamos Neutron Science Center
LET	Linear Energy Transfer
linac	Linear Accelerator

MCA	Multi Channel Analyzer
MEDICIS	Medical Isotopes Collected from ISOLDE
MELISSA	MEDICIS Laser Ion Source Setup At CERN
MRP	Mass Resolving Power
PAM	PicoAmpereMeter
PET	Positron Emission Tomography
PIPS	Passivated Implanted Planar Silicon
PSB	Proton Synchrotron Booster
PSMA	Prostate-Specific Membrane Antigen
RBE	Relative Biological Effectiveness
RIAR	Russian Institute of Radionuclides and Radiopharmaceuticals
RIMS	Resonance Ionization Mass Separation
SPECT	Single-Photon Emission Computed Tomography
spf	Separation Enhancement Factor
SRIM	Stopping and Range of Ions in Matter
TAT	Targeted Alpha Therapy
TRIUMF	TRI-University Meson Facility
TRT	Targeted Radionuclide Therapy
US	United States

Symbols

α	Crystal ball parameter (when tail starts)
χ^2_ν	Chi-squared reduced
ΔH	Activation enthalpy of diffusion
ϵ	Efficiency
η	Surface ionization efficiency
λ	Decay constant
μ	Mean
ν	Degrees of freedom

ϕ	Work function
Φ_p	Plasma potential
σ	Standard deviation, Statistical weight
A	Activity
B	Magnetic field strength
D	Diffusion constant
d	Separation distance
D_0	Pre-exponential factor
E	Energy
e	Laser enhancement, charge of electron
E_{act}	Activation energy of desorption
I	Current
k_b	Boltzmann constant
m, M	Mass
N	Amplitude peak, amount of radionuclides
n	Crystal ball parameter (determines length tail)
q, Q	Charge
r	Rate, radius
T	Temperature
t	Time
v	Velocity
W	Ionization potential
W^*	Effective ionization potential

List of Figures

List of Tables

Contents

1. Introduction

In the modern world we live in, cancer is one of the leading death causes across the world. With almost 20 million new cancer cases reported globally in the year of 2022 and a mortality rate of 48%, these statistics emphasize the significance to continue research to combat this devastating disease [1]. In response to fight this challenge, several tools exist for physicians to approach a diagnosed patient, as illustrated on figure 1.1. In early stages, the primary cancer (and large metastases) can be treated locally with surgery or local external irradiation. At later stages, cancer often metastasizes, spreading throughout the body and rendering local treatments ineffective for complete removal. For these patients, a systemic treatment is needed to fight the cancer, using substances that travel through the bloodstream, reaching and influencing cells all over the body. With chemotherapy, chemotherapeutic drugs are administered intravenously or orally, inhibiting the cell division process all over the body [2]. As cancer cells have the characteristic of growing uncontrollably, this therapy is more effective for cancer cells compared to normal cells. However, healthy cells are still affected by the chemotherapeutic drugs, which leads to severe side effects such as hair loss, nausea and fatigue [3]. Resistance to chemotherapy can arise due to various reasons such as genetic mutations and activation of cellular pathways involved in drug efflux or DNA repair mechanisms [2] [4]. Targeted radionuclide therapy (TRT) offers a promising alternative, giving a more selective treatment with fewer side effects. This therapy makes use of the concept of radioactivity, a natural process by which unstable atomic nuclei lose energy by emitting radiation. In TRT, radioactive isotopes, which are coupled to a targeting molecule, are inserted in the human body and reach the tumor via biological processes, delivering a local therapeutic dose of ionizing radiation that damages the cancer cells. Different decay modes can be used in this selective therapy, but alpha emission holds high potential due to its higher linear energy transfer (LET), which signifies the local energy deposition per unit path length. TRT using alpha emitters specifically, is referred to as targeted alpha therapy (TAT).

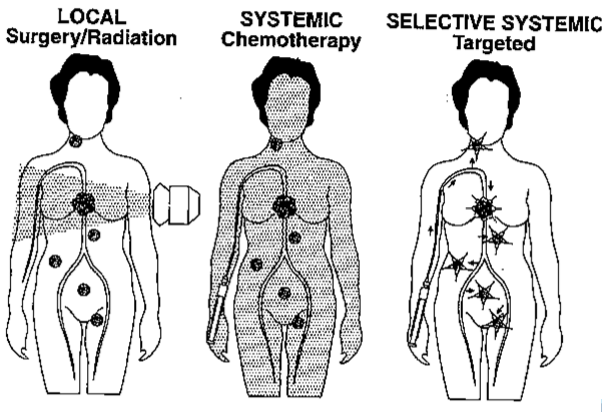

Figure 1.1: Different approaches of curing cancer: surgery or external irradiation (left), chemotherapy (middle) or target radionuclide therapy (right). The black dots represent cancer lesions. Figure taken from [5].

A promising candidate for the selective alpha therapy is ^{225}Ac, an isotope with a half-life of 9.92 days and four alpha emissions in its decay chain, which makes the radioisotope highly cytotoxic - the quality to damage cells. The biological aspects of the therapy are discussed in chapter 2, as well as the clinical relevance of ^{225}Ac. Multiple trials, both in vitro and in vivo, have been undertaken with ^{225}Ac, showing promising clinical outcomes [6]. However two main factors render the ongoing pre-clinical/clinical TAT research for this isotope difficult: production capability and contamination of co-produced isotopes. Even now, when ^{225}Ac is not yet used in commercial clinical applications, production rate does not meet global demand. Currently the majority of the production comes from ^{229}Th generators, but other production pathways are and should be investigated to meet future global demand [7]. Details on the production of ^{225}Ac can be found in chapter 3, explaining the origin of the ^{229}Th generators and the mechanics and potential of other pathways. One alternative and promising pathway discussed is proton irradiation of thorium-based targets. Although research is still ongoing to increase production yields for ^{225}Ac generated in Th-based targets, certain experiments have already been conducted. These findings indicate the potential for producing over 10 GBq annually in-target at isotope production facilities like RIAR (Russia), LANSCE (USA), ARIEL (Canada), and CERN-MEDICIS (Europe) [6]. However, by irradiating a target with high energy protons, a span of other radioisotopes are produced, including the long lived ^{227}Ac ($t_{1/2} = 21.772$ y), which necessitates a separation process. This can be either done by direct radio-chemical separation or by a combination of mass separation and radio-chemical separation. The first method shows an efficiency of 85-98% in recent studies, but shows no isotopic selectivity [6]. While the ^{227}Ac contaminant in the final drug is not expected to reduce its efficacy or cause additional toxicity to patients, it could be problematic in terms of facility licensing and decommissioning, product licensing and waste disposal, where in Europe the clearance level is 10 Bq/kg and the exemption level is 1 kBq [8] [9] [10] [6]. This is why in Europe, the separation process should involve mass separation of the isotopes in the irradiated target, which is isotope selective. This technique starts with heating the radioactive target, which creates an atomic vapour of the produced isotopes escaping from the target. These isotopes migrate to the ion source, where ionization is induced to extract and produce an accelerated ion beam. Ionization at CERN-MEDICIS (MEDical Isotopes Collected from ISolde), a facility dedicated to the production of novel medical radioisotopes, occurs at the moment via two methods: surface ionization and resonance laser ionization [11]. In surface ionization, isotopes

lose an electron upon contact with the heated walls of the ion source. The second method involves tuning the laser frequencies in order to selectively ionize Ac, where the energy of the photons are used to emit an electron. The ions are then accelerated across a potential to form an ion beam. These ions are mass-separated using a dipole magnet, based on the mass-to-charge ratio of the isotope of interest. This technique is referred to as RIMS, standing for Resonant laser Ionization and Mass Separation. More information about this technique can be found in the beginning of chapter 4. An image of the mass separator can be seen on figure 1.2. Thanks to this method, the co-produced ^{227}Ac (typically $0.15 - 0.20\%$ activity vs ^{225}Ac) is suppressed, making a more pure end product which can be used for medical endpoints [12].

Figure 1.2: A picture of the CERN-MEDICIS experimental setup, where medical radioisotopes are extracted from a target and filtered using mass separation. Image taken from [13].

In this study, two aspects of the separation technique are analyzed: determining collected activity using data of the ion beam current on the sample foils during isotope collections and assessing the purity of collected samples concerning the contaminant ^{227}Ac. Chapter 4 examines four experimental runs conducted at CERN-MEDICIS, using the data obtained during collection. PicoAmpèremeters (PAM) measure the current at different parts of the setup coming from the ion beam, which give guidance and understanding of the collected isotopes during collection. The goal of this analysis was to obtain viable information which could benefit future extraction runs during and after collection. One of the aims was to develop an alternative method for evaluating the activity on collection foils by analyzing the ion beam current, which is discussed in section 4.4. Currently, foil activity is assessed using gamma spectrometry after collection. This new estimation can validate the gamma spectrometry measurements and can also provide a means to monitor collected activity in real-time. This could be advantageous in the future when high yields of actinium are produced and time efficiency becomes crucial for collection on different foils. In addition to activity estimation, a detailed analysis is conducted on the effects of resonant laser ionization in section 4.5. Lasers selectively ionize actinium, leading to more actinium extraction from the ion source. By analyzing the ion beam current on the foils, the laser enhancement and activity gain can be estimated. This analysis offers a qualitative assessment of the laser ionization and provides insights into its temporal evolution.
The second part of this study is dedicated to analyzing the purity of collection foils coming from two experimental runs at CERN-MEDICIS in chapter 5, more specifically regarding the

long-lived contaminant ^{227}Ac. As it is difficult to analyze the presence of ^{227}Ac right after collection due to the high background of isotopes, the foils were kept in isolation at KU Leuven [10]. After approximately 30.04 and 27.82 half-lives of ^{225}Ac, the ^{227}Ac contaminant should remain detectable, while ^{225}Ac will be suppressed by factors of 9.07×10^{-10} and 4.21×10^{-9}, respectively. This enables the determination of the original activity of the collected contaminant, allowing for the calculation of the separation enhancement factor of the technique, which is given by dividing the ratio of ^{225}Ac to ^{227}Ac after and before extraction. This value provides insights into the technique's separation capability, which is the goal of this method. The calculated separation factor can also be compared with other quantification methods to verify accuracy.

Both parts of this study provide a two-step determination of the overall feasibility of this production pathway. The purpose of the separation process is to suppress the activity of contaminants to make the radioactive end-products useful for patient administration. If this condition is met, production rate should increase to meet global demand, which can only happen by providing information from the data to deepen our understanding of the extraction process. In chapter 6, a conclusion is made regarding the future of this separation process based on the results given in this thesis.

2. Role of ^{225}Ac in radiation therapy

In this chapter, clinical and biological aspects of targeted radionuclide therapy will be explained. First, different components of TRT will be explained in section 2.1. The properties of radiopharmaceuticals will be explored, detailing how these substances are designed to interact with cancerous cells via specific physiological processes. Additionally, the fundamental principles of the interaction of radiation with matter will be examined, highlighting its significance in the context of medical therapy. In section 2.2, the promising subcategory TAT of TRT is discussed, explaining why alpha particles can be beneficial for therapy. Afterwards in section 2.3, the necessity for further research into ^{225}Ac is mentioned, by showing the clinical relevance of ^{225}Ac but also the challenges for the safe use of the α-emitting isotope.

2.1 Targeted radionuclide therapy

In the past century, there has been significant interest in radionuclide therapy since the discovery of iodine treatment for the thyroid, leading to extensive research efforts aimed at creating, refining, testing, and clinically evaluating numerous innovative radiopharmaceuticals [14]. As previously mentioned, TRT makes use of radiopharmaceuticals, which reach the tumor via a biological pathway and irradiate the cancer cells locally, including metastasis sites. This therapy is capable of specifically targeting cancer cells with cytotoxic radiation while minimizing harm to neighboring healthy tissues. The radiopharamceuticals can be administered to the body via different routes, primarily through intravenous administration [15]. They consist of 3 major parts: a radioisotope, a chemical linker and a carrier molecule (see figure 2.1). The radioactive isotopes or radioisotopes are a crucial element of the treatment. By decaying at the site of interest, the radiation can induce damage via direct or indirect interactions. The selected radioisotope is then coupled to a carrier molecule with a chemical linker or chelator. The carrier molecule, also named the vector molecule or targeting molecule, has the role of delivering the radioisotope to tumor sites, which are often characterized by receptors that are overexpressed. The overexpression increases the probability that the targeting molecule binds to this cell. The vector is responsible for the selective nature of the therapy and can be a variety of substances, ranging from peptides and proteins to nanoparticles or cells [15]. It is thus important to diagnose the disease in advance to discern the overexpression of the target protein of the cancer. For instance, in prostate cancer, there is an overexpression of Prostate Specific Membrane Antigen (PSMA). By employing carrier molecules designed to target PSMA, radiopharmaceuticals accumulate specifically at the prostate cancer site.

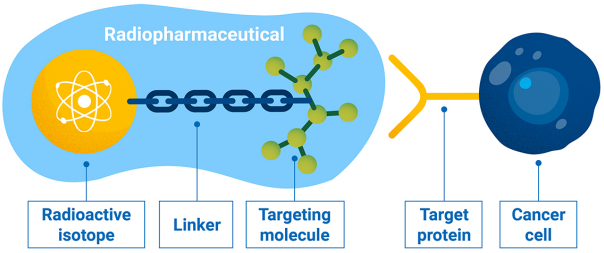

Figure 2.1: Different components of a radiopharmaceutical: radioisotope, chelator and targeting molecule. Image taken from [16].

It is also worth noting that there exist radioisotopes which are target-specific on their own, thus without the need of a carrier molecule. These are also called unconjugated or naked radiophamaceuticals and in contrast to conjugated radiopharmaceuticals, are already decades in clinical practice [17]. A classic example is ^{131}I, which is a β-emitter and is naturally taken up by the thyroid for the production of hormones.

The efficacy of TRT is dependent on the targeting ability of the vector molecule and the radiotoxic nature of the radiation emitted. The choice of radionuclide depends on many factors. Medical radioisotopes must be available at a high standard of purity to prevent the administration of undesired isotopes into the body. Additionally, their chemical properties should be favorable for effective linkage with vector molecules. The physical half-life of the decay should match the in vivo biolocalization and clearance properties of the vector, meaning it should live long enough such that the radiopharmaceutical reaches the tumor. If the half-life is too short, it comes at the cost of irradiating healthy tissue, as a greater fraction of the injected radionuclides decay before reaching the tumor. On the other hand, if the half-life is too long, the activity of the source has a slower decrease, thus prolonging the exposure which may be undesired. A half-life ranging between 1-14 days is often considered optimal [18]. In the context of alpha emitters, it is crucial to consider not only these decay properties of the injected nuclide but also the behaviour of the entire decay chain. The daughter nuclei should decay quickly to confine subsequent radiation to the targeted tumor. The type of emitted particle is thus important to consider. Radionuclides undergoing α emission, β^- emission, and nuclides with a high Auger electron yield are viable candidates for TRT. Gamma emissions are useful for imaging purposes and can be used for dosimetry estimates, however high energy photons do deliver an undesired dose to healthy tissue. For therapeutic purposes, the emitted particle should preferably have a high LET, relative biological effectiveness (RBE) and deliver a localized dose. High LET radiation, such as alpha particles (100 keV/μm), deposits more energy per unit path length, leading to increased damage potential compared to low LET radiation. This translates itself into RBE, which is defined as the ratio between the doses needed from two different radiations to produce equivalent biological damage [18]. The value of the RBE is dependent on the tissue and particle type and allows to compare different therapy modalities with each other. Besides the biological damage induced, the tissue range of the emitted particle should match the size of the tumor or metastases. β^- particles typically have a kinetic energy of $0.3 - 2.3$ Mev, giving rise to a tissue range of $0.5 - 12$ mm in soft tissue, while Auger and C–K electrons are effective exclusively when confined within the nucleus of

the cell due to their low energy [15]. As mentioned above, α particles have a high LET due to their high mass, causing concentrated damage over a few cell volumes ($50-80$ μm, equivalent to $2-10$ cells) [18]. This property is beneficial in radiotherapy, as the desired outcome is to damage the DNA of cancer cells, which can lead to cell death.

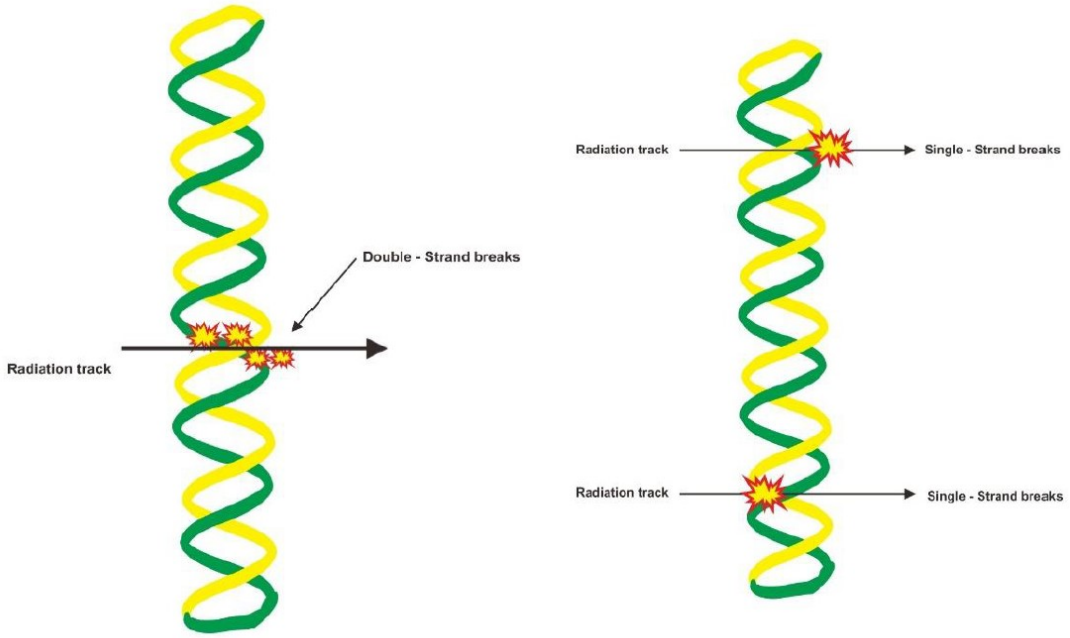

Figure 2.2: **(Left)** High and intermediate LET radiation, such as alpha particles and Auger electrons, induce double-strand breaks in DNA. **(Right)** Radiation with low LET, such as beta particles, causes single-strand breaks in DNA. Image taken from [19].

As previously mentioned, this damage to the DNA can happen via direct or indirect interaction with the emitted particle. Direct interaction with DNA leads to their ionization, resulting in numerous base alterations, single- and double-strand breaks and other modifications of the DNA double helix [20]. Indirect interaction can happen in multiple ways. By interacting with water, free radicals can be formed such as HO° that can react with biomolecules (such as DNA) and indirectly damage the cells. Additionally, cells that are in the proximity of irradiated cells can also undergo modifications, which is known as the bystander effect. Furthermore, the 'abscopal' effect describes antitumorigenic responses in distant metastases [15] [21]. Irradiated cells can release damage associated molecular patterns (DAMPs), which can boost the immune system at distant places [22]. Dependent on the amount of damage inflicted, these interactions to the DNA can impact the intra-cellular mechanisms of the cell which can lead to cell death. However, DNA has the ability to repair itself. Double-strand breaks, which are more abundant in concentrated damage, are generally irreparable, while single-strand damage is typically reparable. All these possible biological damages and repair capability lead to the determination of RBE, which is a crucial factor in dosimetry calculations used to estimate radiobiological effects. It is within this context of optimizing therapeutic impact while minimizing damage to healthy tissue that the choice of radioisotope becomes critical.

2.2 Targeted alpha therapy

The first clinical trial using an alpha emitter dates back to 1997, using ^{213}Bi coupled to the antibody HuM195 targeting myeloid leukemia cells and is the first proof-of-concept for targeted alpha therapy in humans[23] [24]. In 2013, the first alpha emitter ^{223}Ra was approved by the U.S. Food and Drug Administration (FDA) after a phase 3 clinical trial [25] [19]. This unconjugated radiophamaceutical is used for bone pain palliation in prostate and breast cancer patients, targeting high osteoblastic activity in bone metastases. Targeted alpha therapy is a relatively recent approach in cancer treatment, with promising outcomes giving the distinctive properties of alpha particles. The energy dissipation of alpha particles is represented by the Bragg peak, as illustrated in figure 2.3. It shows that the energy dissipated per unit distance increases gradually until a well-defined peak, before rapidly decreasing as the particle comes to rest. This property is different from electrons or photons, allowing a precise targeting of the tumor, as the energy deposition suddenly decreases to zero. A higher initial energy of the alpha particle results in a longer path length, but a lower initial LET [18]. As previously mentioned, typical energies of alpha particles range from 4-8 MeV, which results in an average range in soft tissue around (50-80 μm). Alpha particles are cytotoxic, due to a high probability (20-40%) of that direct interaction with a DNA molecule which results in double-strand breakage [18]. This is in contrast with β^- particles, needing several sub-lethal hits to ensure cell death. The toxicity of alpha particles is thus independent of dose rate based on the double-strand breakage, but due to the short path length, the alpha emission should be in close proximity of the cancer cells [18]. For the deterministic endpoints of targeted therapy, the RBE ranges from 3 to 7, which is of course higher than beta particles.

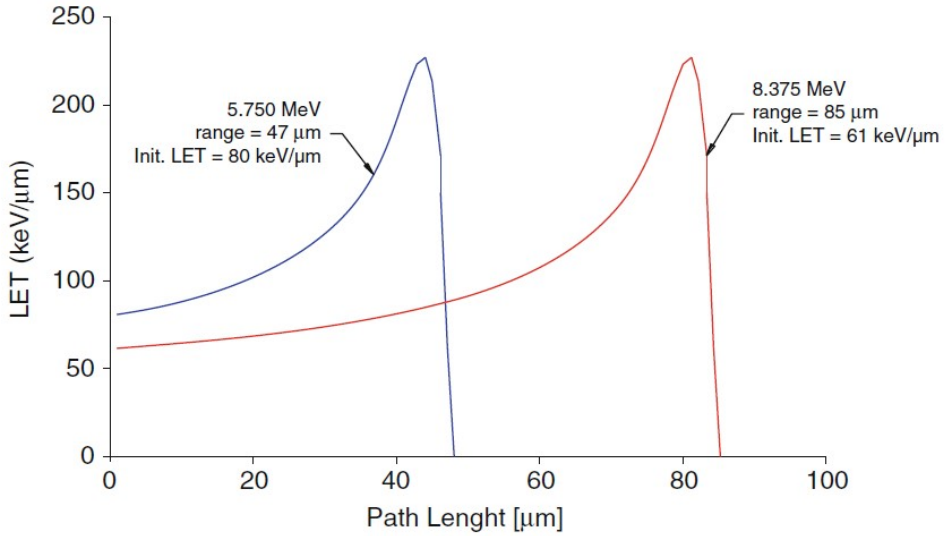

Figure 2.3: The Bragg peak of two alpha particles in a biological system. Different initial energies result in different energy dissipation. Image taken from [18].

In the nuclear chart, over more than 100 radionuclides are identified which decay by alpha emission. However, as mentioned above, the properties of the radionuclide should be practical for radiotherapy, restricting the amount to only a few for therapeutic applications. Table 2.1 gives an overview of the viable candidates for TAT.

Table 2.1: TAT viable isotopes with their respective properties. Amount of clinical trials taken from [26]. *Decays via β^-, but the daughter nucleus decays via α emission.

Isotope	Half-life	Alpha Decay Energy	Clinical trials
Actinium-225	9.920 (3) d	5830 (50.7 %)	16
Astatine-211	7.214 (7) h	5869.5 (41.8%)	5
Bismuth-212	60.55 (6) min	6050.78 (25.13%)	0
Bismuth-213*	45.59 (6) min	-	1
Lead-212*	10.622 (7) h	-	4
Radium-223	11.43 (5) d	5716.2 (51.2%)	124
Terbium-149	4.12 (3) h	3967 (16.7 %)	0
Thorium-227	18.697 (7) d	6038 (24.2 %)	4

2.3 ^{225}Ac clinical relevance

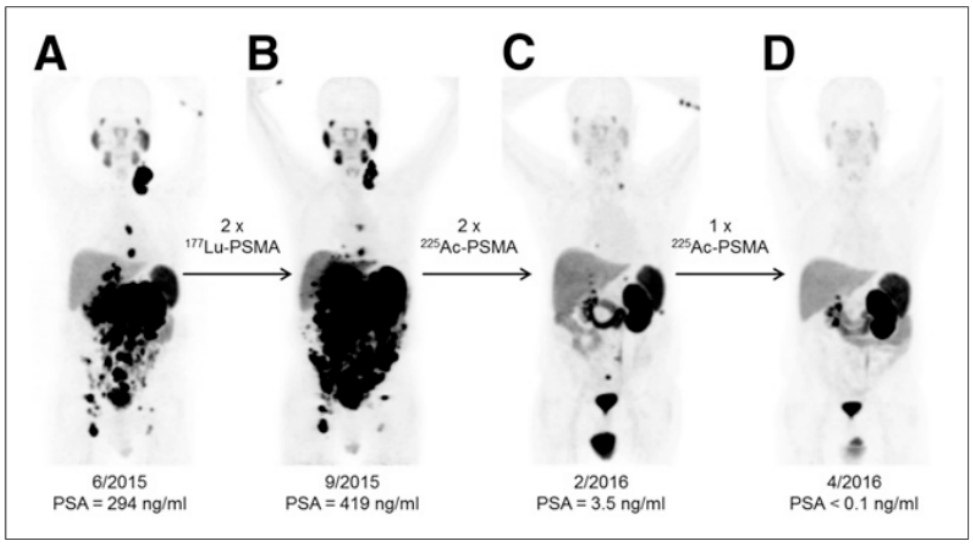

Figure 2.4: PET/CT scans of patient with highly metastasized prostate cancer, showing the initial tumor spread (A) and the response of 2 cycles of β-emitting ^{177}Lu-PSMA-617 (B). Afterwards, restaging after cycles of ^{225}Ac-PSMA-617 showing an impressive response. Figure taken from [27].

As can be seen in table 2.1, ^{225}Ac is listed as a viable option for targeted alpha therapy. ^{225}Ac has a half-life of 9.92 days and decays through a series of six short-lived isotopes before reaching the stable element ^{209}Bi. As can be seen on figure 2.5, the decay chain contains four alpha emissions (Ac-Fr-At-Bi/Po), making ^{225}Ac highly cytotoxic. In 2016, the clinical potential of ^{225}Ac became clear when five patients with highly advanced prostate cancer showed a positive response to ^{225}Ac-PSMA-617 therapy [27]. PSMA-617 is a ligand optimized for PSMA-specific tumor uptake and shows a rapid background clearance and fast kidney excretion, giving clear clinical advantages [28]. In figure 2.4, positron emission tomography (PET)/computed tomography (CT) scans are showed of one of the patients, displaying an ineffective response to the β^- emitter ^{177}Lu, but a clear regression when using 3 cycles of ^{225}Ac

[27]. Nevertheless, it is also important to mention that the therapy came with a side effect called xerostomia (condition of a dry mouth). Besides the salivary glands, the kidney is also considered an organ at risk due to renal toxicity [29]. So even though the drastic reduction of the disease is very promising, research is and should be ongoing to implement the clinical use of ^{225}Ac. Up until now, more than a thousand patients have been treated by ^{225}Ac, which was used against approximately 10 different cancer types [30]. More than a 100 pre-clinical studies have been performed and more than 15 clinical trails have been conducted. These statistics emphasize again the importance and potential of the medical isotope.

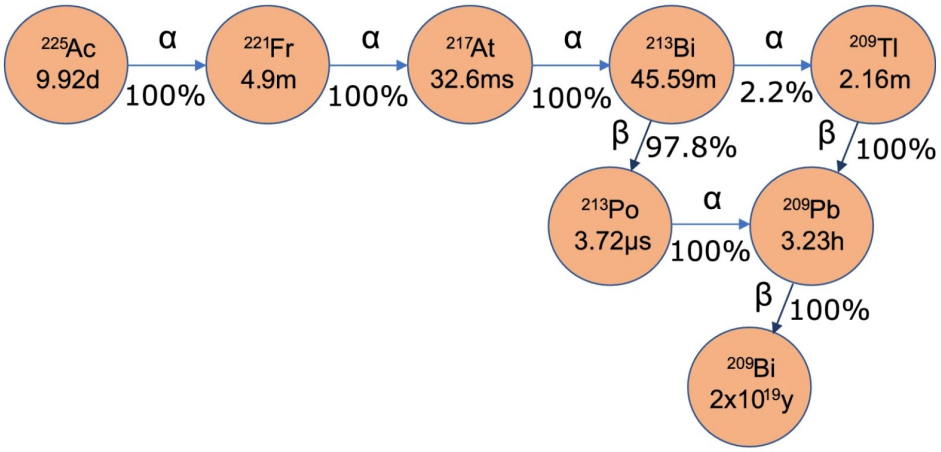

Figure 2.5: Decay scheme of ^{225}Ac, where the half-lives and branching ratios are given. Image taken from [6].

Several challenges are yet to be investigated before the safe use of the medical isotope. One of these challenges concerns the recoil effect from the alpha emission. As the recoil energy (around 100 keV) exceeds the binding energy of the chelator by more than a thousand times, daughter nuclei do not remain conjugated to the carrier molecule [31]. These free α-emitting daughters have to be taken into account in dosimetry calculation. Research shows that the biokinetics of daughter nuclei should be taken into account, as they induce a 13.5% increase for the kidney dose for unlabeled ^{225}Ac [32]. Other studies show that free ^{221}Fr and ^{213}Bi are responisble for activity accumulation in the gastrointestinal and kidneys respectively [29]. Additionally, the dosimetry of TAT remains difficult due to the different behaviour of α particles, especially when imaging modalities such as PET or single photon emission computed tomography (SPECT) cannot efficiently be used employing the emission of gamma rays. Even though ^{225}Ac emits two gamma particles (^{213}Bi: $218\ keV\ (11.44\%)$, ^{221}Fr: $440\ keV\ (25\%)$) in its decay chain, the low probability and the overlapping Brehmsstrahlung of the β-particles in the decay chain renders the theranostics approach difficult [29]. In figure 2.6, a patient is shown with a neuroendocrine tumor after ^{225}Ac-DOTATATE therapy, showing the poor resolution of the imaging modality from ^{225}Ac. Other possible approaches to asses the biodistribution and dose administered is by using another radionuclide (with the same targeting molecule) which can be imaged by PET or SPECT. However, this approach assumes that changing the radionuclide does not affect the pharmacokinetics of the radiopharmaceutical. The binding properties of the diagnostic radionuclide should be similar for a good therapeutic prediction. ^{177}Lu-PSMA has already been used to estimate the dosimetry on the basis of time–activity curves, which were extrapolated to the physical half-life of ^{225}Ac [33]. An additional solution is to create a

radiopharamaceutical which can contain more than one radionuclide. ^{225}Ac and ^{89}Zr pair have been developed in such a molecule and are still in preclinical testing [29]. Another approach to tailor the pharmacokinetics is to examine the blood, feces or urine, but gives an extra burden to the patients. Long-term follow ups are also needed to evaluate the probabilities for secondary cancers.

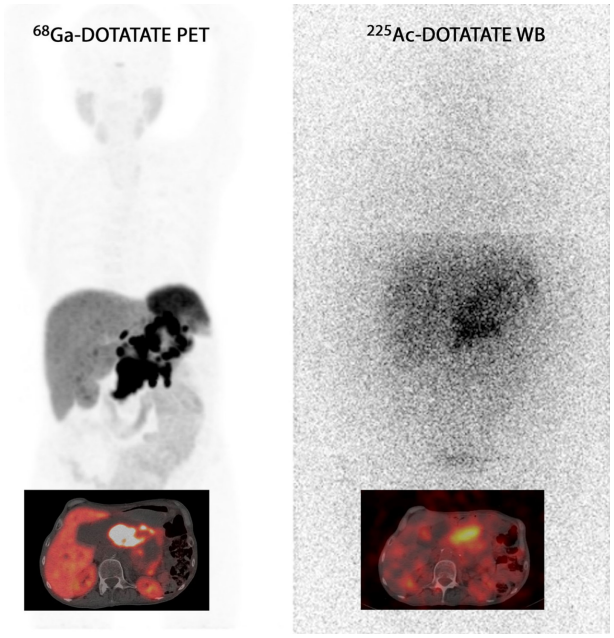

Figure 2.6: Whole-body and SPECT/CT images show increased accumulation of ^{225}Ac-DOTATATE in the mass lesion (right), concordant with ^{68}Ga-DOTATATE PET/CT (left). Image taken from [34].

To summarize, ^{225}Ac shows great potential due to its high cytotoxicity and duration of half-life. Clinical trials have proved, such as shown in figure 2.4, that ^{225}Ac is effective against cancer cells. However, challenges remain regarding dosimetry endpoints. As shown in figure 2.7, a small change in administered dose can have a severe influence on healthy tissue, which is why further research is needed to minimize unwanted administered doses. The promising results, but also the challenges to overcome, are a clear motivation to continue research.

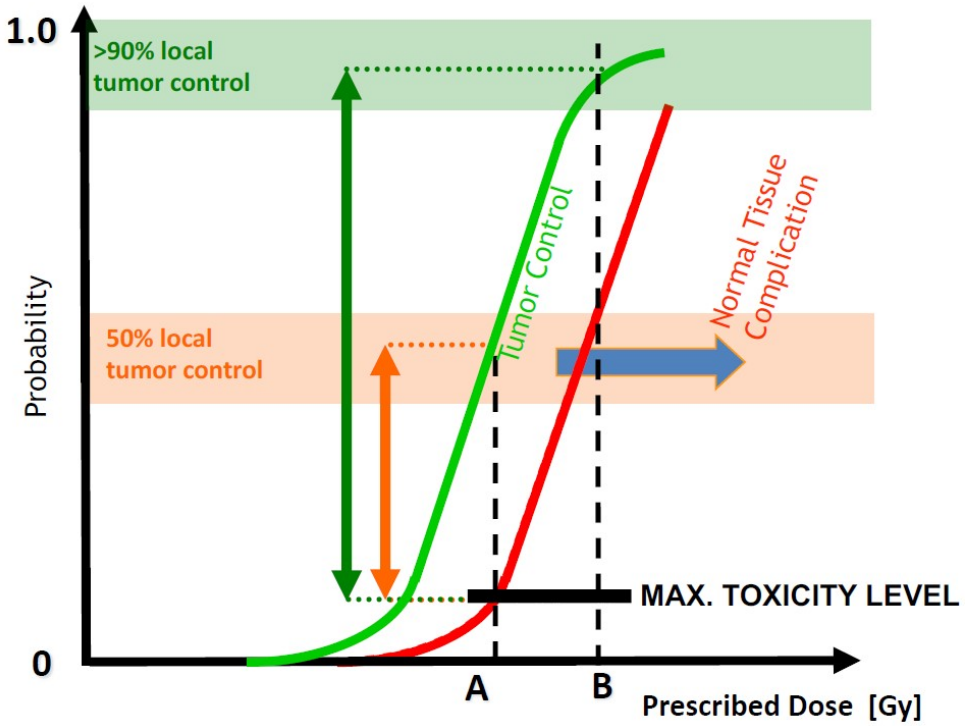

Figure 2.7: The probability for tumor control and normal tissue complication in function of the prescribed dose. It can be noted that a small change in prescribed dose majorly influences the healthy tissue. Image taken from [35].

3. Production of ^{225}Ac

Despite the promising results and challenges discussed earlier, two main factors render the ongoing research for this isotope difficult: production capability and the purity of the produced samples. In the following section, information is given on the current supply of ^{225}Ac. However, as this is insufficient to meet the global demand of the medical isotope, different production methods are discussed in section 3.2 of the medical isotope, giving an idea on how production capacity could possibly be increased. For comparison, a typical patient dose is 10 MBq and a patient typically needs 2-6 cycles of treatment [?].

3.1 Current production of ^{225}Ac

$$^{229}\text{Th} \rightarrow {}^{225}\text{Ra} + \alpha \rightarrow {}^{225}\text{Ac} + e^{-} + \bar{\nu}_e$$

The current production of ^{225}Ac is supplied by ^{229}Th generators, which themselves are generated from ^{233}U stockpiles. The majority of this uranium was produced between 1954 and 1970 for investigation in nuclear weapons and reactors [36]. Thorium-229 has a half-life of 7880 years and decays to ^{225}Ra via alpha emission, which via beta emission becomes ^{225}Ac. Three major sources are located in Germany, USA and Russia, which produce a total estimated activity of 70 GBq of ^{225}Ac per year [37]. Smaller generators exist at Canada and Belgium, but the scale of the ^{229}Th generators render it only useful for research purposes. This production pathway offers a clear advantage: the resulting product is free of other actinium isotopes yielding a purer medical product.

$$^{232}\text{Th} + \text{p} \rightarrow {}^{225}\text{Ac}/{}^{225}\text{Ra} + \text{x}$$

Besides ^{229}Th generators, ^{225}Ac can currently be produced from irradiating thorium foils at laboratories consisting of a high energy accelerator, as will be discussed below. Examples of such laboratories are TRIUMF (Canada), CERN-MEDICIS (Switzerland) and the tri-lab effort composed of Brookhaven, Oak Ridge, and Los Alamos National Laboratories in the USA. Even though there is ongoing research to make the production more efficient, the quantity produced by irradiating thorium is now lower compared to the ^{229}Th stocks.

Current global demand is estimated on to be less than 185 GBq per year, but in the future, as ^{225}Ac is approved for clinical use, the estimated demand can grow up to 200 or 400 GBq per year for each ^{225}Ac-based therapy that is approved for clinical use [38]. The overall small production of ^{225}Ac slows down the process of research, fundamental radiochemistry and clinical trials, while the resulting high price inhibits access to many researchers. Harnessing untapped ^{229}Th stocks could greatly increase the ^{225}Ac supply, however in 2005, the U.S. Congress ordered the disposal of the two tonnes of ^{233}U [38]. Without any new significant

^{229}Th sources, new production pathways should be investigated to increase production rates, which are discussed below.
The message for the need of more actinium is clear and shows itself in the society. Companies such as Pantera, Terrapower, Fusion Pharmaceuticals Inc., BWXT Medical Ltd., Actinium Pharmaceuticals, SpectronRx and NorthStar are examples of the fact that investing in the production of the promising isotope is worthwhile [39][40][41][42][43][44]. This will be done via different production methods: Pantera and Terrapower have bought the (supposed) final batch of thorium extracted from the uranium stockpiles and strive to supply actinium in the near future. Actinium Pharmaceuticals, Fusion Pharmaceuticals Inc, Northstar and also Pantera plan to use or are using irradiation of ^{226}Ra, an alternative pathway which shares the advantage of yielding a purer product. Besides these companies, projects like PRISMAP again emphasize the importance of the medical isotopes. PRISMAP is a European project which aims to create a centralized platform for accessing high-purity radionuclides, serving to diverse medical research needs. By standardizing access procedures and developing new enrichment techniques, it seeks to advance research in radiopharmaceuticals, cancer drugs, and personalized medicine, ultimately improving healthcare outcomes [45].

3.2 Promising production pathways

As current thorium generators are not sufficient to meet the demand of ^{225}Ac, other pathways are and should be considered. In this section, different promising production pathways are discussed to generate ^{225}Ac, giving the advantages, disadvantages and potential production estimates.

^{226}Ra as target material

$$^{226}\text{Ra} + \text{p} \rightarrow {}^{225}\text{Ac} + 2\text{n}$$

Three different pathways will be discussed to produce ^{225}Ac from ^{226}Ra. The first discussed reaction directly produces ^{225}Ac via ^{226}Ra(p,2n)^{225}Ac, demonstrated in 2005 by Apostolidis et al. [46]. There are 3 major advantages of this technique. The first is the high cross section, which peaks at a maximum of 710 ± 68 mb at 16.8 MeV. This high cross section enables to produce ^{225}Ac at a large scale at a single production site. A 24 hour irradiation of a ^{226}Ra target of 50 mg could produce 5 Gbq ^{225}Ac, with a current of 100 μA protons, which is equivalent to 500 patient doses of 10 MBq [7]. Furthermore, with a threshold energy of 6.8 MeV [47], the production pathway is accessible for up to more than 550 facilities housing a low energy accelerator [38][48]. Additionally, co-production of the long-lived isotope ^{227}Ac is avoided. Other isotopes of actinium are however produced: ^{226}Ac ($t_{\frac{1}{2}} = 29$ h) and ^{224}Ac ($t_{\frac{1}{2}} = 2.9$ h). Unlike ^{227}Ac, these contaminants would decay relatively fast due to their short half-lives, resulting in a higher isotopic purity over time. The co-production of these isotopes can also be minimized through selection of appropriate proton energies [7]. A drawback of this production method is the limitation of the thickness of the target material. Protons needed to induce the reaction, are quickly stopped in the target, meaning that enlarging the target does not have a beneficial influence on the production. This means only thin targets can be used, which not only limits the producing potential, but cooling abilities are limited for such thin targets [37]. The following production pathways do not suffer from the proton range and are based on the production of ^{225}Ra, which functions as a generator for ^{225}Ac.

$$^{226}\text{Ra} + \gamma \rightarrow {}^{225}\text{Ra} + \text{n}$$

The first is ^{226}Ra(γ,n)^{225}Ra, where bremsstrahlung photons impinge on a ^{226}Ra target with a threshold energy of 6.8 MeV [7]. The photons originate from the interaction of an electron beam on a metal target. This method is able to produce a ^{225}Ac yield of 550 Bq/(μA·h·mg ^{226}Ra) with 24 MeV photon beam [7]. The advantages include the absence of other actinium isotopes and accessibility to cancer centers equipped with linear accelerators (linacs). However none of these centers have the capacity to produce isotopes on a large scale [38]. This production pathway is less efficient than the proton irradiation, but has been shown to be feasible, with successful demonstrations conducted at Joint Research Centre (JRC) Karlsruhe, the Joint Institute for Nuclear Research in Dubna, Russia, and the Illawarra Cancer Centre in Wollongong, Australia [38]. Although coproduction of ^{224}Ra happens with photons exceeding 12 MeV, it shouldn't affect the intended ^{225}Ra/^{225}Ac generator. This is because ^{224}Ra ($t_{\frac{1}{2}} = 3.7$ d) decays into inert ^{220}Rn without generating any actinium isotopes.

$$^{226}\text{Ra} + \text{n} \rightarrow {}^{225}\text{Ra} + 2\text{n}$$

Another pathway is via the reaction ^{226}Ra(n,2n)^{225}Ra, where a fast neutron induces a 2-neutron evaporation. The estimated cross section for this reaction is 2 b, which is high, but the neutron beams are harder to produce. An experiment performed by J. Morell produced a neutron beam originating from deuteron break-up [49]. Their work suggested a production that could be scaled up to a quantity of 64 GBq ^{225}Ac, where a 10 g ^{226}Ra target is irradiated with a 600 μA deuteron beam at 33 MeV for 5 days [37].

Despite the potential of using ^{226}Ra for the large scale production of the medical isotope, challenges are paired with using ^{226}Ra as a target material. The material is difficult to obtain and is radioactive, complicating the target production, irradiation and recycling. It is estimated that only a few kilograms of ^{226}Ra exist on earth, however new ^{226}Ra sources could be extracted from the waste of current uranium mining operations, which could increase the supply to roughly 12.85 kilograms per year [38]. ^{226}Ra contains five alpha emissions in its decay chain, containing the noble gas ^{222}Rn. The internal alpha emissions can rupture the target, after which the noble gas and ^{226}Ra salt can escape. Strict safety protocols are mandatory to prevent the gas from escaping.

Production of ^{229}Th

Another approach is simply to produce more ^{229}Th, which naturally decays to ^{225}Ra, which on itself decays to ^{225}Ac. Producing a stockpile of ^{229}Th is a good method of providing ^{225}Ra and ^{225}Ac in the long term (due to the long half-life) [50]. Radium-226 targets provide challenges as discussed above, and high energy proton ($E_p \geq 100$ MeV) spallation of natural thorium produces a large quantities of fission products. Developing a stockpile of ^{229}Th can be achieved via various pathways.

$$^{232}\text{Th} + \text{p} \rightarrow {}^{229}\text{Th} + \text{x}$$

This production pathway describes the irradiation of natural thorium with low-energy protons ($E_p \leq 40$ MeV). A cumulative cross section of approximately 100 mb is estimated in the

work of J. R. Griswold et al. [50], which is the summation of the reaction cross sections of ^{232}Th(p, 4n)^{229}Pa, ^{232}Th(p, p3n)^{229}Th, and the ^{232}Th(p,α)^{229}Ac reaction cross sections. ^{229}Pa and ^{229}Ac decay directly to ^{229}Th via β decay. Their work estimated that irradiating a thick thorium foil target with a density of 2.34 g/cm^2 using a 40 MeV proton beam at 200 μA for one year would yield approximately 1.147 GBq of ^{229}Th. This amount of ^{229}Th is sufficient to generate about 370 MBq of ^{225}Ac every 20 days.

$$^{232}\text{Th} + \gamma \rightarrow {}^{229}\text{Th} + 3\text{n}$$

Another possibility for natural thorium would be achieved by irradiating the target with a $30 - 90$ MeV electron beam, producing photons in the target which evaporate neutrons. This method is not yet experimentally performed, but as linacs are available in many laboratories, this pathway has potential for supplying ^{225}Ac [37].

$$^{230}\text{Th} + \text{n} \rightarrow {}^{229}\text{Th} + 2\text{n}$$

^{230}Th can be extracted from the naturally occurring mineral pitchblende and provides a potential of producing ^{229}Th using fast neutron reactors. This reaction involves fast neutrons, which again is limited by the neutron beam intensity as with ^{226}Ra. An advantage of this method is the relative easy procurement of ^{230}Th. It is estimated that after a 10 year irradiation, a ^{229}Th source could be produced which contributes to 6.5 GBq ^{225}Ac per year [37].

High energy proton irradiation of ^{nat}Th, ^{nat}U

$$^{232}\text{Th}/^{238}\text{U} + \text{p} \rightarrow {}^{225}\text{Ac}/^{225}\text{Ra} + \text{x}$$

An alternative solution is the irradiation of natural thorium or uranium with high energy protons (> 70 MeV) ^{nat}U,^{nat}Th(p, X)^{225}Ac,^{225}Ra. The beam of protons induces a high number of reactions via different channels, resulting in the production of different nuclei. Thorium emerges as a more superior option than uranium for ^{225}Ac production due to its lower density, higher melting point, and a uranium cross-section that is ten times lower. Additionally, employing thorium helps avoid the co-production of ^{239}Pu and ^{235}U [38]. In contrast to ^{226}Ra, ^{232}Th is readily available as target material. It is known that stockpiles in various countries contain tens of kilograms of thorium, and theoretically 500–740 tons of thorium metal per year could be recovered worldwide by processing of monazite ($CePO^4$) [51]. The optimum reaction cross section for Th + p is found to be at ~ 150 MeV using Monte Carlo based MONC code [47]. Even though the cross section is ~ 40 times smaller than proton irradiation of ^{226}Ra, this method shows great potential. Facilities such as MEDICIS, (Switzerland), TRIUMF (Canada), the Institute for Nuclear Research of the Russian Academy, Brookhaven National Laboratory and Los Alamos National Lab (US) are using this method to produce actinium. Theoretical estimations range from $127.7 - 11267$ Gbq production of ^{225}Ac per month for each institute, depending on the maximal yield possible [38]. Target sizes are assumed to be big enough to completely stop the proton beam in these estimations (100 MeV protons have a range of ~ 16 mm [47]). These values do not account for the additional ^{225}Ac generated from ^{225}Ra generators, which could potentially increase each production total by approximately 10% to 20% [38]. Practical yields will however be lower due to the size of the target container and cooling abilities. For MEDICIS in particular, it is indicated that it can

be able to generate approximately 112 MBq of ^{225}Ac each month [38]. The disadvantage of this production pathway is the production of dozens of elements, so separation processes must follow to isolate ^{225}Ac. However, the co-production of ^{227}Ac creates concern as radiochemistry separation processes do not offer isotopic selectivity [37]. Typically a ^{225}Ac to ^{227}Ac activity ratio of $0.1 - 0.2\%$ is produced in the thorium matrix. The impact on dosimetry endpoints is estimated to be negligible, but for endpoints like facility licensing and decommissioning, waste disposal, and product licensing, the concentration of ^{227}Ac should be kept to a minimum [52].

To summarize, different pathways are possible to generate the medical isotope, but each contains challenges to overcome. ^{226}Ra targets are difficult to deal with, enlarging the ^{229}Th stock needs (more) experimental verification and high energy proton irradiation produces lots of different nuclei, including the difficult to separate and long-lived isotope ^{227}Ac. A possible solution to separate ^{225}Ac is to make use of resonance laser ionisation and mass separation. In this method, an irradiated target is heated to high temperatures (> 2000 °C), causing the created isotopes to escape the target material. The emerging isotopes are then filtered using selective ionization and mass separation, creating a more pure end product. This method will be extensively described in the next chapter, where data of such experimental runs are analyzed.

4. Analysis of MEDICIS data

In this chapter, data are analyzed from four different collections conducted in CERN-MEDICIS in 2023. The setup used for these collections is described in section 4.2, where an explanation is given about the different components. The data analysis consisted of the ion beam currents measured at various sectors of the mass separator beamline. The aim of this analysis is to extract systematic information from the data that could benefit future experimental runs and the understanding of the extraction process. The analysis consists of two parts: an estimation is made for the collected activity and the effect of the ionizing laser is investigated. The former is discussed in section 4.4. This approach allows for real-time assessment of the activity and can serve as an additional validation for the gamma spectrometry measurements performed after collection. Additionally, since ^{225}Ra and ^{225}Ac are both collected in most extraction runs, this analysis helps distinguish the origin of the ^{225}Ac on the foils, whether it is generated by the collected ^{225}Ra or directly from the ion beam. Afterwards, in section 4.5 the effect of laser ionization is analyzed. By blocking the ionizing laser regularly, a drop in the current is observed, which provides insights into the gain of collected activity and the (apparent) laser enhancement.

4.1 CERN-MEDICIS facility

MEDICIS (MEDical Isotopes Collected from ISolde) is a facility at CERN dedicated to the production of novel radioisotopes for medical imaging and treatment (see figure 4.1). It is referred to as an offline isotope separator facility, meaning that the experimental setup is not coupled to a driver beam. This means that the extraction from the target and mass separation happens at MEDICIS, but the preparation of the target happens elsewhere. This can be at an external institute, but commonly comes from the ISOLDE (Isotope Separator OnLine DEvice) facility at CERN, which lies next to the MEDICIS facility. ISOLDE receives 1.4 GeV proton beams delivered by the CERN Proton Synchrotron Booster (PSB), which makes it an online separator facility [53]. A target can be positioned in between the ISOLDE target and its beam dump, recycling the protons from the ISOLDE irradadiation [54]. During irradiation, the protons induce fission, spallation and fragmentation reactions, which results in different kinds of isotopes produced in the target. All radioactive targets are then remotely handled by a KUKA robot, whereafter the targets are placed onto the separating setup. Additionaly, MEDICIS features a laser laboratory, called MELISSA (MEDICIS Laser Ion Source Setup At CERN), which selectively ionizes isotopes by inducing step-wise resonant electron transitions/excitations in the species of interest. MEDICIS was founded in 2017 and until today, a total of 32 projects have been approved by the members of the MEDICIS collaboration board [13].

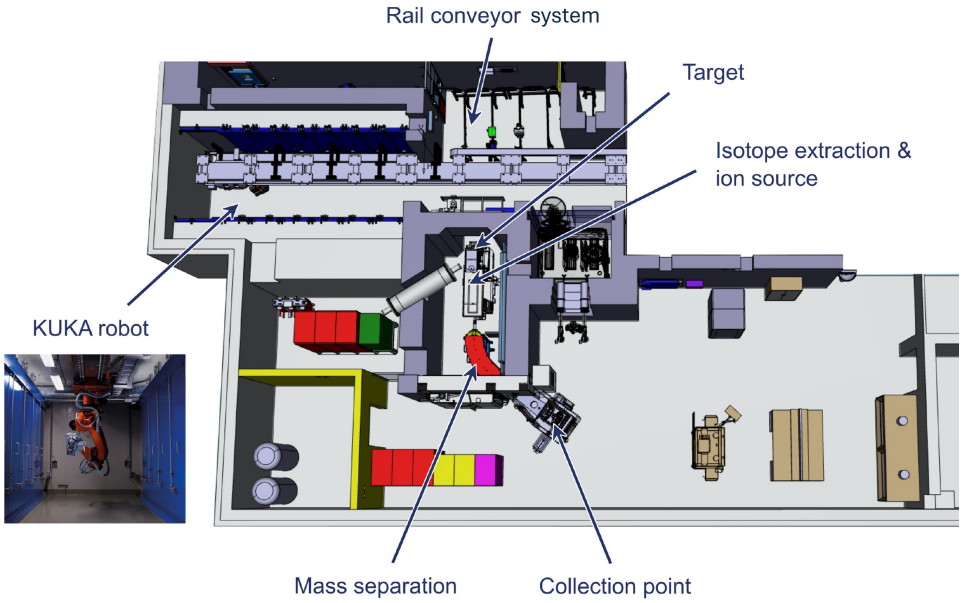

Figure 4.1: Overview of the MEDICIS facility. A KUKA robot handles the radioactive targets, which can be placed onto the extraction setup. Isotopes are extracted from the target, ionized in the ion source and then accelerated to the mass separating magnet. This filters the isotopes based on the mass-to-charge ratio before they reach the collection point. Figure taken from [55].

4.2 ^{225}Ac mass separation at CERN-MEDICIS

In this section, the offline extraction method of the medical isotopes is described. As previously mentioned, the target is prepared externally (at ISOLDE or elsewhere), whereafter the radioactive target is placed onto the front end. The extraction begins with heating the target, going up to more than 2000 °C towards the end of collection, which causes isotopes to be released from the target with rates dependent on temperature and element. This atomic vapour reaches the ion source via a heated transfer line. Here the isotopes are ionized by surface ionization or resonance laser ionization. These ions can then be extracted and accelerated from the source by an extraction electrode and focused by electro-optical components towards the dipole magnet. Here the isotopes of interest are filtered by mass separation and collected on different foils in the collection chamber. This process is schematically represented in figure 4.2.

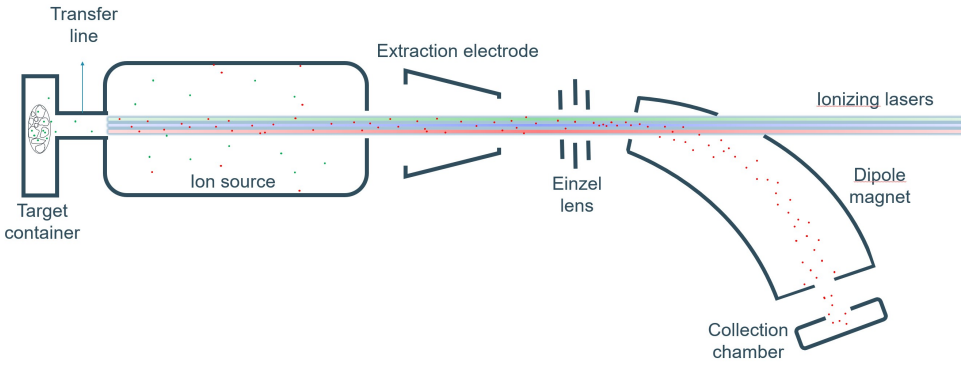

Figure 4.2: Schematic representation of experimental setup at MEDICIS. The target container is heated, which causes the isotopes to be released to the ion source via the transfer line. The isotopes are ionized by resonant laser ionization or by surface ionization. Ions are extracted and accelerated by the extraction electrode, whereafter the ion beam is focused towards a dipole magnet by an Einzel lens. Here the isotopes are filtered based on their mass-to-charge ratio before reaching the collection chamber. Different parts not shown to scale.

The total collection efficiency of this process can be written as a multiplication of the efficiencies of the different sub-processes:

$$\epsilon = \epsilon_{diff}\epsilon_{eff}\epsilon_{ion}\epsilon_{sep}\epsilon_{trans}\epsilon_{implant}, \tag{4.1}$$

containing diffusion from the target grains (ϵ_{diff}), effusion from the target grains to the ion source (ϵ_{eff}), ionization (ϵ_{ion}), separation by the dipole magnet (ϵ_{sep}), the beam transport (ϵ_{trans}) and implantation on the foil ($\epsilon_{implant}$) [6] [56]. A more detailed explanation about every step in the production method is given below. The technical description of the MEDICIS setup is mainly inspired by the work of Y. M. Palenzuela et al. [54].

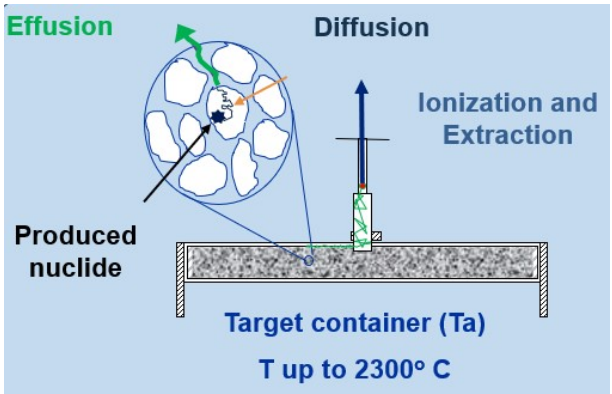

Figure 4.3: Schematic representation of the processes in target and ion source unit. The microstructure of the target material is shown, where the effusion and diffusion can visually interpreted. Figure taken from [57].

1. Target As previously mentioned, high energy protons induce nuclear reactions (spallation, fragmentation, fission) when interacting with the target material, creating a span of new isotopes. The target itself is contained in a small tantalum tubular oven of 2 cm diameter and 20 cm length, which can be heated by applying a current through it that is drawn from a

power supply rated up to 1000 A [54]. The current and temperature do not behave linearly at high currents due to radiative and resistive power dissipation. Two fitting functions are used: $P = aT + bT^4$ for power and $I = \frac{\alpha T}{T+\tau} + \frac{\beta T^4}{T+\tau}$ for current through the target (and transfer line) [6]. Bigger target containers can be beneficial for future production projects, which account for the broadened proton beam [54]. Target materials can differ between different experiments and the efficiency of production is target and isotope dependent (ϵ_{diff} and ϵ_{eff}). For the ^{225}Ac production at MEDICIS, a ThC target was used. Targets used at CERN typically present a microstructure, represented by the grains on figure 4.3. Produced isotopes have to escape the target itself and reach the ion source. This process consists of 2 steps: diffusion and effusion. The isotopes first have to diffuse out of the grains (target material), where the diffusion is described by the Arrhenius relation [58]:

$$D = D_0 exp\left(-\frac{\Delta H}{k_b T}\right), \tag{4.2}$$

where D is the diffusion coefficient, D_0 is the pre-exponential factor, ΔH the activation enthalpy of diffusion, k_b the Boltzmann constant and T the absolute temperature. After the diffusion step, the isotopes can effuse from the surface of the target material through the target matrix. The desorption rate is given by [59]:

$$r_d \sim exp\left(-\frac{E_{act}}{k_b T}\right), \tag{4.3}$$

where E_{act} is the activation energy for desorption. This process can be negatively influenced by high sticking times or for those isotopes which are chemically reactive with the target matrix. The process of effusion is typically faster than diffusion, so it is beneficial to use a porous target, even though this decreases the target density [60]. Thanks to the microstructure, isotopes reach the target surface faster via diffusion and can effuse out through the target matrix to the ion source. From equation 4.3 and 4.2, it can be seen that a high temperature speeds up the diffusion and effusion. On top of that, it reduces the sticking time to the walls of the target of container, which is also why the creation of cold spots can negatively influence the extraction efficiency [61]. However, heating a target to very high temperatures comes with a certain drawback. The maximum temperature of the target is limited by sintering, a process which brings grain growth, coarsening and porosity reduction [57]. This is an irreversible process that negatively impacts the release process. The use of carbon in the target is an efficient way to hinder the sintering process [62]. This is why a ThC target with a microstructure was used in the MEDICIS runs of 2023.

2. Ion Source The isotopes that have escaped, make their way to a rhenium ion source through a heated transfer line. The ion source is resistively heated using a current that is separate from the one powering the target, which is typically operated at 2000 °C [6]. As previously mentioned, the isotopes undergo ionization, achieved either through surface ionization or resonance laser ionization. The former happens when an isotope comes in contact with the hot surface of the ion source container, which loses an electron in the process. This technique works for elements with an ionization potential (IP) $W_i < 7\ eV$ [61]. The ionization efficiency η for surface ionization inside the ion source is given by the modified Saha-Langmuir equation [63]:

$$\eta = \frac{\beta N_{TE}}{1 - \beta(1 - N_{TE})}, \tag{4.4}$$

with

$$\beta = \alpha/(1+\alpha),$$
$$\alpha = exp\left(\frac{\phi - W^*}{kT}\right)$$

and

$$N_{TE} = exp\left(-e\Phi_P/kT\right).$$

Here ϕ is the work function - the energy needed to remove an electron from the surface - $W^* = W - kTln(\sigma_i/\sigma_0)$ the effective ionization energy, including the effect of the statistical weights $\sigma_{i,0}$, T the temperature of the heated surface and Φ_P the plasma potential w.r.t. the wall potential ($\equiv 0$). This equation incorporates the plasma that is created inside the ion source. It is therefore advantageous to use materials with high work functions to produce positive ions, such as tantalum ($\phi = 4.19$ eV), tungsten ($\phi = 4.53$ eV) and rhenium ($\phi = 5.1$ eV) [61]. The disadvantage of this ionization technique is that is not very selective. Besides surface ionization, resonance ionization is performed by two or more temporally and spatially overlapped lasers. The process consists of a stepwise excitation of the atom, where the last step excites a valence e^- to the continuum, an auto-ionizing state (state above IP) or a Rydberg state - a state close to the continuum. This method is very selective, as the ionization scheme is specific for an element. In the case of ^{225}Ac, three lasers in total were used, originating from two ionization schemes, as can be seen in figure 4.4. Via a laser window in the dipole magnet, 3 lasers were directed at the ion source with a wavelength of 438.575 nm, 456.148 nm and 424.702 nm. The efficiency of ionization is usually increased by the fact that a potential is created by the formation of a thermal plasma, which confines the ions in the center of the ion source and avoids de-ionization [64].

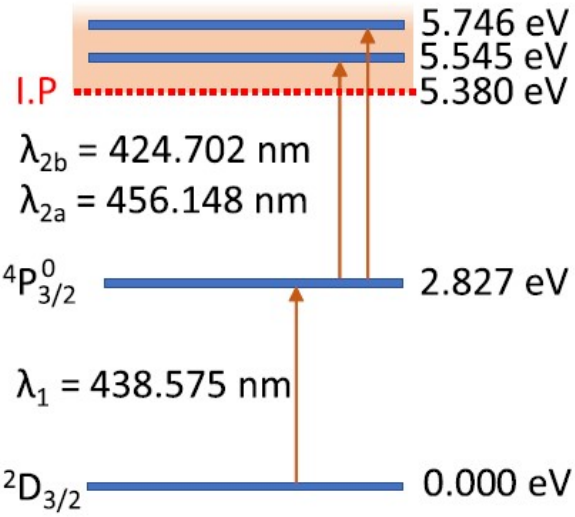

Figure 4.4: Two ionization schemes used for resonance ionization of ^{225}Ac. As step 1 is common for both schemes, 3 lasers had to be used. Figure taken from [6].

3. Beamline An extraction electrode is placed behind the ion source, which is typically put at 60 kV. Higher voltages are possible, but are not used to avoid electrical sparks. The beam is focused using an Einzel lens, which consists of three cylindrical electrodes as can be seen

on figure 4.5. The outer two electrodes are grounded, the middle electrode has a potential in the range of 18 kV (for a 30 keV beam) [54]. This mode of focusing is called decel-accel [65]. After the particles exit the first electrode, the ions decelerate axially and are pushed outward radially. When entering the second electrode, the ions are pulled inward radially and upon exiting, they are also accelerated axially. A higher voltage on the inner electrode results in a higher refractive power. It is noted that the beam is only focused and not accelerated by the lens.

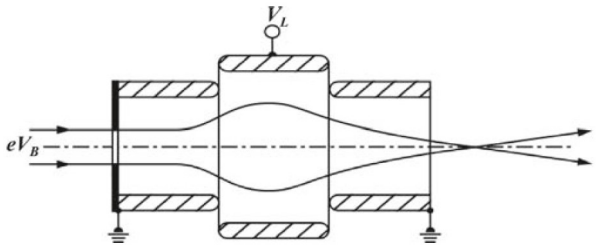

Figure 4.5: Workings of an Einzel lens in decel-accel mode. The incoming ions have an energy of eV_B and the inner electrode a potential of V_L. Image taken from [65].

4. Dipole magnet The focussed ion beam eventually reaches the mass separator magnet. The magnet from MEDICIS originates from Louvain-La-Neuve [54]. By applying a current through the coils of the magnet, the direction of the incoming ions is modified by the magnetic field. The radius r of the bended trajectory is given by

$$r = \frac{mv}{qB}, \tag{4.5}$$

where m, v and q are the mass, velocity and charge of the ions and B the strength of the magnetic field. The isotope of interest is thus filtered by its mass-to-charge ratio. It is important that the magnetic field is homogeneous in the path of the ions. The mass resolving power of the magnet is given by

$$MRP = d\frac{M}{FWHM}, \tag{4.6}$$

where d represents the separation distance between two neighboring peaks with masses M and $M+1$, while $FWHM$ (expressed in distance units) denotes the full width at half maximum of an ion beam with mass M in the focal plane of the separator. A higher MRP results in better filtering of the isotope of interest (ϵ_{sep}). The MRP depends on the magnet characteristics and the ion optical properties of the ion beam.

5. Collection chamber After the mass separation of the dipole magnet, the ion beam is implanted on a collection foil. Up to three different foils can be positioned in the setup, separated by 15 mm with a size of 250x150x0.25 mm, which enables the implantation of multiple samples during one run [54]. A collimator is positioned in front of the foils to enhance the selective collection of ions of interest. Additionally, the current on the foil and collimator is measured by a PAM, providing a measurement of the ion beam current on the collection foils at any given moment. A CZT (cadmium zinc telluride) KROMEK detector is positioned next to the foils, which is gated on the gamma rays of the daughter nuclei ^{213}Bi and ^{221}Fr

to assess the collected activity during an extraction run. Different materials can be used for the foils and depends on the radiochemistry purposes performed after collection. For the runs analyzed in this work, the materials used were thin Al coating on a gold foil and NaCl crystals on Al. Gold is chosen as a substrate, since it is inert and thus does not dissolve in acid used in the subsequent radiochemistry steps. Aluminium has the advantages that it easily dissolves. In the past, Zn was used, but the lower Z of Al provides a better mitigation against sputtering [56]. The latter is a process where the impact of the incoming ions cause isotopes on the foil to escape, which can negatively impact $\epsilon_{implant}$.

6. Beam diagnostics instrumentation Characteristics of the ion beam could be determined by Faraday cups and wire scanner. A Faraday cup (FC) is a metal cup which collects the ions of the incoming beam. Upon impact, the ions are neutralized by picking up an electron, which results in a current flow. A current from ~ 0.5 pA can be measured, which is proportional to the number of incident charges per second. Careful electronics design is therefor necessary to avoid large errors. If an ion arrives with enough energy to eject a secondary electron, failure to recapture this electron can lead to inaccurate readings. Hence, the metal cup shape is designed to maximize recapture and repeller voltages (approximately 60 V) can be applied to push back emitted e^-'s [66]. This technique interrupts the collection of isotopes on the foils. Two Faraday cups are present in the setup, before and after the mass separating dipole magnet, which are referred to as FC70 and FC30 respectively. A wire scanner works with the same principle (but no repeller voltage), but with the finite size, the profile of the ion beam can be visualized.

4.3 Description of collection runs

In this work, four collection runs from CERN-MEDICIS are examined. The runs date from May, June, August and September 2023 and will be referred to using the month. The data from each run consist of a log book and a collection report, in which details and significant events are written from during the run. This information was examined before every analysis to gain a general idea on the collection conditions. Afterwards, data from every run were retrieved from TIMBER, a CERN database. The data included ion current on collection foils, collimator and two Faraday cups, as well as heating current and voltage data, all measured in function of time. In table B.1, an overview of the available data are given.

During a collection run, the target container and transfer line are stepwise heated. At first, isotopes with a low boiling temperature escape the target, such as ^{39}K. A sudden release in isotopes can result in pressure spikes, which potentially can trip the target. In order to not damage the target or setup, the current is kept constant to give enough time for the isotopes to escape, after which a gradual stepwise increase can occur. Mass scans can be performed to identify the mass composition of the beam. This can give insight about which isotopes are being released and ionized, especially in the case of radium. A typical pattern can be recognized in the mass scan when Ra is produced, as shown in figure 4.7. This pattern of isotopes is validated through simulations using FLUKA in the work of J. D. Johnson et al. [67], underscoring its reliability. The production of actinium could be identified based on the effect of the ionizing lasers. If the lasers were blocked, a drop in the current should happen with respect to when the lasers are not if actinium is present in the ion source. During the

collections, the lasers were blocked every five or ten minutes, which gives a typical pattern as shown in figure 4.6. This phenomenon will be referred to as the laser on/off effect.
Below, more context is given about the different runs, giving details about the targets, the temperatures used and other significant information. The collection efficiency of a collection is determined by the ratio of the activity at the start and end of a collection for a particular collected isotope. The activity at the start was determined by a FLUKA estimation (Monte Carlo), the activity after the end of collection (EOC) is determined by gamma-ray spectrometry with a HPGe (High-Purity Germanium) detector. All information of the runs are based on the logbook and collection reports.

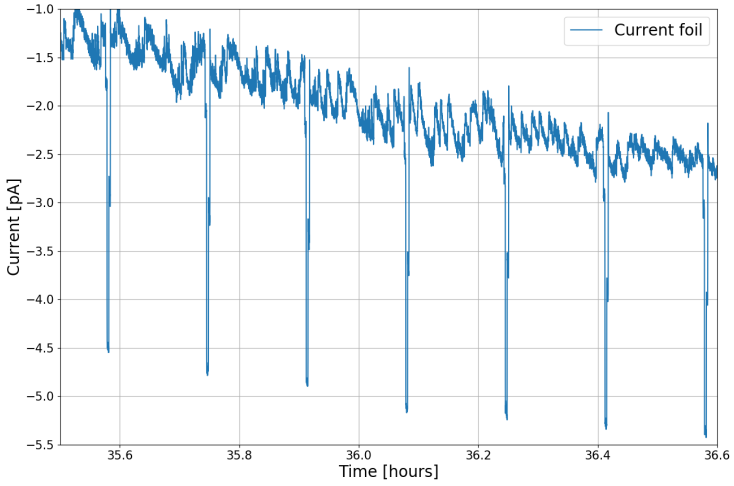

Figure 4.6: A sample of beam current data where the periodic drops are due to the lasers being blocked, approximately 30 seconds every 10 minutes (in this figure). The current [pA] on the foil is plotted against the time elapsed [hours]. The data are from the May run.

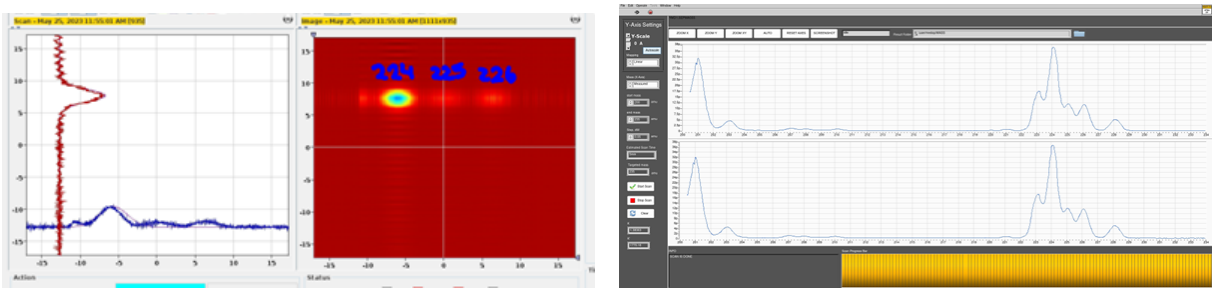

Figure 4.7: **Left.** The beam profile of radium, showing the different isotopes. **Right.** Mass scan from $A/q = 200$-235, where the typical pattern can be seen at the right. Both pictures are retrieved from the logbook of May, at a target temperature of 1400 °C and 3.90 hours in the run.

May The objective of this run was to assess the feasibility of extracting ^{225}Ra and ^{225}Ac. The target for May run was a ThC target, which was irradiated for 21.85 hours with 1.4 Gev

protons at the ISOLDE facility. 25 minutes after end of bombardment (EOB), a dose rate of 1589 mSv/h was measured for the target unit. Three foils were loaded in the collection chamber, where one was composed of NaCl/Al and the other two Al/Au. One of the latter was meant for KU Leuven for further analysis (see chapter 5). The other two foils were meant for Centre Hospitalier Universitaire Vaudois (CHUV) in Switzerland and Pakistan Atomic Energy Commission (PAEC) in Pakistan. After approximately 3.90 hours, the target was heated to 401 A (1400 °C), whereafter ^{225}Ra was seen and collected. After 30.17 hours, the laser effect of actinium was seen with a target current of 801 A (2269 °C), where the foil for KU Leuven was implanted on for a total of 1 hour, divided over 2 time intervals of 30 minutes. The maximum temperature of the target was 2398 °C. Ra collection efficiency (according to FLUKA calculations of the radionuclide inventory in the target at the time the collection starts) is around 40 % and Ac around 1%. A typical higher efficiency is seen for Ra due to the lower boiling point (1140 °C at 1 atm) and more efficient surface ionization [68].

June The same objective and target were used as in the May run. The target was irradiated for 21.98 hours, which resulted in a dose rate of 1440 mSv/h, 30 minutes after EOB. Two foils were composed of NaCl on Al, where one was meant for KU Leuven (but not for the Institute for Nuclear and Radiation Physics), the third was composed of Al/Au. After 2.5 hours, Ra was identified on the mass scan, again at a target current of 400 A, which corresponds to a temperature of 1400 °C. The laser on/off effect of actinium was seen after approximately 1.5 days, at a target current of 800 A (2260 °C). The maximum target temperature was 2398 °C. Ra collection efficiency (according to theoretical calculations in the target) is around 24 % and Ac around 0.5 %. It should be noted that sintering of the target (from May) had an effect on the efficiency of extraction from the target.

August The objective of this run was to collect ^{224}Ra and ^{225}Ra. The same target was used as in the previous runs. The target was indirectly irradiated using the ISIS station for 120.45 hours and afterwards directly irradiated using the proton beam of 1.4 GeV. For comparison, the cumulated current was 151 $\mu A \cdot h$ and 8 $\mu A \cdot h$ respectively, which resulted in a dose rate of 259 mSv/h (18.7 hours after EOB). However, the run experienced some setbacks. The target showed a lot of outgassing that hampered the heating process. The vaccuum status prevented heating of the target. The high voltage and beamline tripped during the first night. This had the consequence that not sufficient information was given about when the collection started or ended for a particular foil. For this reason, this run is not further analyzed in this work.

September The objective of this collection was to assess the feasibility of producing ^{225}Ra and ^{225}Ac, with also a small collection of ^{224}Ra for internal use. Another ThC target was used for this collection, which was irradiated for 4.58 hours by protons of the PS Booster. This resulted in a dose rate of 1270 mSv/h on the target (0.92 hours after EOB). Three salt foils were used in this run. After approximately 7 hours, the collection of ^{225}Ra began at a target current of 400 A (1421 °C). The next morning, ^{224}Ra was collected for 2 hours for radiochemistry purposes. After four days, the laser on/off effect was visible at a target current of 775 A (2268 °C), but as the beam current was low (few pA) and high temperatures were involved, it was decided to stop the collection. The laser effect was not analyzed in this run due to the short time span. The maximum target temperature was 2315 °C, corresponding to a current of 800 A. The efficiency of the collection is calculated to be 40 % for ^{225}Ra.

4.4 Activity on collection foils

One of the objectives was to estimate the collected activity on different collection foils based on the eion beam current measured during the experiment. This method would enable real-time estimation of the activity. Currently, the activity on the foils is assessed using a KROMEK detector, which detects the gamma emissions of the daughter nuclei ^{221}Fr and ^{213}Bi. While this method is effective, it has certain disadvantages. There is a delay in detecting the collection of ^{225}Ac, the detector can experience saturation and it does not entirely differentiate between the activities on different foils. The method based on the ion beam current can overcome these challenges and can also serve as an additional check on activity measured with a HPGe gamma detector.
The gamma spectrometry is performed after collection and is a mandatory step for logistics and quality control. This measurement technique can identify different isotopes on the foil through visible peaks and calculate the activity. However, it cannot distinguish between the amount of ^{225}Ac resulting from the decay of ^{225}Ra (if collected on the same foil) and the amount of ^{225}Ac directly collected from the ion beam. The technique discussed in this work addresses this limitation by estimating both amounts.

Method

The technique used in this work is based on integrating the electric current measured on the collection foils. This equals the collected charge and can be converted to an activity under the assumption that one certain isotope is collected. As mentioned above, an identification can be done for the isotopes of Ra and ^{225}Ac. This process is put in the following equation

$$A(t_1, t_2) = \lambda \cdot N(t_1, t_2) = \lambda \cdot \frac{Q(t_1, t_2)}{e}, \tag{4.7}$$

where A is the activity, λ the decay constant and N the total amount of isotopes, which is given by dividing the collected charge $Q(t_1, t_2)$ by the charge of an ion $e = 1.6 \cdot 10^{-19}$ C. The time interval $\Delta t = t_2 - t_1$ is chosen based on logbook information, matching the period when a specific foil is in use. If there are contaminants being collected, this method provides an upper limit to the total activity.

Before integrating the current, the background current must be estimated. This is the current measured on the collection foil when no isotopes from the beam reach it, which occurs when a Faraday cup is measuring and blocking the isotope beam. Even when no isotopes are collected on the foil, the measured current is not zero. This can be due to two reasons: an electrical offset where the electronics do not provide the correct value and the presence of radioactive isotopes on the foil. If these isotopes for example decay via alpha emission, a helium nucleus with a charge of $2e$ can escape the foil, resulting in a negative current. Therefore, it is essential to estimate the background current instead of simply calculating the area under the beam current. To put it another way, the measured current on the foils I_{foil} is given by

$$I_{foil}(t) = I_{beam}(t) + I_{decay}(t), \tag{4.8}$$

where $I_{beam}(t)$ is the current coming from the incoming ion beam and $I_{decay}(t)$ is the negative background current coming from the loss of charge from radioactive decay. These two values

are correlated with each other, as an increase in the ion beam current at a time t results in more radioactive isotopes collected, which decay at a time $t^* > t$. To estimate the activity collected on the foil, $I_{beam}(t)$ has to be determined for all times t. The current on the foil $I_{foil}(t)$ is measured by the PAM. However, $I_{decay}(t)$ is only given for those times t_{fc} when the Faraday cup is blocking the beam, as $I_{decay}(t_{fc}) = I_{foil}(t_{fc})$ ($I_{beam}(t_{fc}) = 0$). Since no physical model currently exists to predict the background behavior for all t, the data points $I_{foil}(t_{fc})$ are either empirically fitted or linearly interpolated to get an estimate of $I_{decay}(t)$. The interpolation has its advantage in its simplicity, making it possible to integrate this method in real-time during experiment. Empirically fitting has the advantage of assigning an error to the background estimation and gives a smoother behavior of $I_{decay}(t)$ with respect to the perfect linear connections of linear interpolation. However, as the behavior of $I_{decay}(t)$ is not known, the challenge is to choose the best fit. In this work, an exponential function

$$y(x) = A \cdot exp(k \cdot x) - b, \tag{4.9}$$

and polynomials of different degrees were chosen. The fit quality is assessed by examining the χ^2_ν value given by

$$\chi^2_\nu = \frac{1}{\nu} \sum_i \left(\frac{y_i - \hat{y}_i}{\sigma} \right)^2, \tag{4.10}$$

where y_i represents the $I_{foil}(t_{fc})$ data points, $\hat{y}_i$ the fitted values for those points, and σ the error on the current $I_{foil}(t_{fc})$. The error on the foil is determined by calculating the deviation on the current when it was relatively stable. It was found that this error was correlated with the magnitude of the current. For simplicity, the error was assumed to be 0.5 pA, which approximately corresponds to the error observed for the highest currents measured. This overestimation of the current did not result in significant errors, as evidenced by the results shown below.

After estimating the background current $I_{decay}(t)$, the area between the background and the foil current was determined using the trapezoid rule. This is done by calculating the area between consecutive data points

$$Q_i = \frac{(I_{foil}(t_{i+1}) - I_{decay}(t_{i+1})) \cdot (I_{foil}(t_i) - I_{decay}(t_i)) \cdot \Delta t}{2}. \tag{4.11}$$

The error on the calculated area was determined using error propagation, considering the statistical error on the electrical current I_{foil}, the error on the fit I_{decay} obtained by propagating the errors on the fitted parameters, and the error on the time difference Δt between consecutive points. A more detailed explanation about the errors is provided in the appendix. In the case of linear interpolation, no error is given on I_{decay} coming from the background estimation, which resulted in lower errors. This charge Q_i can then be converted to an activity A_i using equation 4.7.

By summing all A_i, the total collected activity $A(t_1, t_2)$ could be determined. However, as radioactive isotopes are being collected on the foil, the decay of these isotopes has to be taken into account using

$$A(t) = A_0 \cdot exp(-\lambda t), \tag{4.12}$$

where A_0 is the initial activity ($t = 0$) and λ the decay constant. This resulted in $A_i^{decay} = A_i \cdot exp(-\lambda \Delta t)$, where $\Delta t = t_{end} - t_i$ is the time duration till the end of collection. By summing A_i^{decay}, the total collected activity $A^{decay}(t_1, t_2)$ could be determined at the end of

collection, which could be compared with the gamma spectrometry measurement performed after collection. The timing of the latter can be found in the collection report for each run. Using this information, the activity could be calculated, using equation 4.12, to the moment when collection ended.

Results

Below, the results for the runs in May, June, and September are presented. For the May run, a detailed explanation is provided, including figures and tables that describe how the activities on the foils were determined. To maintain readability, the figures and tables for the June and September runs are included in the appendix, and only the determined activities on the foils are given here.

May run

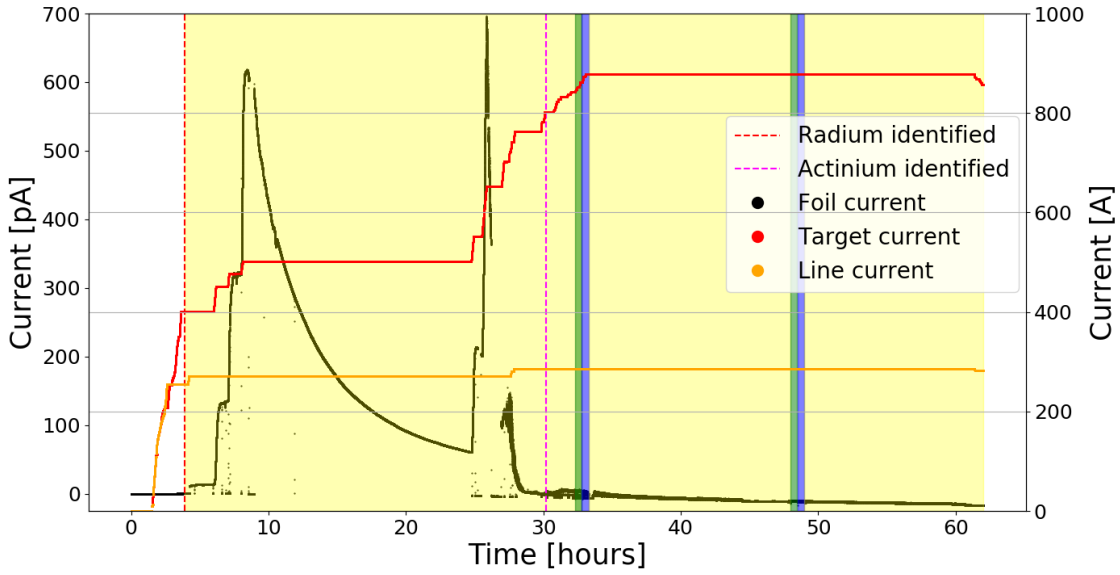

Figure 4.8: The ion beam current measured on the foils (black) and the heating current through the target unit (red) and transfer line (orange) in function of elapsed time [h]. The colored regions represent the collection on one of the three foils (yellow = MS-022, green = M-239, blue = M-233). The dotted lines indicate when isotopes of interest were identified. Sudden drops in the current happen when a Faraday cup (FC) is in.

In the May run, three foils (MS-021, M-239, and M-233) were examined. M-239 and M-233 were irradiated for one hour each to collect actinium, while MS-021 collected ^{225}Ac and ^{225}Ra for the remaining time. Collection times and the isotopes collected were retrieved from the logbook. ^{225}Ra was collected first due to its lower release onset temperature, transitioning to ^{225}Ac after 31.16 hours when the laser on/off effect was observed. An overview of the data is provided in figure 4.8.
^{225}Ra collection began after 3.90 hours with a target current of 401 A and a line current of 255 A. This process lasted for 26.27 hours, ending with a target current of 801 A and a

line current of 285 A. Background currents were fitted using multiple polynomials only (see figure 4.9), as exponential fits were not suitable given the behavior of the data. The negative values on the foil emphasize the need to take background data into account. The results are summarized in table 4.1.

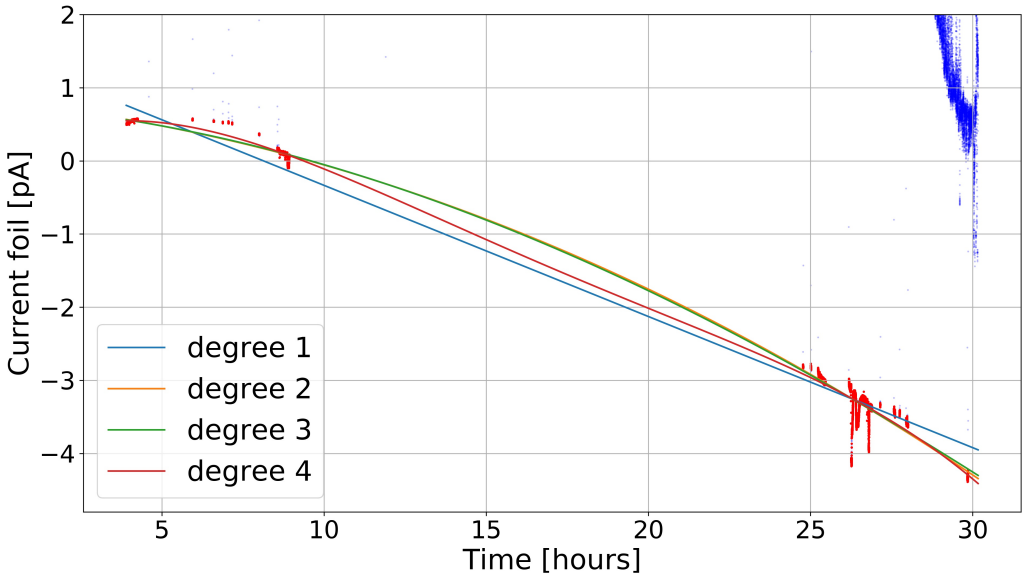

Figure 4.9: The ion beam current on the foil over time during the collection of ^{225}Ra in the May run. The red dots indicate the moments when a Faraday cup (FC) is in use. These points were fitted using multiple polynomials to model the background current. Values coming from these fits are shown in table 4.1.

Table 4.1: Summary of collected charges and activity when collecting ^{225}Ra using polynomial fits and linear interpolation for background estimation in the May run. See figure 4.9.

Background	Charge Collected [μC]	Activity [MBq]	χ^2_ν
Polynomial degree 1	$14.792 \pm 8.5627 \cdot 10^{-5}$	45.30761 ± 0.0003	0.1488
Polynomial degree 2	14.775 ± 0.002	45.2520 ± 0.0049	0.0771
Polynomial degree 3	14.775 ± 0.060	45.2533 ± 0.1878	0.0769
Polynomial degree 4	14.785 ± 9.262	45.2852 ± 29.0758	0.0760
Linear interpolation	$14.849 \pm 8.1379 \cdot 10^{-5}$	45.4883 ± 0.0003	-

Errors in the activity arise from uncertainties in electrical current and fit and seem to differ strongly between different fits. Linear interpolation errors are relatively small as they exclude fit uncertainty. These estimates provide the collected ^{225}Ra activity on foil M-021, which is compared to gamma spectrometry value (see table 4.5).
The laser on/off effect for ^{225}Ac was observed after 30.17 hours. From this moment, it was assumed no ^{225}Ra was being collected for further calculation. Background fitting was performed using an exponential and multiple polynomials (see figure 4.10). Total collected charge and activity are shown in table 4.2. Polynomials above degree 3 were excluded due to

rising activity errors. Foils M-239 and M-233 were each used twice for half an hour. Values for these foils are in tables 4.3 and 4.4. A visualisation is shown for foil M-233 in figure 4.11. The total activity was calculated using the best fit, based empirically, on the estimated error and on the χ^2_ν value.

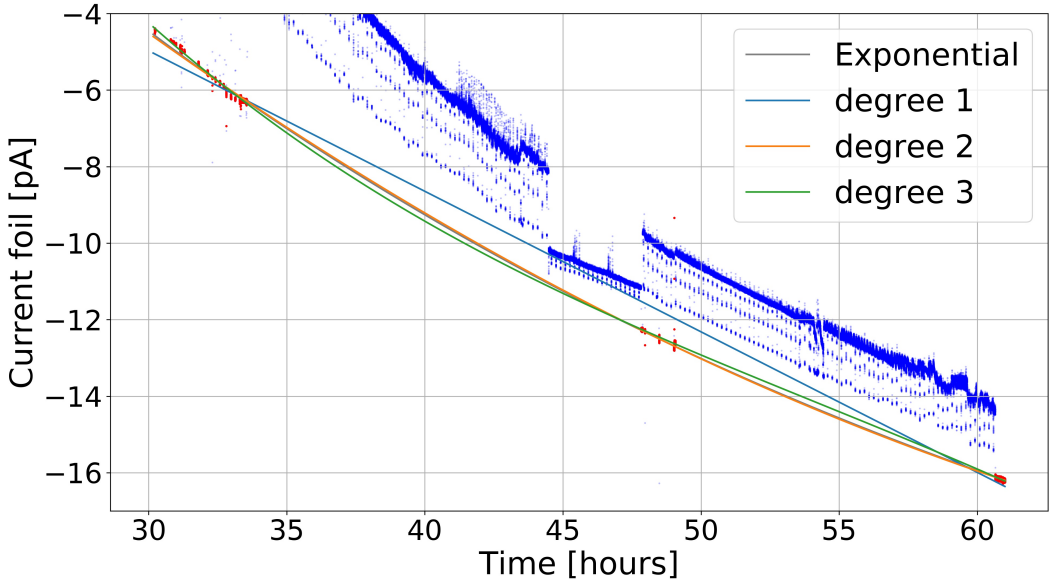

Figure 4.10: The current on the foil over time during the collection of ^{225}Ac in the May run. The red dots indicate the moments when a Faraday cup (FC) is in use. These points were fitted using multiple polynomials and an exponential. The corresponding values are presented in table 4.2.

Table 4.2: Summary of the total collected charges and activity for ^{225}Ac in the May run over a duration of 30.83 hours, using different background estimations. An illustrative representation is provided in figure 4.10.

Background	Charge Collected [μC]	Activity [MBq]	χ^2_ν
Polynomial degree 1	0.33250 ± 0.00019	1.5752 ± 0.0010	0.3844
Polynomial degree 2	0.37723 ± 0.07264	1.7916 ± 0.3587	0.0423
Polynomial degree 3	0.38 ± 38.32	1.8 ± 188.8	0.0280
Exponential	0.37798 ± 0.00008	1.7950 ± 0.0004	0.0371
Linear interpolation	0.36130 ± 0.00008	1.7149 ± 0.0004	-

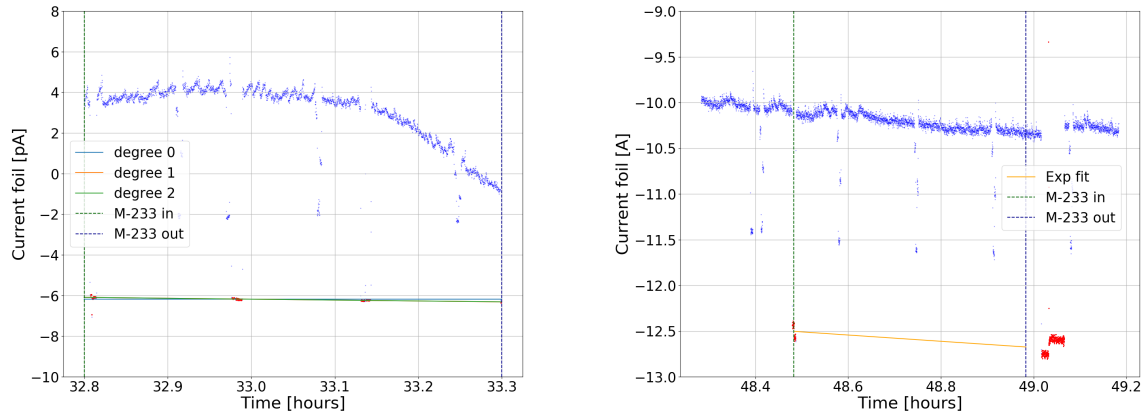

Figure 4.11: Regions 1 (left) and 2 (right) of foil M-233 in the May run, showing the ion beam current on the foil in function of time when ^{225}Ac was collected. The red dots denote the moment when a Faraday cup (FC) is in, which were fitted by multiple polynomials (left) and an exponential (right).

Table 4.3: Collected charges and activity for ^{225}Ac on foil M-233, collected at two different time intervals. Estimation is based on background data fitting or linear interpolation. An illustrative representation is given in figure 4.11.

Elapsed time [h]	Background	Charge Collected [μC]	Activity [kBq]	χ^2_ν
32.8-33.3	degree 0	0.01509 ± 0.00001	69.988 ± 0.049	0.5499
32.8-33.3	degree 1	0.01507 ± 0.00007	69.930 ± 29.069	0.5512
32.8-33.3	interp	0.01523 ± 0.00001	70.654 ± 0.049	-
48.48-48.98	exp	0.00418 ± 0.00001	20.238 ± 0.052	0.1813
48.48-48.98	interp	0.00422 ± 0.00001	20.499 ± 0.052	-
Total Activity Collected (fitting)			90.226 ± 0.071	
Total Activity Collected (interpolation)			91.153 ± 0.071	

Table 4.4: Collected charges and activity for ^{225}Ac on foil M-239, collected at two different time intervals. Estimation is based on background data fitting or linear interpolation.

Elapsed time [h]	Background	Charge Collected [μC]	Activity [kBq]	χ^2_ν
32.3-33.3	degree 0	0.01562 ± 0.00001	72.38 ± 0.05	0.0313
32.3-33.3	degree 1	0.01562 ± 0.00449	72.34 ± 20.80	0.0054
32.3-33.3	interp	0.01553 ± 0.00001	71.96 ± 0.05	-
47.97-48.47	exp	0.00432 ± 0.00001	20.93 ± 0.05	0.1342
47.97-48.47	interp	0.00419 ± 0.00001	20.32 ± 0.05	-
Total Activity Collected (fitting)			93.31 ± 0.07	
Total Activity Collected (interpolation)			92.28 ± 0.07	

To summarize the estimated activities, table 4.5 presents the total activities estimated using background data fitting and linear interpolation of the background data. These estimations can

be compared with the activities obtained from the gamma spectrometry measurements taken after collection. While the values are comparable, they do not agree within the error margins. Nonetheless, the method provides a general indication of the collected activity, except for the ^{225}Ac collected on the MS-021 foil, which differs by an order of magnitude. This discrepancy is expected and is further discussed in the following section.

Table 4.5: Summary of collected activities on the foils at the end of the May run.

Foil	Isotope	Activity from fit [MBq]	Activity from l.i. [MBq]	Gamma spec [MBq]
MS-021	^{225}Ra	48.128 ± 0.005	48.379 ± 0.0003	59.26 ± 0.12
MS-021	^{225}Ac	1.612 ± 0.0004	1.532 ± 0.0004	22.01 ± 0.61
M-233	^{225}Ac	0.090 ± 0.007	0.091 ± 0.007	0.115 ± 0.007
M-239	^{225}Ac	0.093 ± 0.007	0.092 ± 0.007	0.113 ± 0.009

June run

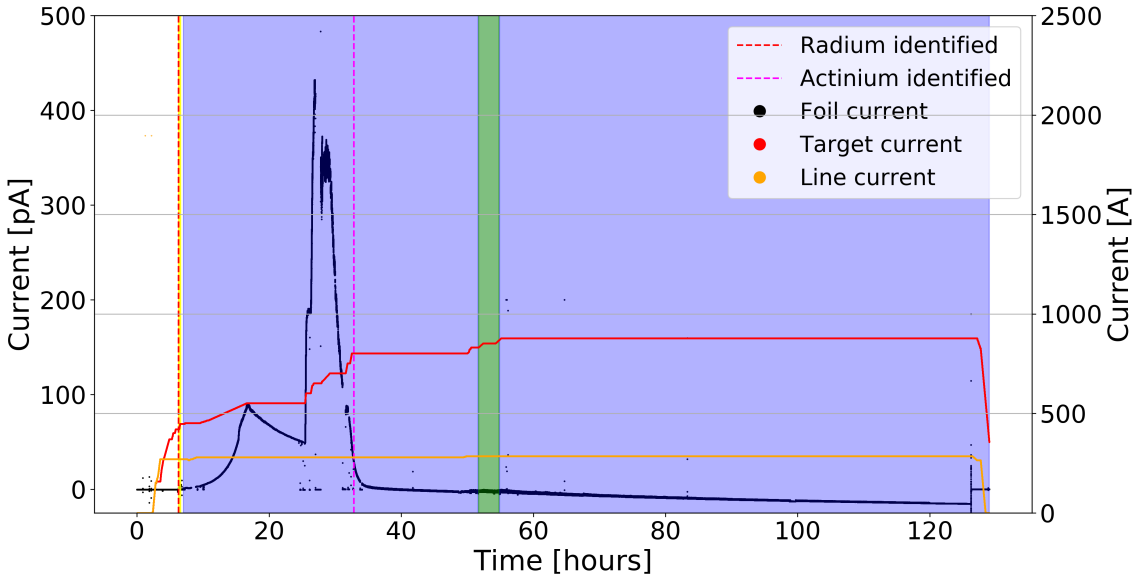

Figure 4.12: The ion beam current measured on the foils (black) and the heating current through the target unit (red) and transfer line (orange) in function of elapsed time [h]. The colored regions represent the collection on one of the three foils (yellow = MS-020 (left), blue = MS-022, green = M-288). The dotted lines indicate when isotopes of interest were identified. Sudden drops in the current happen when a Faraday cup (FC) is in.

In the run of June, ^{224}Ra, ^{225}Ra and ^{225}Ac were collected on three different foils. ^{224}Ra was only collected for 20 minutes on foil MS-020 and was used for internal research. The foil MS-022 for KU Leuven was irradiated with ^{225}Ra and ^{225}Ac right after the collection of ^{224}Ra and was in for the whole run, except when the third foil M-288 was collecting ^{225}Ac for 3.18 hours. A similar analysis has been done as for the May run, which resulted in activity estimates on the collection foils given in table 4.6.

Table 4.6: Summary of collected activities on the foils at the end of the run of June.

Foil	Isotope	Activity from fit [MBq]	Activity from l.i. [MBq]	Gamma spec [MBq]
MS-022	^{225}Ra	20.749 ± 1.966	20.707 ± 0.0002	24.96 ± 0.06
MS-022	^{225}Ac	2.381 ± 0.00064	2.533 ± 0.00064	9.698 ± 0.336
MS-020	^{224}Ra	0.0193 ± 0.0013	0.0193 ± 0.00005	-
M-288	^{225}Ac	0.133 ± 0.012	0.133 ± 0.00011	0.194 ± 0.007

September run

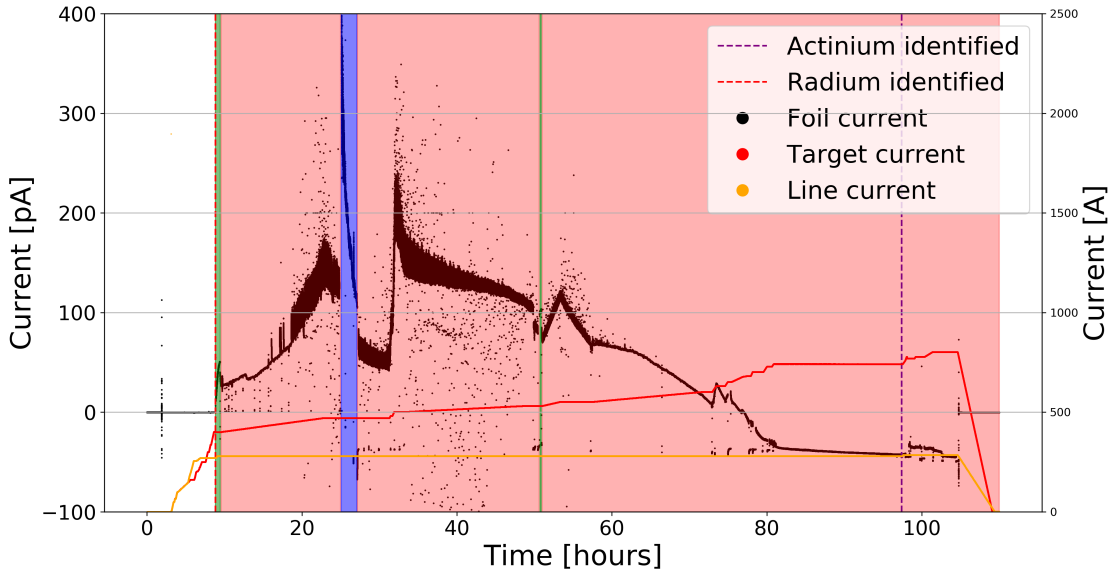

Figure 4.13: The ion beam current measured on the foils (black) and the heating current through the target unit (red) and transfer line (orange) in function of elapsed time [h]. The colored regions represent the collection on one of the three foils (blue = MS-035, red = MS-029, green = M-237). The dotted lines indicate when isotopes of interest were identified. Sudden drops in the current occur when a Faraday cup (FC) is in use. The reason for the presence of the 'spickles' is not investigated.

In the last run, the radioisotopes ^{224}Ra, ^{225}Ra and (a small amount of) ^{225}Ac were collected. A summary of the results for each foil can be found in table 4.7.

Table 4.7: Summary of collected activities on the foils of the run of September.

Foil	Isotope	Activity from fit [MBq]	Activity from l.i. [MBq]	Gamma spec [MBq]
MS-035	^{224}Ra	10.891 ± 6.645	10.980 ± 0.0002	-
MS-029	^{225}Ra	73.754 ± 1.053	75.212 ± 0.0005	122.6 ± 0.5
M237	^{225}Ra	0.546 ± 0.005	0.539 ± 0.00005	1.26 ± 0.65

Discussion

In order to estimate the activity on the foils, the background behavior of the electric current $I_{decay}(t)$ on the foil had to be estimated, which was done by either empirical fit functions (polynomials and an exponential) or by linear interpolation. These functions served to simulate the general behavior of the background current, which allowed an analysis for the collected activity. However, as can be seen for example on figure 4.9 and B.4, the behavior can be complex, which is not encompassed in these fit functions. For example, a rise in the background data can be seen at certain times after the FC is blocking the ion beam current. The span of different nuclei from the decay chain and the incoming ion beam make it difficult to predict how the background behaves. A theoretical solution seems not possible at the moment, but a simulation software could replicate this behavior better and could increase the precision of the background estimation, which ultimately influences the rest of this analysis.
Still, even though the fit functions do not fully encompass the behavior of the background, the results of the fit and interpolation can give insight in the ability to predict the general background behavior by comparing it with the measured activities by gamma spectrometry. Interpolation forms an advantage in its simplicity and can give a reasonable estimation, but a perfect linear change in background current between consecutive times where the FC is in, seems nonphysical. By looking at the values of table 4.5, 4.6 and 4.7, several things can be noticed. First of all, the error estimations on the activity are very small compared to the gamma spectrometry. It was noticed that the error estimation differed strongly between different degree polynomials and it is hard to choose the best fit, as the real behavior of the background is difficult to predict. It is thus important to realize that these error estimations do not serve as an uncertainty on the activity on the foils to take into account in further analysis or conclusions, but rather say something about the precision of this method if the background would behave in the same way (which is not fully expected). A lower degree polynomial resulted in lower uncertainties due to the simplicity of the fit, but as can be seen in the figures, this does not encompass the complex behavior of the fit. Higher degree polynomials give then higher uncertainties due the increase in fitted parameters and possible correlation, which leads to results where no further discussion can be done and can also give oscillating behaviors which are not expected for the background. A right balance had to be chosen between the two, which in this case was based empirically, on the χ^2_ν values and the error estimations. The quality of the fit, in terms of accurately simulating the background behavior, improves if there are relatively more background data points I_{decay} within the considered time interval. As shown in figure B.2, the long time interval with a low amount of background data resulted in a low-quality fit, overestimating the background data in the middle and underestimating the background data towards the end. This discrepancy is deducted from the trend of the calculated apparent laser enhancement, which is discussed in the next section. For future experiments, the background data could thus be better assessed if the Faraday cup was inserted more frequently, resulting in improved fits and providing better insights into the background behavior.
Regarding the activity estimations, the values for ^{225}Ra show relative good agreement, but consistently underestimate the measured value. The underestimation can be explained by the following. In this analysis, an abrupt transition from collecting ^{225}Ra to ^{225}Ac is assumed. This transition point is chosen based on the first observed laser on/off effect, indicating the collection of ^{225}Ac. However, in reality, ^{225}Ra continues to be collected beyond this point and gradually diminishes as all the radium from the target escapes. This leads to an underestimation of ^{225}Ra. However, the opposite is also possible, where ^{225}Ac is being collected

before the first occurrence of the laser effect. When the laser on/off effect is observed and when the lasers are optimized, an effect on the order of 5 pA is observed. Therefore, it is expected that this effect is smaller before optimization and may not be visible when higher orders of ion beam current are collected. One method to check if ^{225}Ra is still present is by examining the behavior of the laser enhancement, which will be discussed below. Another method is to assess whether the gamma spectrometry measurement identifies ^{225}Ra on a foil that was inserted after the first occurrence of the laser on/off effect. For the June run, gamma spectrometry measured 1 kBq of ^{225}Ra on foil M-228, indicating that ^{225}Ra was collected in the time span of 18.9 hours after the first occurrence of the laser effect. Although this explanation of the abrupt transition may not fully correct the underestimation, it can provide a partial adjustment. The larger part of the underestimation would either come from the fact that the background estimation for I_{decay} may be overestimated, or the current measured by the PAM is an underestimation of the collected current on the foil I_{foil}. The first hypothesis can be explained due to the correlation between I_{decay} and I_{beam}. As previously mentioned, a higher ion beam current I_{beam} results in a more negative current of I_{decay}. This should normally be incorporated in the background fit, which suggests that the general behavior of I_{decay} is not well captured by linear interpolation or fitting. Putting the FC more in would benefit this problem. The second hypothesis could in theory be tested by analyzing the ion beam current measured on FC30, which is positioned after mass separation. If FC30 measures a higher current than the current measured immediately before on the collection foil, a correction factor could be applied. This would indicate that the ion current measured on the foils is underestimated and may depend on the material and dimensions of the foil. However, this analysis could not be conducted because the current measured by FC30 was not representative of the ion beam current, displaying nonphysical behavior. If in other extraction runs, the FC would give a physical behavior of the ion beam current, then the correction factor could be determined and this hypothesis could be checked. Additionally, the material dependency on the foil could not be verified due to the influence of background current on the analysis.
For the foils where only ^{225}Ac is collected, the values also closely approximate the measured data, but also seem to underestimate the measured activity, which again can be explained by either of the previous hypotheses. For foil M-288, approximately 1 kBq of ^{225}Ra was identified by gamma spectrometry, but the magnitude of the generated ^{225}Ra should not have a big influence on the estimated value. This activity probably comes from residual ^{225}Ra in the target that has escaped after increasing the target temperature.

Looking at the values of ^{225}Ac on the foils MS-021 and MS-022, a clear deviation can be seen between measurement and the estimated value from the electric current. This is expected, as on both foils, both the parent and daughter isotope are collected. This means the values of ^{225}Ac, measured with gamma spectrometry, do not represent the directly collected ^{225}Ac, but also the decayed ^{225}Ra on the foil. The amount of actinium left on the foils coming from ^{225}Ra can be calculated using the solutions to the Bateman equation [69]

$$N_n(t) = \frac{N_1(0)}{\lambda_n} \sum_{i=1}^{n} \lambda_i \alpha_i exp(-\lambda_i t), \tag{4.13}$$

where

$$\alpha_i = \prod_{j=1, j\neq i}^{n} \frac{\lambda_j}{\lambda_j - \lambda_i}.$$

This equation encompasses the generation and decay of a certain isotope, and was applied for every activity A_i of ^{225}Ra collected coming from one trapezoid. By doing this, the ^{225}Ac on the foils coming from the ^{225}Ra can be estimated and the values are shown in the table 4.8. However, in this calculation, potential recoil of ^{225}Ac from the foil is not taken into account, though this effect is not expected to be large. If needed, this effect could be simulated [56]. The new values still underestimate the measured ^{225}Ac by $65.1 \pm 1.9\%$ and $14.3 \pm 9\%$, which makes sense since the generated ^{225}Ac comes from an underestimated amount of ^{225}Ra. Still, for foil MS-021 in the May run, the large difference in activity is not expected.

Table 4.8: Generated ^{225}Ac on foils MS-021 and MS-022 coming from ^{225}Ra. The background data are either fitted or linearly interpolated (l.i.).

Foil	Actinium generated [MBq]	Total ^{225}Ac [MBq]	Gamma spec [MBq]
MS-021 fit	6.067 ± 0.020	7.682 ± 0.019	22.01 ± 1.22
MS-021 l.i.	6.092 ± 0.004	7.623 ± 0.004	
MS-022 fit	5.931 ± 0.543	8.312 ± 0.680	9.698 ± 0.671
MS-022 l.i.	5.918 ± 0.008	8.452 ± 0.008	

Since the same target was used for both the May and June runs, it is expected that the extraction efficiency would be lower in June due to the sintering of the target. Prior to each run, the target was irradiated for 21.85 and 21.95 hours, respectively. Gamma spectrometry measurements indicate that less than half the amount of ^{225}Ra was collected in June compared to May, suggesting that sintering might have had a significant impact. However, gamma spectrometry alone cannot provide information on the extraction of ^{225}Ac due to the feeding effect of ^{225}Ra. The analysis performed in this work allows for a comparison of the extracted amounts of ^{225}Ac between the two runs. The extracted amounts were 1.7950 ± 0.0004 MBq in May and 2.5136 ± 0.0120 MBq in June, based on the background fitting. Despite the sintering effect, the total amount of ^{225}Ac collected in June was larger because the experimental run lasted twice as long. However, when the collected amounts are divided by the time difference between the first occurrence of the laser effect and the end of collection, the values are 56.412 ± 0.013 kBq/h for May and 26.142 ± 0.124 kBq/h for June. This shows that the effect of sintering slows down the extraction of ^{225}Ac, which poses to be problematic if production scales up.

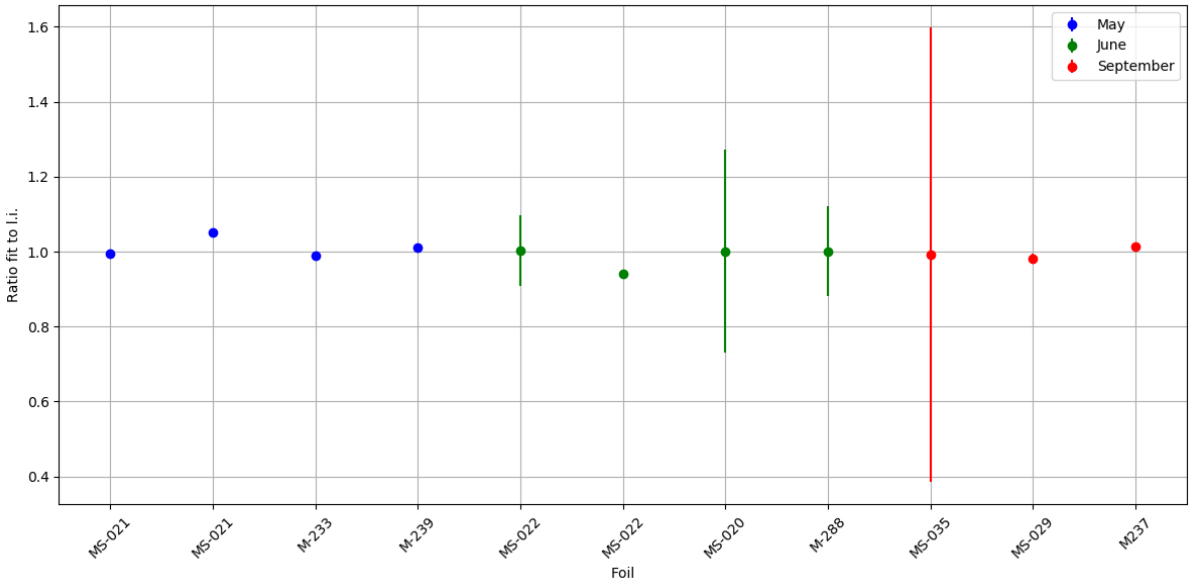

Figure 4.14: Ratio of activities calculated with subtraction of fitted background and linearly interpolated background respectively.

At last, a comparison can be made between the values coming from the fit and linear interpolation. As can be seen in figure 4.14, the linear interpolation differs from the fitted values only by 0.1-6%. The large error of MS-035 comes from the error of the fit. These values encourage the implementation of the interpolation for on-line analysis during an experimental run, due to its simplicity and the relative good agreement with the measured values.

To summarize, relative good agreement is found between the determined and measured activities, but a clear underestimation is found. A deeper analysis in the workings of the PAM in the experimental setup or analysis in the background current could benefit the determined estimations. If, in the future, this method could accurately predict the collected activity, a slight overestimation would still be expected due to the presence of contaminants in the beam (which is the topic of chapter 5), as it is assumed one isotope of interest is collected at a time in this method. High precision would be required, but this approach could enable assessment of contaminant collection. It should be mentioned that caution should be taken using the word 'contaminants', as these could include (useful) ^{225}Ra if only ^{225}Ac is expected to be collected.

4.5 Laser on/off effect

Another goal was to investigate the influence of the laser ionization on the extraction of ^{225}Ac. In the extraction run, the ionizing lasers were blocked every ten or five minutes. This was done to identify the presence of ^{225}Ac, which results in the characteristic behavior seen on figure 4.6, referred to as the laser on/off effect. The influence of the lasers was only investigated in the May and June run, since the other runs had no or no significant laser on/off effect. To assess the influence of the laser, two values were calculated: the apparent laser enhancement and the activity collected due to the ions produced by resonance laser ionization. Both values were calculated at a constant temperature of the target and transfer line. The gain in activity

thanks to the lasers allowed to calculate the true laser enhancement for three collection foils, as will be explained below.

Apparent laser enhancement

The apparent laser enhancement is given by

$$e = \frac{I_{on}}{I_{off}} = \frac{I_{Ac^L} + I_{Ac^S} + I_{C^S}}{I_{Ac^S} + I_{C^S}} = \frac{I_{Ac^L}}{I_{Ac^S} + I_{C^S}} + 1, \tag{4.14}$$

where $I_{on/off}$ represents the current when the laser is (not) blocked , I_{Ac^L} and I_{Ac^S} denote the currents from laser-ionized and surface-ionized actinium respectively and I_{C^S} represents the current from surface ionized contaminants. This is termed "apparent" since contaminants are included in the calculation. All currents were first corrected by accounting for the background current.

Method

To determine the data points for I_{off}, the mean of the lowest values within a specified time interval was calculated. These intervals were chosen around the time when the lasers were blocked, typically every 5 or 10 minutes. The minimum value within each interval was identified, and a group of data points that differed from this minimum by a specified threshold was selected. The mean and standard deviation of this group were used as the laser-off value and its error.

The I_{on} data points were chosen by shifting 25 seconds from the laser-off states to the right. Similar to the I_{off} data points, a group of data points was selected based on a specified threshold difference. This group was then used to calculate the laser-on value and its error. An example of both I_{off} and I_{on} values are visualized in figure 4.16. The background data were then subtracted from $I_{on/off}$ before using equation 4.14. It is thus important to keep in mind that the enhancement factors depend on the behavior of the fitted background.

Results

May: The laser enhancement was determined between 33.7 and 60.64 hours (EOC), where the target current was 878 A and line current 286 A. Three different regions were investigated separately, as the Einzel lens malfunctioned after 44.5 hours, lowering and increasing the current on the foil and collimator respectively. The regions can be seen in figure 4.15.
In figure 4.17, the time evolution of the apparent laser enhancement can be seen. The sudden drop of the values is due to the malfunctioning of the Einzel lens. After 54 hours, a laser optimization was performed, which disturbed the current on the foil and explains the discontinuity around 54 hours.

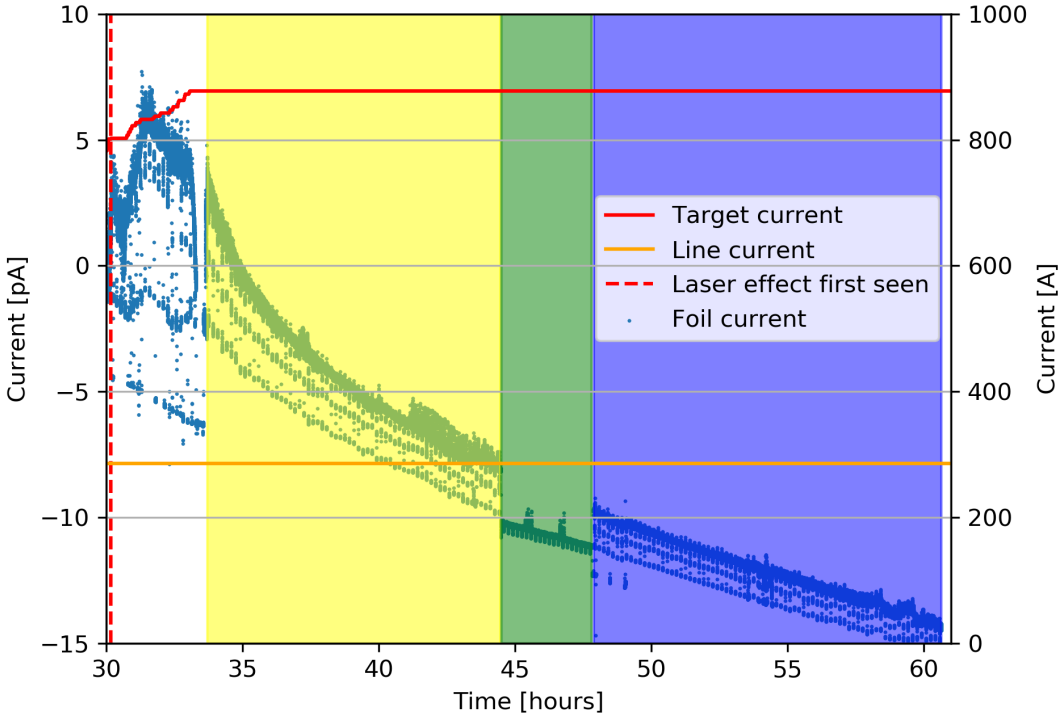

Figure 4.15: The ion beam current measured on the foil (blue) and the heating current through the target unit (red) and transfer line (orange) in function of elapsed time for the May run. Three different regions are highlighted, which are analyzed separately.

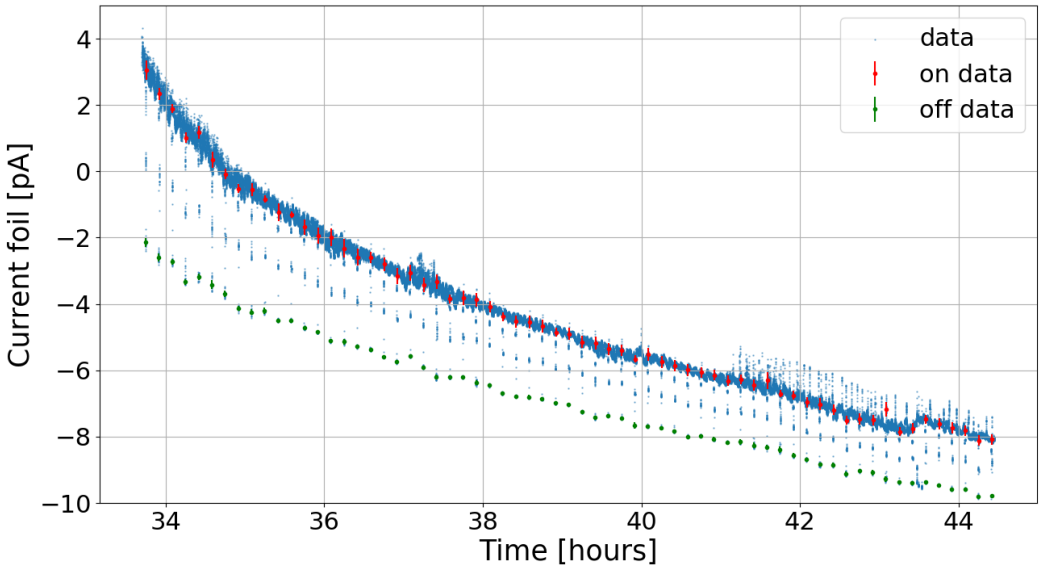

Figure 4.16: The data points of the first region used to determine the apparent laser enhancement (see equation 4.14) of the May run. Figures of the other regions are in the appendix.

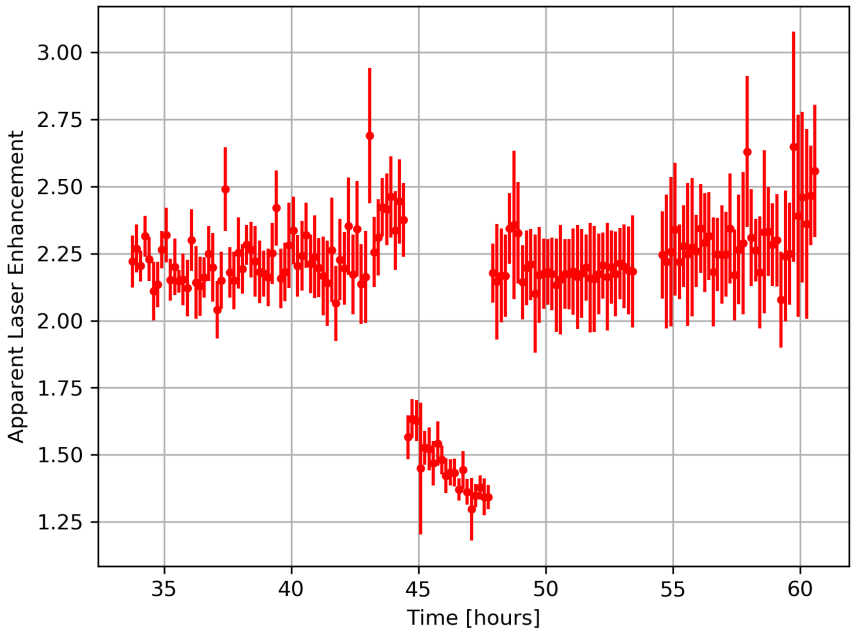

Figure 4.17: The apparent laser enhancement (see equation 4.14) of the May run. The discontinuities are due to the Einzel lens malfunctioning and a laser optimization. The target and line current are 877.69 ± 0.02 A and 285.58 ± 0.02 A.

June: Two regions were investigated for the laser effect, which are visualized in figure 4.18. In contrast to the run in May, the laser was blocked every five minutes instead of ten minutes during the collection.
The first region denoted the moment when the laser effect was first seen and has a duration of approximately 13 hours, where the target current was 802 A and line current 280 A. The apparent laser enhancement can be seen on figure 4.19. The second region considered is a time interval of 64.5 hours at the end of the collection (EOC). The target and line currents were higher than the previous region, namely 878 A and 286 A respectively.

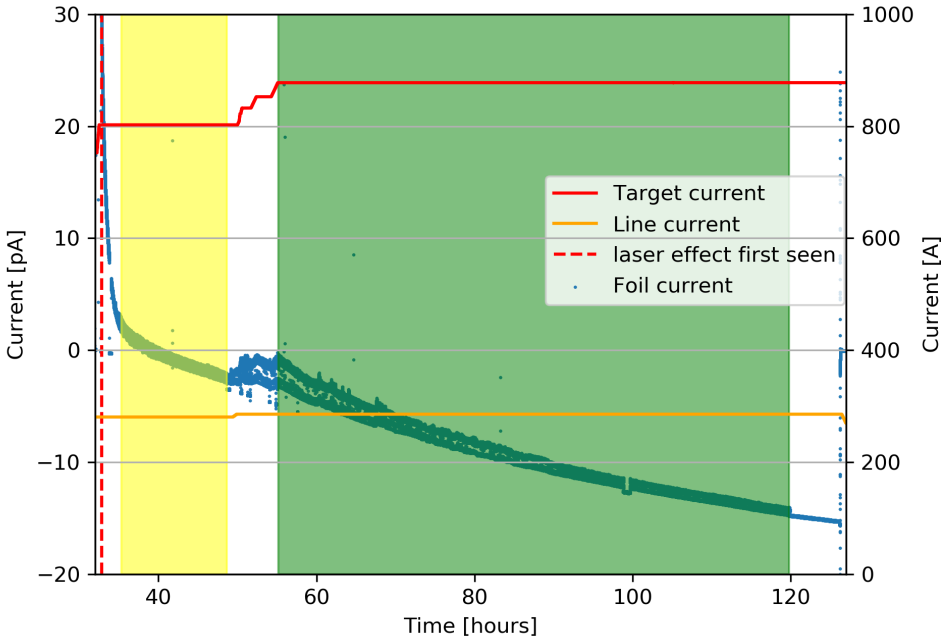

Figure 4.18: The current on the foil (blue), target (red) and transfer line (orange) plotted against time. The yellow region is the first region investigated, the second region is colored green.

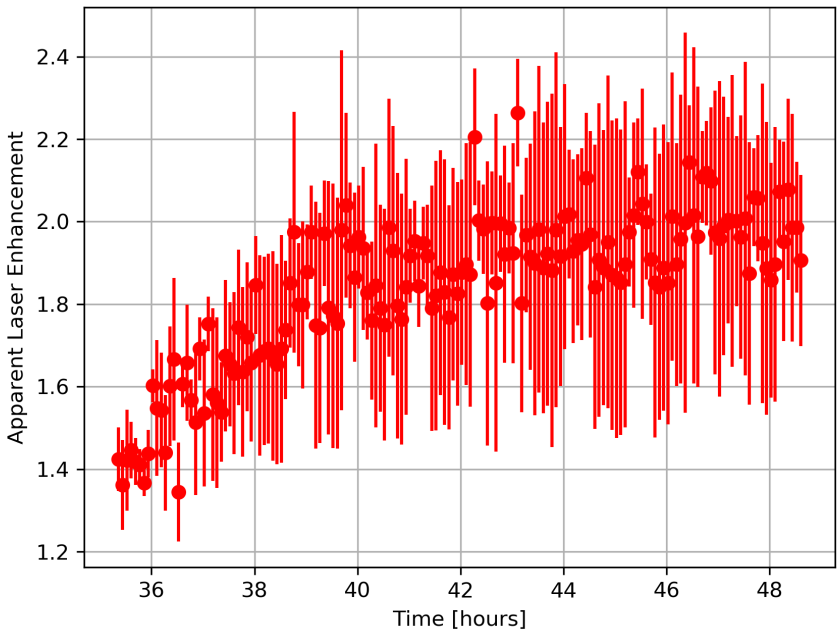

Figure 4.19: The apparent laser enhancement (see equation 4.14) of the June run in the first region (yellow on figure 4.18). The target and line current are 802 A and 280 A.

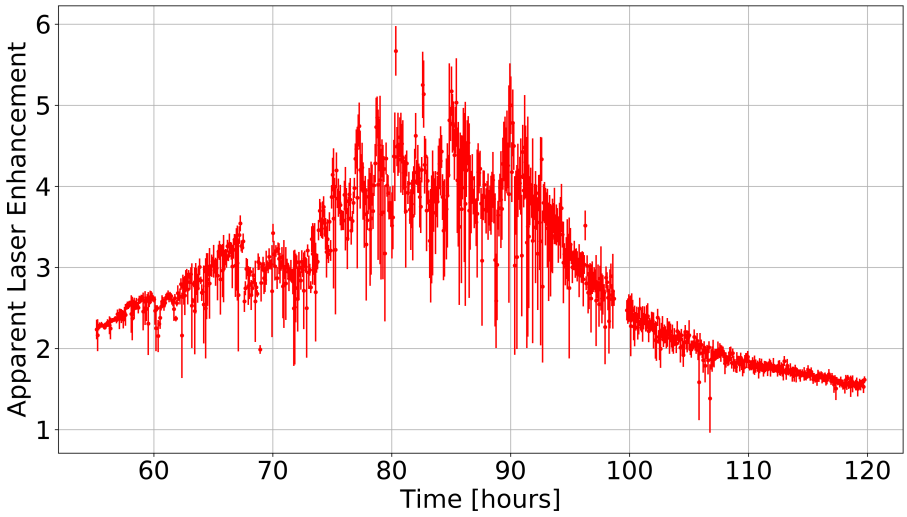

Figure 4.20: The apparent laser enhancement (see equation 4.14) at the end of the June run. The target and line current are 878 A and 286 A.

Discussion

The laser on/off effect describes the regular blocking of the lasers, which leads to a characteristic drop in the current. For the calculated values of the apparent laser enhancement, it is important to note that these values depend on the background fit, as equation 4.8 is applied. In figure 4.17, the apparent laser enhancement is shown for the May run. The sudden drop in the plot is due to an unexpected Einzel lens malfunction, and the gap around 54 hours is due to a laser optimization performed at that time. Based on this plot, it can be seen that the collected current more than doubles when the laser is turned on, highlighting the benefit of laser ionization. A better understanding of the background data could improve the precision of the enhancement factor.
For the first region of June (see figure 4.19), the values increase first and seem to saturate after four hours. If the behavior of the background would be fitted well, this plot would show that amount of contaminants (isotopes other than ^{225}Ac) is decreasing after four hours, whereafter a stability is reached where (approximately) only ^{225}Ac is collected. It is reasonable to assume this 'contaminant' is ^{225}Ra, as these values are calculated right after the first observation of the laser effect. However, by looking at figure 4.21 at the left, it can be seen that the fit overestimates the background data slightly, which can mean the saturation is an effect of the background fit. In figure 4.20, the apparent laser enhancement is given for a period of more than 2 days. However, due to the large duration and the low amount of background data, the fit on the background is considered as an incorrect representation of the real behavior. This can also be seen at the right of figure B.2, where the fit does not capture the last data points of the background data. The expected behavior was a relatively constant plot of the enhancement, as after such a long duration in the experiment, other isotopes are depleted. The increase in figure 4.20 is thus inherent to an overestimation of the background, and the decrease to the underestimation of the background at the end. From this, it can be concluded that the general behavior of the background is not properly captured by the empirical functions, certainly not for a long duration and few data points.

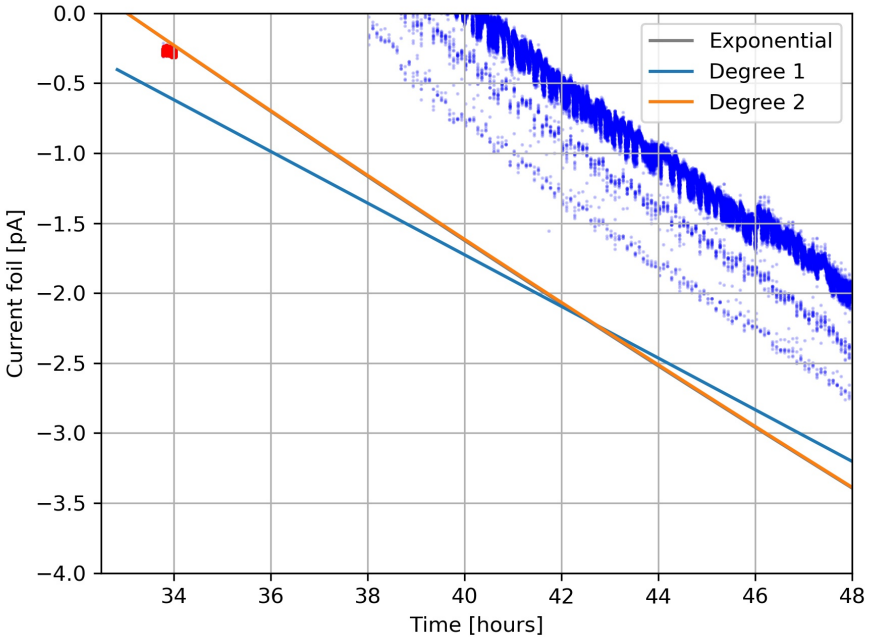

Figure 4.21: Slight overestimation of the background fit for the Ac-25 collection in the run of June. The exponential and degree 2 polynomial overlap.

The apparent laser enhancement was also calculated by fitting both the laser on and off states with an exponential. However, the results showed nonphysical behaviors and do not comply with the figures shown in this work. This means that the behavior of the current cannot be captured by an exponential.

By comparing 4.17 and 4.19, it can be seen that the laser enhancement is higher in May than in June. This can be due the difference in laser powers, which can fluctuate during a run with (poor) experimental conditions. However, the values from both figures depend on the background fit and agree within the error bars, making it difficult to draw a definitive conclusion about the cause of the observed difference.

Gain in activity

Besides the apparent laser enhancement, the gain in collected activity thanks to the lasers is estimated. This analysis allows to calculate the true laser enhancement factor, excluding the activity from contaminants, and to get an estimate of the collection rate due to the influence of the laser alone.

Method

The gain in activity thanks to the lasers is done in a similar way as explained in section 4.4, only here the 'background data' are the data points where the laser is blocked. As above, these laser off data points are either connected using linear interpolation or are fitted by

empirical functions. This allows to calculate an area using the trapezoid rule, incorporate the decay, which can be converted to an activity collected using equation 4.7. The empirical functions considered were polynomials of different degrees and an exponential function. A rate of collection is determined by dividing the amount of activity by Δt in a certain time interval. On top of this, the true laser enhancement factor could be determined using

$$e_{True} = \frac{A_{Ac}^{tot}}{A_{Ac}^{tot} - A_{Ac}^{laser}}, \tag{4.15}$$

where A_{Ac}^{tot} is the total activity coming solely from ^{225}Ac (surface + laser ionized) and A_{Ac}^{laser} the activity gain coming from the laser ionization only. The former value can be deducted from the gamma spectrometry values, the latter is determined below. However, this can only be done for those foils where only ^{225}Ac was collected, as the feeding effect is underestimated (as shown in the analysis of section 4.4). Specifically, it can be determined for foils M-239 and M-233 in the May run and M-288 for the June run (see figures 4.8 and 4.12).

Results

In figure 4.22, the fitted empirical functions are visualized for the first region of the May run. Table B.12 gives more information on the quality of empirical functions. Based on the χ^2_ν (and empirically), it was concluded to use the exponential fit in further analysis (for all regions). Using the exponential, denoted as y_{off}, for fitting the 'laser off' current, the area between the electrical current and the fit could be determined by performing the trapezoid rule, resulting in an activity (see table 4.9).

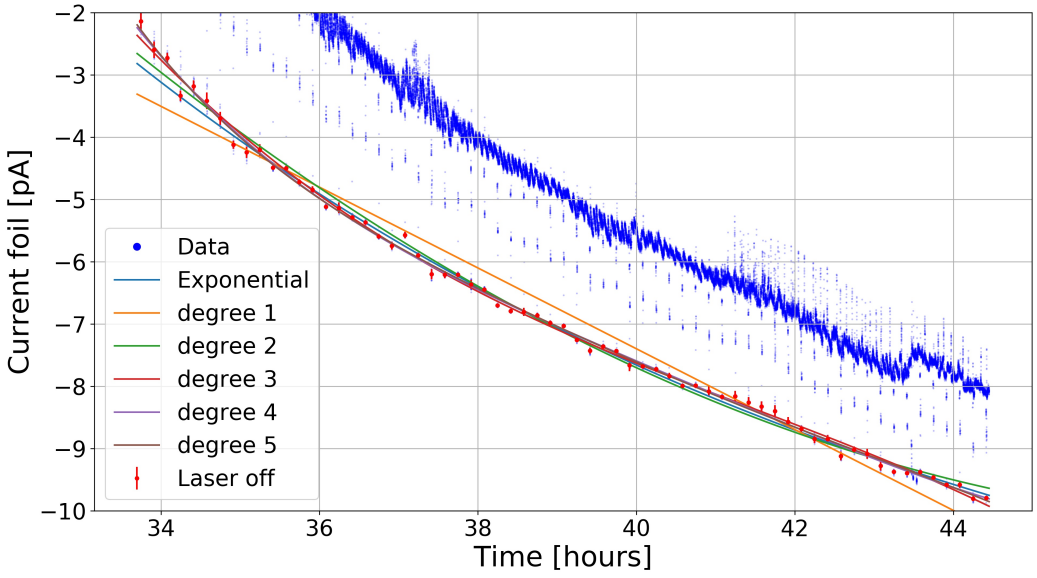

Figure 4.22: Different empirical functions used to fit the laser off data of the first region of the May run. An overview of the quality of the fit can be found in table B.12.

However, as the laser is blocked every 10 minutes for 30 seconds, some actinium is lost. This would result in a 5% decrease in collected activity thanks to the lasers, but this method

effectively checks the presence of actinium. The corresponding gain thanks to the lasers for regions 2 and 3 are also found in table 4.9. In figure 4.23, the rate of collection is shown in function of time. Noticeable is that the errors are small. For foils M-233 and M-239, a similar analysis was conducted, which allowed to calculate the true laser enhancement with the value of gamma spectrometry (see table 4.5). These values are presented in table 4.10. No rate is provided since the foils were only in use for a total of 1 hour. For the June run, a similar analysis has been done as for the May run. Similar figures as above can be found in the appendix. The results for foil M-288 can be found in table 4.10. The total collected activity in the two investigated regions are found in table 4.11 and the rate of collection is given in figure 4.24.

Table 4.9: Increase in charge and activity coming from laser ionized isotopes from different regions in the May run (see figure 4.15). The laser off data are either fitted or linearly interpolated. Collection happened at a target and line current of 878 A and 286 A.

Region	Background	Gain charge [μC]	Gain activity [kBq]
Region 1	exponential	0.09455 ± 0.00005	445.16 ± 0.23
	interpolation	0.09331 ± 0.00005	439.34 ± 0.23
Region 2	exponential	0.00356 ± 0.00003	17.17 ± 0.14
	interpolation	0.00357 ± 0.00003	17.19 ± 0.13
Region 3	exponential	0.04912 ± 0.00005	242.29 ± 0.25
	interpolation	0.04955 ± 0.00005	244.45 ± 0.26

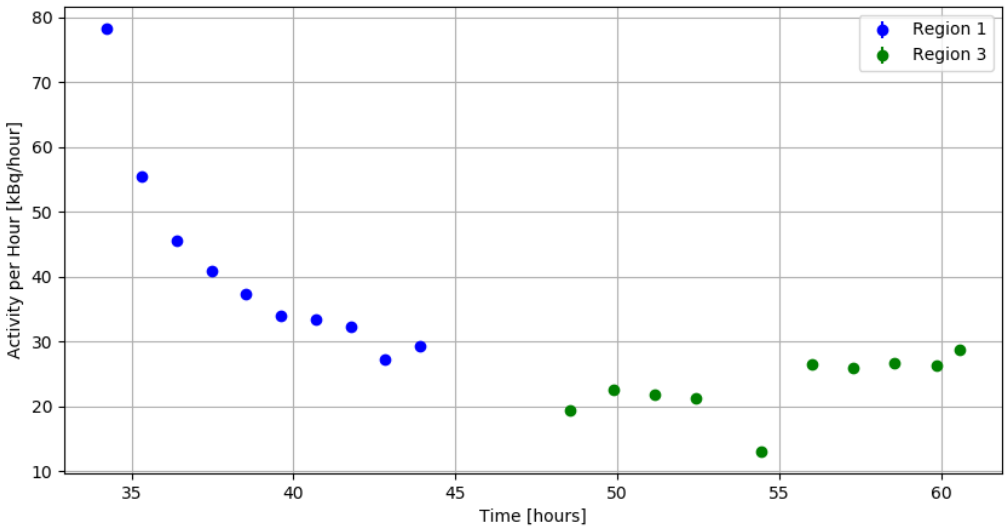

Figure 4.23: Rate of collection of the activity coming from the laser for the May run. Region 2 is not shown, as the Einzel lens malfunctioned. The laser off data were fitted by an exponential.

Table 4.10: The increase in activity of foil M-233 and M-239 (May) and M-288 (June) thanks to the lasers and the corresponding true laser enhancement e_{True}. The laser off data are either fitted or linearly interpolated (l.i.).

Foil	Gain activity fit [kBq]	e^{fit}_{True}	Gain activity l.i. [kBq]	e^{int}_{True}
M-233	47.34 ± 0.08	1.70 ± 0.07	48.12 ± 0.07	1.72 ± 0.08
M-239	54.62 ± 0.08	1.95 ± 0.14	54.47 ± 0.08	1.93 ± 0.14
M-288	71.57 ± 53.804	1.58 ± 0.70	71.46 ± 0.11	1.58 ± 0.03

Table 4.11: Increase in activity thanks to the lasers in the June run. The laser off data are either fitted or linearly interpolated (l.i.).

Region	Gain activity fit [kBq]	Gain activity l.i. [kBq]
region 1	127.82 ± 0.20	139.79 ± 0.22
region 2	881.19 ± 0.54	874.11 ± 0.54

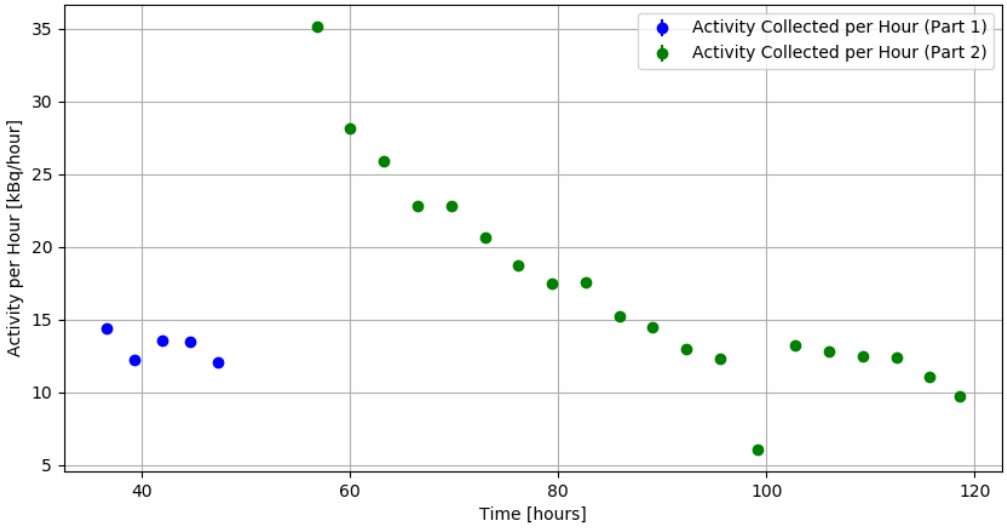

Figure 4.24: Rate of collection of the activity coming from the laser ions. The laser off data were fitted

Discussion

The collected activity due to the laser ionization is calculated in a similar way as the activity estimations on the foil. An area is calculated between a fit function and the electric current on the foil, which can be converted to an activity. Even though it was mentioned that the exponential fit of the laser off data do not fully capture the behavior of the current, this can still give a reasonable estimation of the collected activity and is compared by an interpolation of the laser off data.
Looking at figure 4.23, it can be seen that the rate of collection due to the laser effect goes down in function of time in the May run. This is expected, as most of the actinium may be

depleted from the target towards the end of collection. However, the errors on the rates are expected to be larger in reality, and the underestimation may come from the fact that the activity determination gave a small error.
For the June run, the rate of collection in the first region is lower than for all other investigated data, as can be seen in figure 4.24 by the blue data points. This could be explained by the lower target and line temperature, meaning less actinium is released from the target compared to the other regions investigated. After increasing the target temperature, the rate of collection from laser ionization increases and slowly decreases towards the end of collection. This is again expected, as most of the actinium may be depleted from the target towards the end.

By using the determined gain in activity from table 4.10 and the values from gamma spectrometry (see tables 4.5 and 4.6), the true laser enhancement could be determined using equation 4.15. As no contaminants are included in the calculation, it is expected that the true laser enhancement is greater that the apparent laser enhancement. This is, however, not the case for the May run. Figure 4.17 suggests an apparent laser enhancement greater than 2, but the true laser enhancement for foils M-239 and M-233 is lower than 2. A possible reason for this discrepancy is that the background current might be overestimated in the determination of the values in figure 4.17 or that the values of table 4.10 underestimate the activity. It should be noted that both foils were irradiated for half an hour before the region of the values in figure 4.17, while the other half hour occurred around 50 hours in the run. Additionally, a laser optimization on the first step of the laser was performed after the initial half-hour and before the data collection shown in the figure. For the true laser enhancement of foil M-288 in the June run, no good comparison could be made, as the background estimation was poor for the determination of the apparent laser enhancement. The enhancement factor was expected to be higher based on the laser ionization efficiency determined in the work of J. D. Johnson et al. [6].

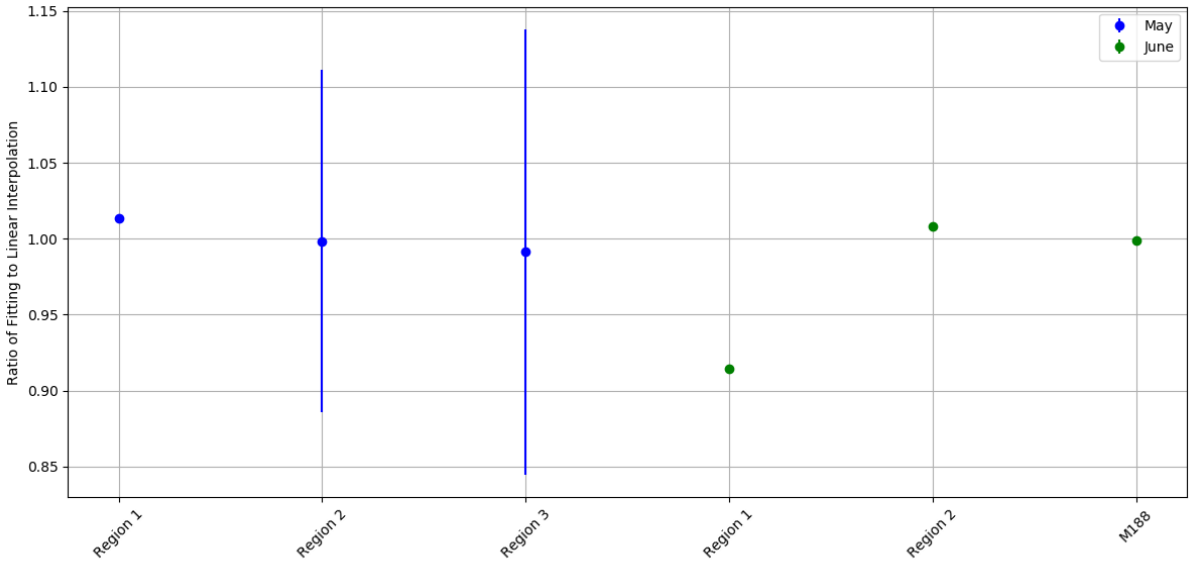

Figure 4.25: Ratio of collection of the activity coming from the laser effect from the fit and linear interpolation of the laser off data points.

At last, the values of the fit and linear interpolation can be compared. As can be seen in

figure 4.25, the values differ by a range of 0.2-8.6%, where the largest deviation comes from the long second region of the June run. Due to the long time interval of this region, the fit clearly deviated from the laser-off data points. Excluding this value, the maximum deviation is only 1.3%. The small deviation can be explained by the large amount of data points, which were regularly spaced by five or ten minutes. The simplicity and the observation that the behavior of the current is not fully captured by an exponential, show that linear interpolation is sufficient and may be even better to perform this part of the analysis.

Summary

To summarize the results of this chapter, the collected activities of every isotope in each run are shown in figure 4.26. Here it can be noted that the measured values from gamma spectrometry are underestimated by the analysis of the ion beam current measured on the foil. In table 4.12, the underestimation is given in percentages for each foil separately. Different hypotheses are given above in the discussion of section 4.4.
On top of this, it can be noted that the majority of the collected ^{225}Ac is generated by the parent nucleus. This is because more ^{225}Ra is collected, likely due to its lower boiling point and more efficient surface ionization. This ^{225}Ra can serve as a generator for ^{225}Ac. By simulating this using the Bateman equation 4.13, the total amount of ^{225}Ac generated can be calculated. A simulation was conducted under the conditions that an elution was performed after one patient dose of 10 MBq was generated or after 17.46 days, as then the maximum amount of ^{225}Ac is generated. The simulation resulted in the generation of approximately 56.5 ± 0.2 MBq, 17.9 ± 0.1 MBq, and 129.7 ± 0.9 MBq in 30 days during the May, June, and September run respectively. It should be noted that these values depend on the logistics of the elution of ^{225}Ac.
Besides the total collected activities, the influence of the ionizing lasers was investigated. For the investigated regions, a total activity is determined of approximately 0.7 MBq and 1 MBq thanks to the lasers for the May and June run. It should be noted that only regions were investigated where the heating current through the target container and transfer line were kept constant, but the total activity generated by the lasers will not differ much from the given values of the regions. The true laser enhancement ranged from 1.7-1.9 in the two runs. Variations can occur by different power levels and ion beam current extracted. The apparent laser enhancement suggested values above 2, but this analysis is dependent on the background estimation. The lower value of the true laser enhancement is either by an overestimation of the background or by an underestimated activity from the lasers.

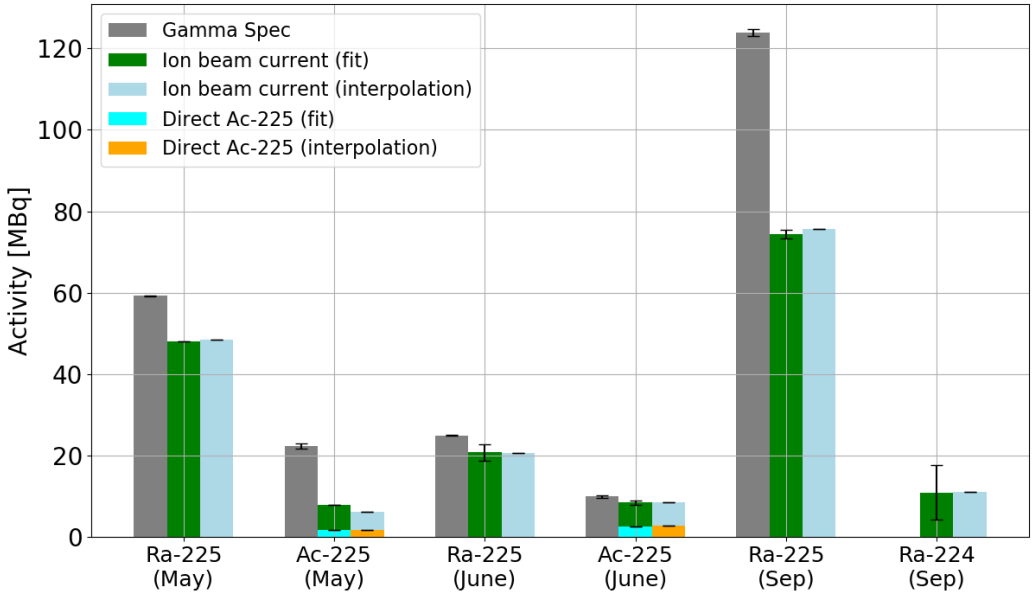

Figure 4.26: Bars representing the collected activities [MBq] in every run for each isotope collected. The values from gamma spectrometry (grey) is underestimated by both the values determined from the ion beam current on the foil, where the background is either fitted (green) of linearly interpolated (light blue). The direct collected activity of ^{225}Ac (cyan or orange) excludes the feeding effect of the ^{225}Ra.

Table 4.12: Underestimation percentages for each foil and isotope in different runs (feeding effect included).

Run	**Foil Isotope**	**Underestimation (%)**
May	MS-021 ^{225}Ra	18.79 ± 0.34
	MS-021 ^{225}Ac	65.1 ± 1.9
	M-233 ^{225}Ac	21.41 ± 9.65
	M-239 ^{225}Ac	17.06 ± 12.75
June	MS-022 ^{225}Ra	16.87 ± 7.89
	MS-022 ^{225}Ac	14.3 ± 9
	M-288 ^{225}Ac	31.66 ± 8.01
September	MS-029 ^{225}Ra	39.84 ± 0.97
	M237 ^{225}Ra	56.66 ± 44.89

5. Purity analysis

As previously mentioned in chapter 3, different kinds of isotopes are produced in the process of high energy proton irradiation of a thorium-based target, including the long-lived isotope ^{227}Ac. Separation processes are thus needed to retrieve as much ^{225}Ac, while suppressing the presence of contaminants. As radio-chemical separation processes are not isotope selective on their own, mass separation is combined with this technique to reduce the ^{227}Ac contamination. In this work, the separation enhancement factor of the mass separating process is determined for two experimental runs performed at CERN-MEDICIS by calculating the ^{227}Ac activity on the collection foil. This is difficult to do right after the collection, as the half-life of ^{227}Ac is long and the presence of the decay chain of ^{225}Ac makes it hard to measure the contaminant directly [10]. A solution to this problem can be achieved by utilizing the difference in half-lives of the actinium isotopes. Since the half-time of ^{225}Ac and ^{227}Ac are respectively 9.92 days and 21.7 years, it is possible to suppress the ^{225}Ac activity by waiting a sufficient long time. Two end products were kept in isolation since December 2022 and May 2023, which corresponds to a time of approximately 69 and 54 half-lives of ^{225}Ac till the beginning of the analysis. The contaminant ^{227}Ac should still be measurable on the collection foil, whereas ^{225}Ac should be suppressed by a factor of $9.07 \cdot 10^{-10}$ and $4.21 \cdot 10^{-9}$ respectively. This enabled to perform an α spectrometry measurement to calculate the activity of ^{227}Ac. Below, the target preparation before extraction is briefly mentioned in section 5.1. Afterwards, the components of the experimental setup are explained in section 5.2, where the process is explained on how radiation detected in the detector is translated into digital pulses transmitted to the PC, resulting in the spectrometry data. Afterwards, the calibration measurement is explained using a triple alpha source in section 5.3, allowing to relate the channel numbers of the data with the energies detected of the α-particles. Subsequently, the analysis of the MEDICIS samples is given in section 5.4, in which the initial activity is estimated of the contaminant ^{227}Ac, allowing us to calculate the enhancement factor of the mass separating process.

5.1 Target preparation

As mentioned above, two samples were investigated from two extraction runs at MEDICIS. However, it is important to keep in mind how the targets were prepared. For the December run, a thorium-carbide target was prepared by depositing 12.7 MBq and 100 kBq of ^{225}Ac and ^{227}Ac respectively into the target matrix. The target and actinium samples were provided by JRC Karlsruhe. In the May run, the target was irradiated by a high energy proton beam, as described in the previous chapter.

5.2 Experimental setup

For the spectrometry measurement of ^{227}Ac, an 'alpha setup decay spectroscopy chamber' (ASET) at KU Leuven was used, which can be seen on figure 5.1. A ladder was used to mount the source on, which can be seen on figure 5.2. The ladder enables to measure 5 sources at the same time, where the radioactive samples from CERN-MEDICIS fit the rectangular holes. The circular hole at the bottom is meant for the calibration source. However, for this experiment, only one radioactive product was investigated at a time. A silicon (Si) detector could be placed in front of the ladder and could be moved horizontally further or closer to the source. The furthest position was 23 mm from the source and could be placed in one of the 8 increments with a spacing of 2 mm. The ladder could be vertically adjusted, to align the source in front of the detector. After the alignment, the ladder could be placed inside a vacuum the chamber connected to a vacuum pump. A vacuum on the order of 10^{-5} mbar was reached during the experiment.

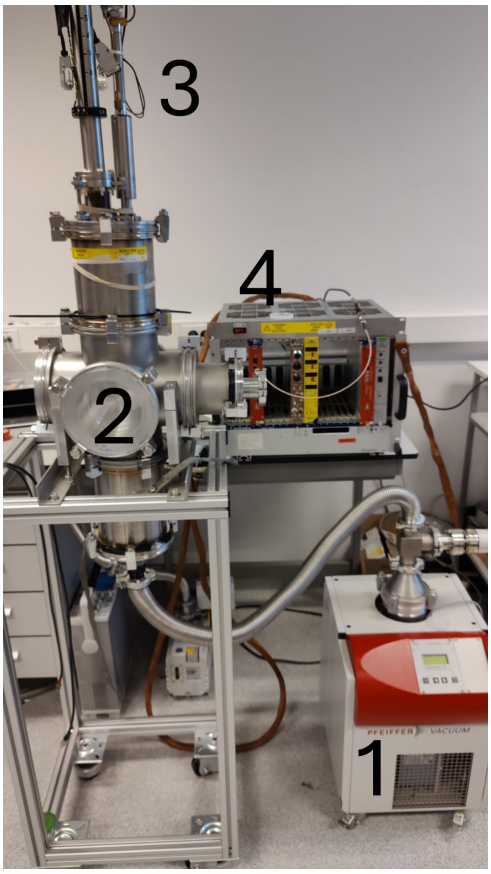

Figure 5.1: An overview of the setup at KU Leuven. 1: The vacuum pump. 2: The vacuum chamber. 3: The top of the ladder. 4: Electronics processing the received signal

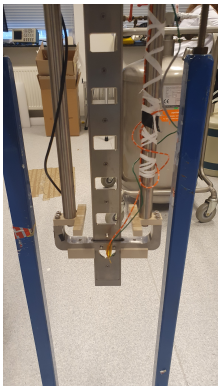

Figure 5.2: Front view of the ladder.

Figure 5.3: Side view of the ladder. The PIPS detector is mounted upon the ladder.

PIPS detector

The detector used in the measurement was a 300 mm^2 active area partially depleted passivated implanted planar silicon (PIPS) detector. This detector is based upon the detection of electron hole pairs created in semiconductor materials. A property of semiconductor material is that a crystalline structure is formed in which the atomic energy levels are split in such a way that a valence and conduction band are formed, which can be seen on figure 5.4. A semiconductor distinguishes themselves from other crystalline structures by the size of their bandgap, which is typically around 1 eV. For silicon, the bandgap is around 1.12 eV [70]. If electrons are given enough energy, they are able to cross the gap and move freely in the conduction band (allowing the flow of a current). The detector itself consist of a p-n junction or a diode, which is obtained by joining the same intrinsic semiconductor with opposite doping, or in other words a p- and n-type semiconductor. This means that impurities are inserted into the semiconductor, which results in the creation of energy levels a few meV lower or higher than the conduction of valence bands, denoted as μ in figure 5.4. For p-type conductors, trivalent atoms (B, Ga) or acceptors are added to the semiconductor material, resulting in energy levels above the valence band which can be filled with thermally excited electrons [70]. The same holds for n-type semiconductors, but here pentavalent atoms (As, P) or donors are added to create energy levels right under the conduction band. When these two types are joined together, the free electrons and holes recombine resulting in the formation of the depletion zone. This depletion zone has the same properties as an intrinsic semiconductor, but an electric field is present. If radiation passes through the depletion zone and deposits enough energy to create an electron hole pair (~ 3 eV), the two particles will drift to opposite sides of the detector [70]. The charge collection of these e-h pairs forms the electric signal used for data analysis. By putting an external voltage upon the p-n junction, it is possible to increase the size of the depletion zone by recombining more e-h pairs. This is done by applying a negative voltage (cathode) to the p-side, attracting the holes to the electrode, and a positive voltage (anode) to the n side. This is called a reverse bias and increases the chance of detecting radiation passing through the detector, while a larger current is created do to the larger electric field. For the experiments performed in this work, a bias voltage of 60 V was chosen.

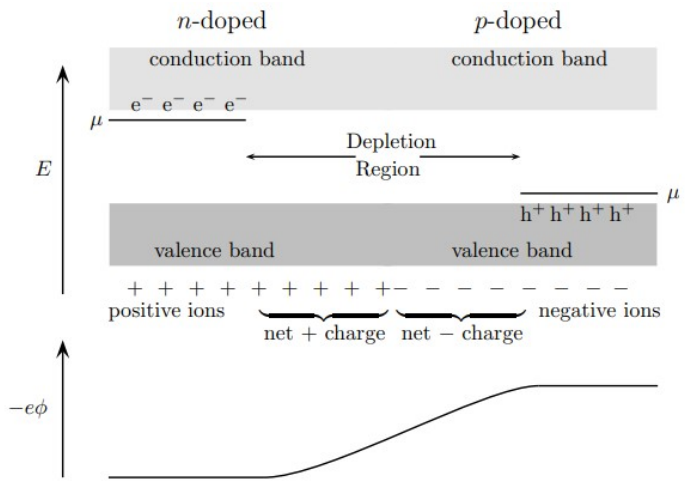

Figure 5.4: Representation of a pn junction. μ represent the added energy levels from the impurities, E the chemical potential, $-e\phi$ the electrostatic potential. The depletion region grows until the band energy is smaller than the difference in electrostatic potential. Image taken from [71].

Electronics

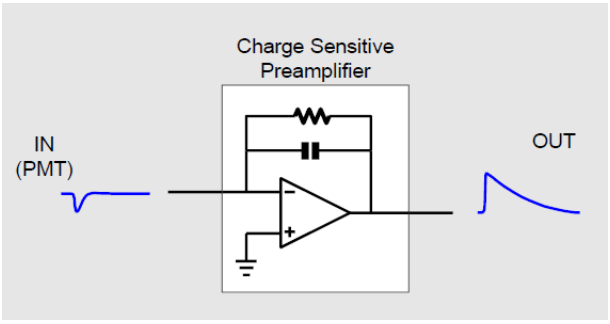

Figure 5.5: Representation of a RC-type charge sensitive preamplifier. Image taken from [72].

In this section, an in-depth explanation is given on how the electronics operate, understanding how the charge collection in the detector evolves into a digital signal given to the computer. The electric signal created in the detector has a typical duration on the order of μs or less, and the integrated signal corresponds to the charge collected. As it is desired to discriminate different energies deposited in the detector and because the output itself is very small, the signal is amplified by a charge sensitive preamplifier. This amplification is realised by an RC circuit, where the capacitor integrates the incoming signal, converting the collected charge to a voltage step, and a discharging resistor, which gives a long exponential tail. This conversion is schematically shown in figure 5.5. The charge amplitude proportionality is governed by the capacitor $V_{out} = \frac{Q}{C}$, the decay time is given by $\tau = RC$. Typically decay times from $50 - 100$ μs are chosen to give a good amplitude and to minimize the noise, but the long tail gives the disadvantage of pile-up of different detections. An important note is that the preamplifier should be wrapped into aluminium foil to shield it from noise. As the preamplifier

is very sensitive, an electromagnetic field coming from external electronics can influence the working of its operation. The aluminium also ensures that all parts of the preamplifier are held at a common ground. In the setup used at KU Leuven, a CAEN N6724s pulse height analysis digitizer was used, which can be seen on figure 5.6. Here the signal from the preamplifier directly reaches the digitizer, where the signal passes through two parallel branches: one for energy determination, the other for timing. The signal processing of the digitizer is influenced by various parameters, which are explained in the appendix. Although there are other parameters that could be adjusted within the software, for the scope of this thesis, these parameters remained untouched.

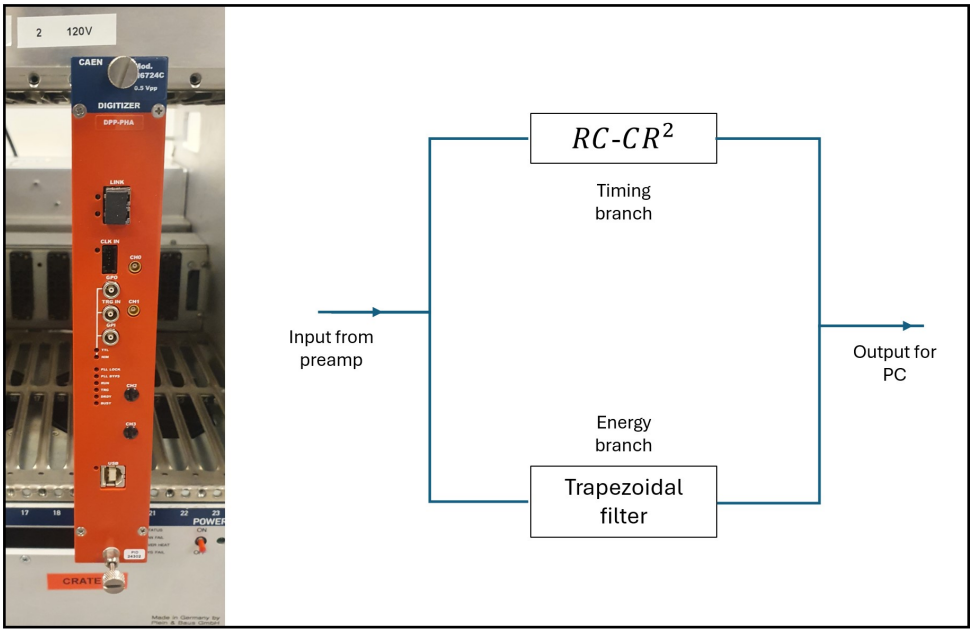

Figure 5.6: **Left:**Picture from the CAEN digitizer used in the experimental setup. **Right:** Simplified scheme of the two branches of the digitizer.

The timing is performed by a digital RC-CR^2 filter, converting the input signal to a bipolar signal, as can be seen in red above on figure 5.7. The zero crossing triggers a time stamp. The integrative component of the filter acts a low frequency filter, preventing that the fast rise of high frequency noise generate false triggers. The derivative component allows to subtract the baseline, enabling the registration of piled up events, as is shown in figure 5.7 above in blue. In the energy branch, a trapezoidal filter transforms the input from the preamplifier to a trapezoidal signal, where the height of the input signal is proportional to the amplitude of the trapezoid. It has the same function as a shaping amplifier, where the height is read out. The filter works by using two time windows, which are shifted over the input signal (blue in figure 5.7). The top of the trapezoid is then formed when one of the time windows contains the input signal while the other only contains the baseline. The width and distance between the windows can be adjusted and influences the shape of the trapezoid. After the 'peaking time' (see table A.2), samples are taken from the top of the trapezoid, which is translated into a digital value corresponding to a certain channel.

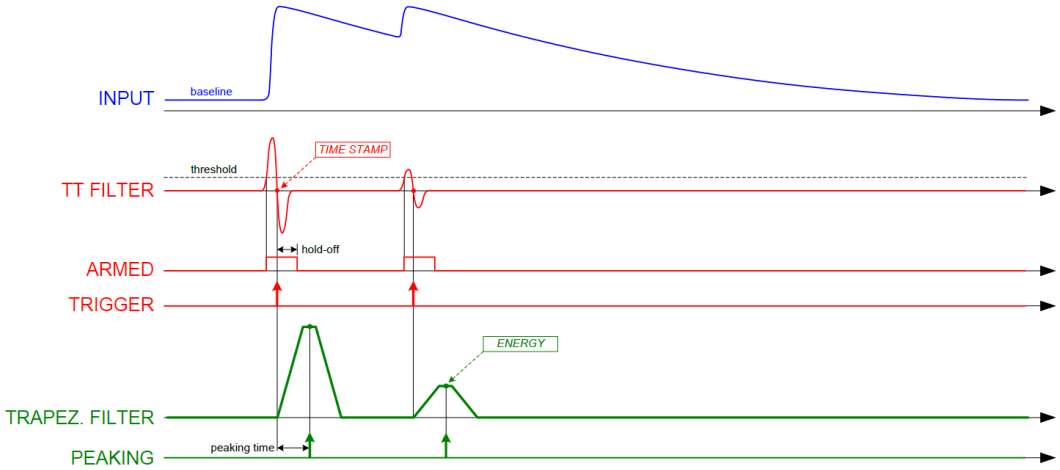

Figure 5.7: Representation of the signal shapes. The blue signal is from the preamplifier. The red bipolar signal corresponds to the timing branch and the green trapezoidal signal to the energy branch. Image taken from [72].

5.3 Calibration

Before every spectrometry measurement of ^{227}Ac, the detector was calibrated. This means a correlation is found between the channel numbers and their corresponding energy. In this case, a linear relationship $E = ax + b$ is assumed, where a and b are the calibration parameters and E the corresponding energy of channel number x. This relation is justified as the height of the signal is proportional to the energy deposited in the detector. For the calibration, the detector was put as far as possible from the source, i.e., a distance of 23 mm. This is done to minimize the angle of impact from the alpha particles, ensuring that the particles cross a similar path in the dead layer - a non-responsive layer upon the detector - and lose a similar amount of energy. A calibration can be obtained by using a known source of alpha emitters. By comparing the obtained spectra with energies of the alpha decay from literature, the correlation can be calculated. The known source used for the calibration was a triple alpha source from the IKS (figure 5.8). It contains three different unstable isotopes: ^{239}Pu, ^{241}Am and ^{244}Cm. Each of these elements have their corresponding half-life and decay energies, which can be found in table 5.1 .

Table 5.1: Initial activities, half-lives and decay energies of ^{239}Pu, ^{241}Am, and ^{244}Cm with their corresponding branching ratios (BR). Values (except A_0) retrieved from IAEA [73].

Isotope	Half-life [y]	A_0 [kBq]	Decay energies [keV]	BR
^{239}Pu	24110 (30)	2.407	5156.59(14) 5144.3(8) 5105.5(8)	70.77(14)% 17.11(14)% 11.94(7)%
^{241}Am	432.6 (6)	1.716	5485.56(12) 5442.8(13) 5388	84.8(5)% 13.1(3)% 1.66(2)%
^{244}Cm	18.11 (3)	1.699	5804.77(5) 5762.64(3)	76.9(1)% 23.1(1)%

The initial activities given on the source information card are not accurate. The real initial activities are given in table 5.1 (with 10% error). Since the source dates from 23/06/1994, the activity on the moment of the experiment is recalculated using the standard decay formula

$$A = A_0 e^{-\lambda t}, \tag{5.1}$$

where $\lambda = \frac{ln(2)}{t_{1/2}}$ is the decay constant, $t_{1/2}$ the half-life and A_0 the initial activity.

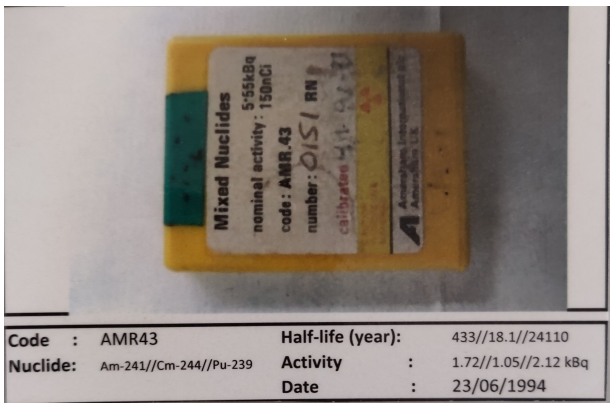

Figure 5.8: The source information card of the triple alpha source.

Two calibration runs were taken in total. The second measurement needed a separate calibration, as this experiment was performed months after the first run. Further information about the two experiments can be found in table A.3 in the appendix. The data was stored as csv files up to 10 MB, which resulted in 33 and 32 files for the first and second run. By setting a maximum file memory, not all data files would be lost if something were to happen during the measurement. These files were separately analyzed in python and fitted using a least square minimisation. Every decay peak was fitted using a Crystal Ball function [74]:

$$f(x;\alpha,n,\mu,\sigma) = N \cdot \begin{cases} exp\left(-\frac{(x-\mu)^2}{2\sigma^2}\right), & \text{if } \frac{x-\mu}{\sigma} > -\alpha \\ A \cdot \left(B - \frac{x-\mu}{\sigma}\right)^{-n}, & \text{if } x \leq -\alpha, \end{cases} \tag{5.2}$$

where

$$A = \left(\frac{n}{|\alpha|}\right)^n exp\left(-\frac{|\alpha|}{n}\right),$$

$$B = \frac{n}{|\alpha|} - |\alpha|.$$

In equation 5.2, N is the amplitude, μ the center of the peak and σ the standard deviation, just as in a Gaussian. The difference with a Crystal Ball function are the parameters which define the low energy tail. The parameters α and n describe respectively when the tail starts and how strong the tail is. When alpha particles enter the detector, they may experience energy loss, particularly when traversing the dead layer. By using the Crystal Ball function, this phenomenon is taken into account, resulting in a better fit. A distinct Crystal Ball function was defined for each alpha decay branching. These functions were summed for each element, as certain peaks overlapped. This meant for example that for ^{239}Pu, three different functions like equation 5.2 were summed and the total function $f_{tot} = f_1 + f_2 + f_3$ was fitted to the range of the Pu peaks. On figure 5.9, the fit can be observed of an arbitrarily chosen file.

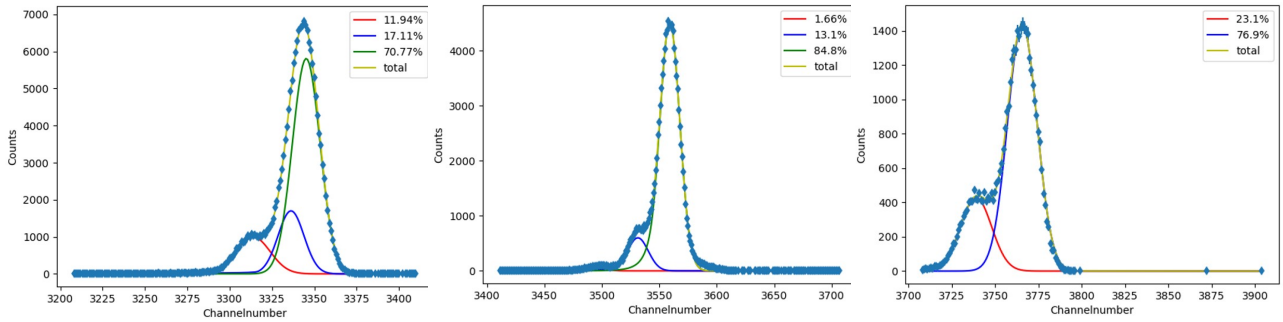

(a) Fit of the Pu peaks. (b) Fit of the Am peaks. (c) Fit of the Cm peaks.

Figure 5.9: The fitted peaks of the triple alpha source by using a Crystal Ball function, where the amount of counts are plotted against the channel numbers. The labels correspond with the branching ratio.

For Pu, it can be seen there are two functions fitted in one peak. As depicted in table 5.1, the decay energies of the highest branching ratios lie very close to each other. This had the consequence that the fit was dependent on the initial values and constraints were given for the parameters to gain realistic results. After the data was fitted, the mean value μ in equation 5.2 of every peak was retrieved. This resulted in 7 centroid positions corresponding with every alpha decay energy. By comparing the energy values of the peaks from literature (table 5.1) and the obtained centroid positions, a linear fit was performed, as shown in figure 5.10, with the calibration parameters in table 5.2 . With this result, the x-axis of the spectrometry measurement could be changed from channel numbers to energy [keV].

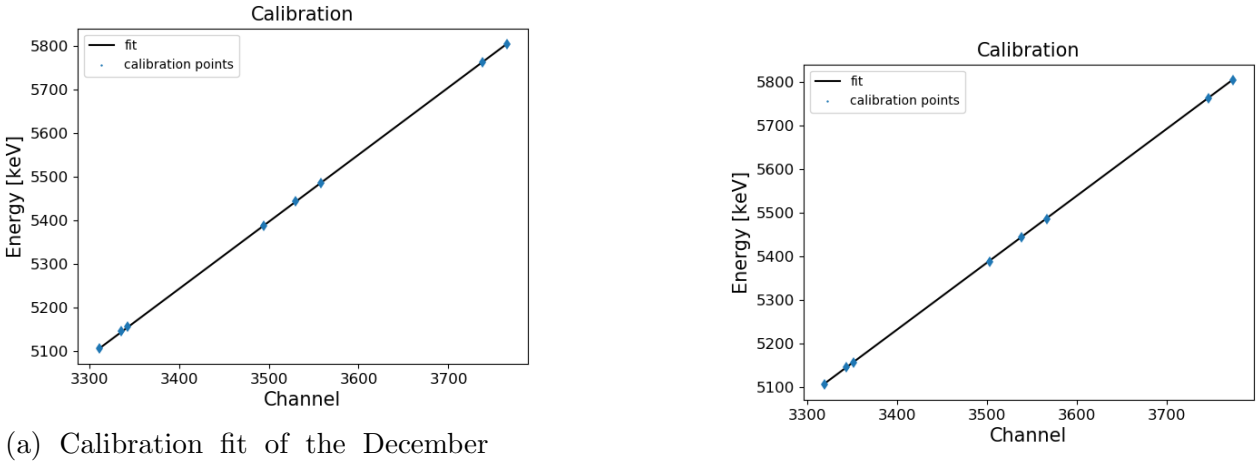

(a) Calibration fit of the December run.

(b) Calibration fit of the May run.

Figure 5.10: The equation $E = ax + b$ was fitted, where x represents the mean of one branching peak of all files (errors are present). Parameters a and b can be found in table 5.2.

Table 5.2: The calibration parameters obtained from the triple alpha source.

	a [keV/channel]	b [keV]
December 2022	1.5418 ± 0.0028	0 ± 0.66
May 2023	1.5352 ± 0.0028	12.096 ± 9.477

5.4 Determination of the activity

After the calibration, the ^{227}Ac source could be placed into the experimental setup. As the activity of the radioactive samples were expected to be low, the detector was placed closer to the detector at a distance of 9 mm to increase geometric efficiency. The sample from December 2022 was measured for 4 days, the second sample was measured for 6 days, as the activity of the latter was expected to be lower. The analysis of the data was done in ROOT, where the maximum memory of the files were respectively 1 MB and 50 kB. By employing the calibration parameters of table 5.2, the x-axis was set in energy. In this way, the peaks in the data could be identified with known isotopes, which can be seen in figure 5.11 and 5.12. As expected, elements from the decay chain of ^{227}Ac were present, but also elements were identified of the decay chain of ^{226}Ra and ^{208}Po (see decay chains on figures 5.13 and 5.14).

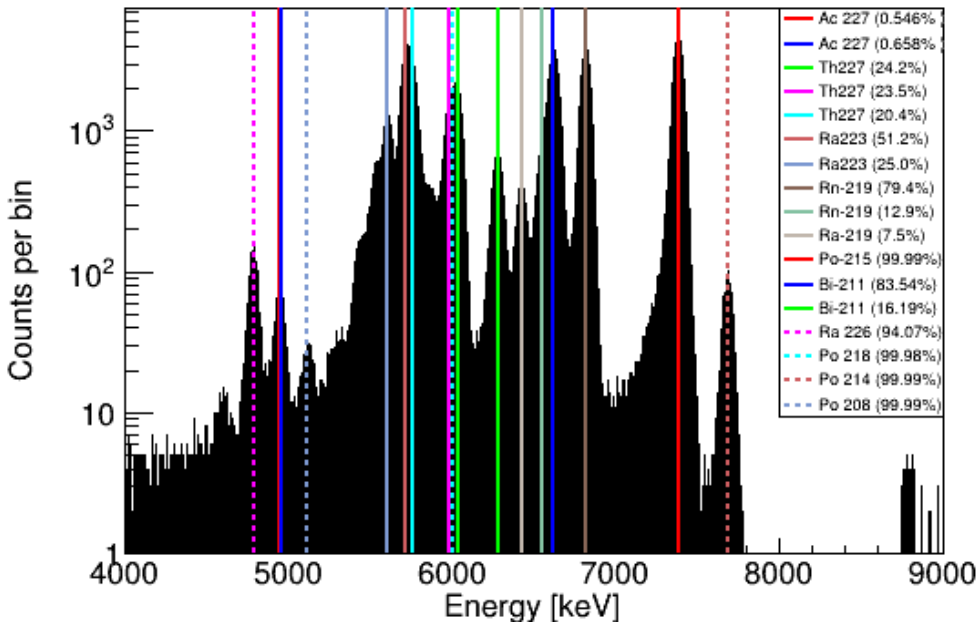

Figure 5.11: Spectrometry data from the December source, where the peaks are identified. Full lines represent isotopes from the decay chain of ^{227}Ac.

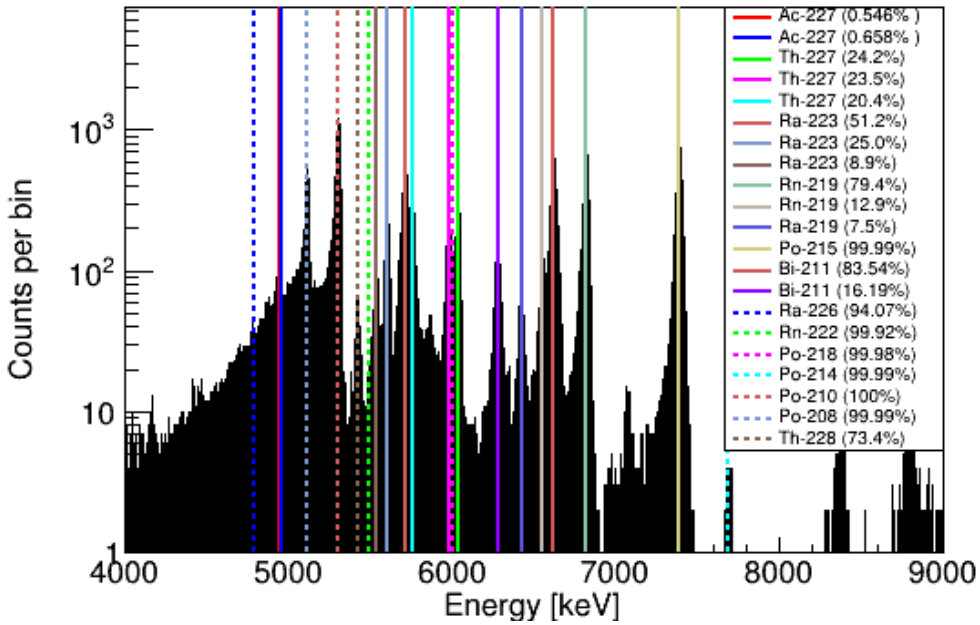

Figure 5.12: Spectrometry data from the May source, where the peaks are identified. Full lines represent isotopes from the decay chain of ^{227}Ac.

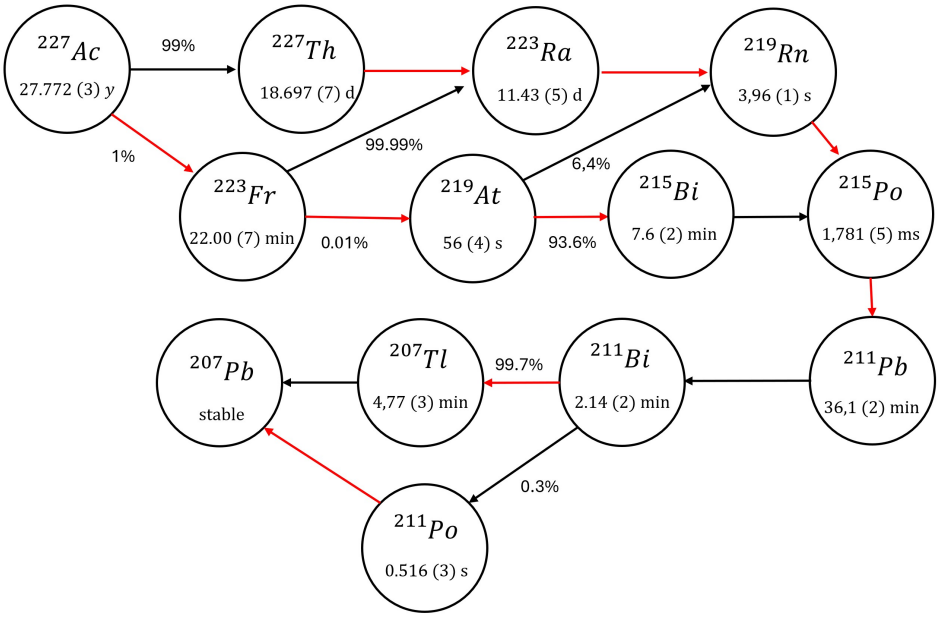

Figure 5.13: Decay chain of ^{227}Ac. Red arrows indicate α emission, black arrows β^-. Branching ratios and half-lives are retrieved from [73].

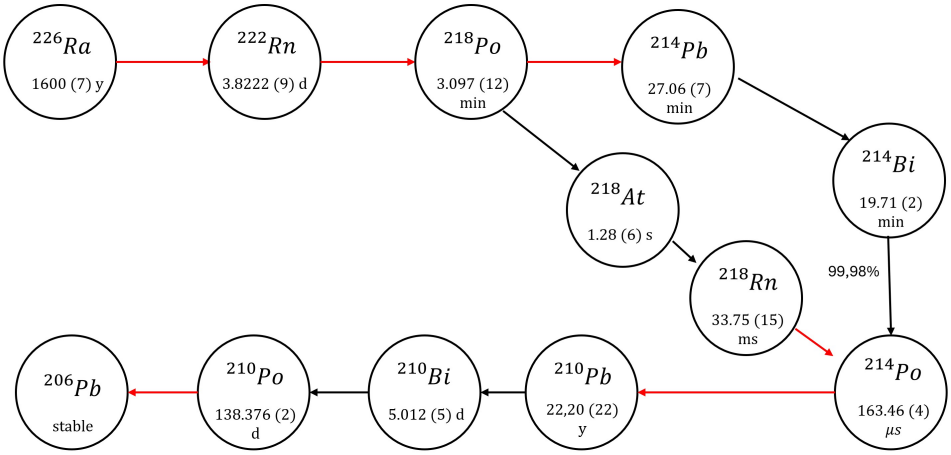

Figure 5.14: Decay chain of ^{226}Ra. Red arrows indicate α emission, black arrows β^-. Branching ratios and half-lives are retrieved from [73].

In order to determine the activity of ^{227}Ac, the following equation was used:

$$A(t) = \frac{r}{\epsilon_{geo}\epsilon_{det}} = \frac{r}{\epsilon_{geo}}, \tag{5.3}$$

where A is the activity, r the rate with $r = \frac{Amount\ of\ counts}{time}$, ϵ_{geo} the geometric efficiency and ϵ_{det} the detector efficiency. The latter can be assumed to be 1 for alpha particles, as all particles which reach the detector, will induce ionization [75]. For the determination of the geometric efficiency ϵ_{geo}, the triple alpha source was used. The detector was also placed at a distance of 9 mm from the source. With the given activities from table 5.1 and inverting equation 5.3, the geometric efficiency could be determined by

$$\epsilon_{geo} = \frac{r}{A(t)\epsilon_{det}}. \tag{5.4}$$

This equation was determined for the three different isotopes of the calibration source, which resulted in a mean ϵ_{geo} of 0.146 ± 0.012. The rate in equation 5.3 was calculated for prominent peaks in the data (see figures 5.15 and 5.16), notable in the sense that no other peaks overlapped, allowing the number of counts to be determined by integrating the energy spectrum over the peak. Knowing the rate and efficiency, the activity could be calculated with equation 5.3.

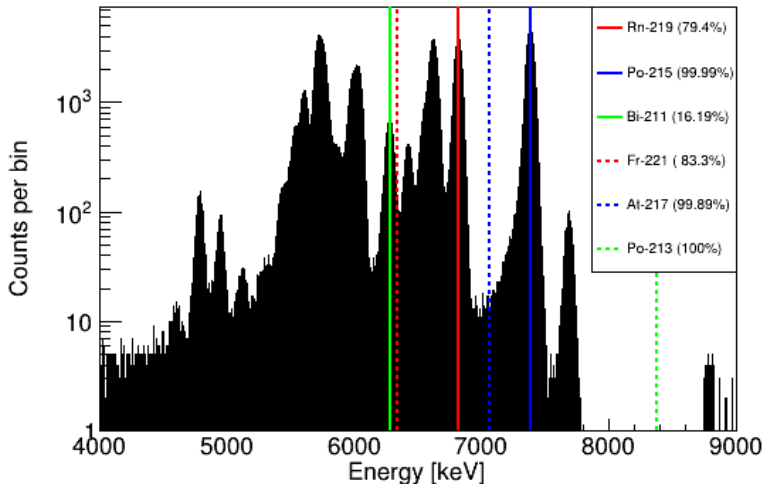

Figure 5.15: Data from the December source with prominent peaks marked (full lines) for activity estimation. Dotted lines represent elements from the decay chain of ^{225}Ac.

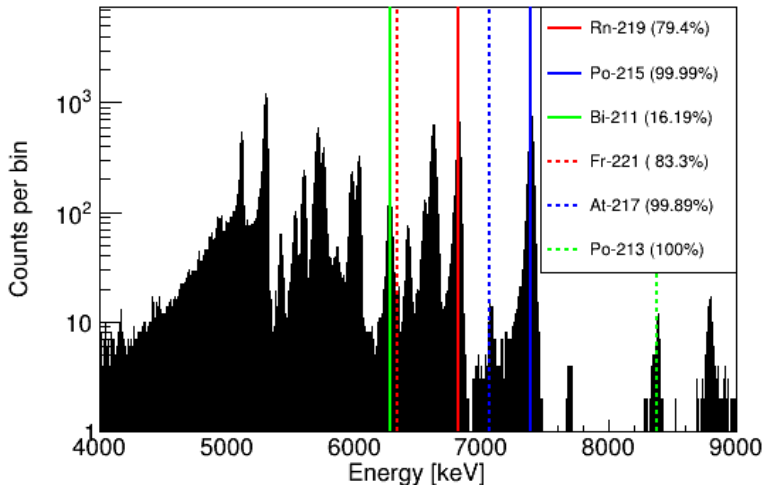

Figure 5.16: Data from the May source with prominent peaks marked (full lines) for activity estimation. Dotted lines represent elements from the decay chain of ^{225}Ac.

However, a correction factor can be taken into account in the determination of the activity, which arises from the recoil effect with alpha emission. When the collection sample is placed in front of the detector, recoiled daughter nuclei can become implanted on the detector, altering the geometric efficiency of the setup. This effect can be further complicated as these implanted daughter nuclei may recoil back onto the foil and then return to the detector repeatedly, a phenomenon known as the "ping pong" effect. This means that the correction factor increases further along the decay chain, as more recoiling changes the distribution of the nuclei. This effect can be simulated using SRIM (Stopping power and Range of Ions in Matter), which provides a correction factor that accounts for these interactions. J. D. Johnson has conducted such simulations, with the resulting correction factors presented in table 5.3 [76]. By using the corrected value of the geometric efficiency ϵ_{geo} and the rate r of the prominent peaks, the activity of several isotopes were determined, which can be found in table 5.4.

Table 5.3: The correction factors on the geometric efficiency for each isotope, incorporating the 'ping pong' effect. Values retrieved from [76].

^{215}Po	^{219}Rn	^{211}Bi
0.85809 ± 0.05987	0.84698 ± 0.06019	0.85809 ± 0.05988

Table 5.4: The determined activities from prominent peaks of the December and May source. The error is one standard deviation, where the highest contribution comes from ϵ_{geo}.

Run	A of ^{215}Po [Bq]	A of ^{219}Rn [Bq]	A of ^{211}Bi [Bq]
December	3.634 ± 0.392	3.471 ± 0.380	3.221 ± 0.349
May	0.237 ± 0.026	0.240 ± 0.026	0.267 ± 0.029

For the run of December, the initial activity of collected ^{227}Ac could be determined directly from the isotope itself. The initial activity could be straightforwardly determined by using 5.1. However, since the error is significant on the activity due to the low counts and relative high background, these data is not used for further analysis. Using the values from table 5.4, the activity of the parent nucleus ^{227}Ac was determined. This cannot be done using 5.1, as radioactive daughter nuclei are both generated and decaying simultaneously. This phenomenon can be represented by the following differential equation

$$\frac{dN_i}{dt} = \lambda_{i-1}N_{i-1} - \lambda_i N_i \quad (i = 2, n), \tag{5.5}$$

where λ_i is the decay constant and N_i the total amount of the ith nuclide in the decay chain. If at the end of production time, $t = 0$, no daughter nuclei were present, then the total number of the nth nuclide is given by Bateman's equation [69]:

$$N_n(t) = \frac{N_1(0)}{\lambda_n} \sum_{i=1}^{n} \lambda_i \alpha_i exp(-\lambda_i t), \tag{5.6}$$

where

$$\alpha_i = \prod_{j=1, j\neq i}^{n} \frac{\lambda_j}{\lambda_j - \lambda_i}.$$

It is thus apparent that equation 5.6 only works if the decay constants are different in the decay chain, since otherwise infinity occurs. Using the half-lives of the decay chain (see figure 5.13) the decay constants λ_i were calculated. By using the relation $A = \lambda N$, the initial activity of ^{227}Ac could be determined, which are given in table 5.5. Here, it can be noted that the value of ^{211}Bi ranges from the lowest value in December to the highest in May. This is due to the difference in overlap with other energy peaks. Due to the dependence on the background, this value is not further used in the calculation of the separation enhancement factor. The determined activity of ^{227}Ac was then 3.71 ± 0.26 Bq and 0.244 ± 0.019 Bq at EOC for the December and May runs respectively.

Table 5.5: The initial activities of ^{227}Ac of the two samples, calculated from 3 different peaks: ^{215}Po, ^{219}Rn and ^{211}Bi.

	$A_{initial}$ of ^{227}Ac [Bq]
December	^{215}Po: 3.809 ± 0.411
	^{219}Rn: 3.617 ± 0.397
	^{211}Bi: 3.376 ± 0.366
May	^{215}Po: 0.242 ± 0.026
	^{219}Rn: 0.245 ± 0.027
	^{211}Bi: 0.274 ± 0.030

5.5 Discussion

In this section, the results are discussed from the two alpha spectrometry measurements. The main part was the calculation of the ^{227}Ac contamination, which was essential for discussing the separation enhancement factor. The presence of other contaminants are discussed afterwards. At the end, a short comment is given on the time evolution of the data and the geometric efficiency, where measures could be taken to increase the precision of the results.

Separation enhancement factor

The goal of this experimental work was to determine the separation enhancement factor of the mass separation of the two actinium isotopes, which is given by

$$spf = \frac{\left(\frac{^{225}\mathrm{Ac}}{^{227}\mathrm{Ac}}\right)_{end}}{\left(\frac{^{225}\mathrm{Ac}}{^{227}\mathrm{Ac}}\right)_{start}}, \tag{5.7}$$

where the start indicates the activity in the radioactive target before extraction, and the end the collected activity of a certain isotope after separation. Only $^{227}\mathrm{Ac}_{end}$ was determined in this work. The other activities can be found in table 5.6. It is noticeable that the error on the starting activities is greater for the run in May than for December. This is due to the difference in target preparation, as discussed in section 5.1. The activities after proton irradiation are simulated using FLUKA, a Monte Carlo approach. The activities from December are based on the amount of actinium deposited on the target matrix. The activity of ^{225}Ac at the end of collection is determined by gamma spectrometry with a HPGe detector.

Table 5.6: The activities of ^{225}Ac and ^{227}Ac at the start of extraction in the target and of ^{225}Ac on the collection foil at the end of extraction.

	$^{225}\mathrm{Ac}_{\mathrm{start}}$ [MBq]	$^{227}\mathrm{Ac}_{\mathrm{start}}$ [MBq]	$^{225}\mathrm{Ac}_{\mathrm{end}}$ [MBq]
December	10.7900 ± 0.3237	0.100 ± 0.003	0.0574 ± 0.0022
May	1030 ± 30	1.640 ± 0.020	0.0967 ± 0.0037

By using the values of table 5.6 and the mean value of table 5.5 (excluding the value from ^{211}Bi), the separation enhancement factor could be calculated using equation 5.7, where the results are shown in table 5.7.

Table 5.7: The separation enhancement factors spf of two mass separation runs at CERN-MEDICIS.

run	spf
December	150 ± 14
May	646 ± 59

These data indicate that for these runs, the separation technique can reduce the ratio of ^{225}Ac to ^{227}Ac by at least two orders of magnitude. The variations in separation factor errors between the two runs are due to differences in target preparation. Notably, the values of the separation factor vary significantly between the two runs, primarily because of difficulties experienced during the December run. Problems were experienced with the vacuum and magnet calibration was not in order as the extraction electrode worked at 50 kV instead of 60 kV. Despite these issues, the December run retrieved a higher percentage of ^{225}Ac from the target, but ^{227}Ac as well. This was because the actinium did not need to diffuse out of the target material, making it easier to extract atomic vapour from the target. Even though the May run had a larger amount of ^{227}Ac in the target, a lower activity of the contaminant was collected on the foil compared to December. This highlights that the experimental conditions strongly influence the separation enhancement.

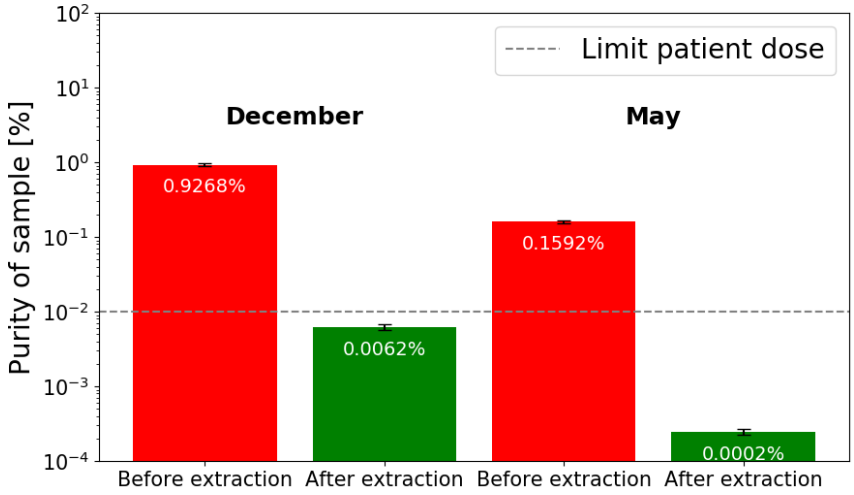

Figure 5.17: The ratios of ^{227}Ac to ^{225}Ac before and after separation. The dotted line represents the exemption ratio for a patient dose of 10 MBq.

In order to assess if the separating property suffices for medical endpoints, the maximum ratio of ^{225}Ac to ^{227}Ac of a patient dose should be estimated. As a typical patient dose consists of 10 MBq and knowing that the exemption level of ^{227}Ac is 1 kBq, the maximum ratio is 0.01% (in Europe). By looking at figure 5.17, it can be noted that the initial ratio was above this limit, which is the reason mass separation was performed. After performing RIMS, it can be seen that for the two runs, the ratio is below the limit, making the samples useful for medical endpoints. Despite the challenges of the technique, RIMS shows promise as a method to suppress ^{227}Ac contamination, making high energy proton irradiation of thorium-based targets

a viable option for ^{225}Ac production if the necessary infrastructure is available. A combination of radio-chemical separation and RIMS after irradiation can effectively isolate a pure sample of ^{225}Ac for medical use.

The method used to quantify the collected activity of ^{227}Ac, while straightforward, is impractical. By waiting a long time, ^{225}Ac and its daughters decay sufficiently, allowing the decay chain of ^{227}Ac to be measured. However, this method is not time-efficient, and given the need for further research into this separation technique, it is not feasible to calculate the separation enhancement factor using this method every time. For instance, the ^{225}Ac activity was 10% of the activity of ^{227}Ac after approximately 171 and 218 days after EOC for December and May, respectively. Therefore, it should be used as an additional check to validate other quantification methods for this contaminant. Another approach to determine ^{227}Ac activity is through recoil implantation. This method is illustrated in figure 5.18, where the collection foil is positioned in front of the detector. Due to conservation of momentum, nuclei can escape the collection foil after alpha emission and are captured on the detector. By performing a measurement without the collection foil in front of the detector, the activity of the daughter nuclei could be determined, which can be used to estimate the original activity of the parent isotope on the foil. This method can be performed after approximately a day, as the daughter nuclei of ^{225}Ac are decayed away due to their shorter half-life. This novel method provides a more time-efficient way to quantify the separation enhancement factor, yielding similar results [67]. An alternative method to quantify ^{227}Ac is decay energy spectrometry, as described by A.D. Tollefson et al. [10]. This novel approach quantifies the energy from each discrete decay event in a sample using an ultra-sensitive microcalorimeter, achieving 100% detection efficiency with high energy resolution. In this work, the contamination of ^{227}Ac was identified 30 days after EOC.

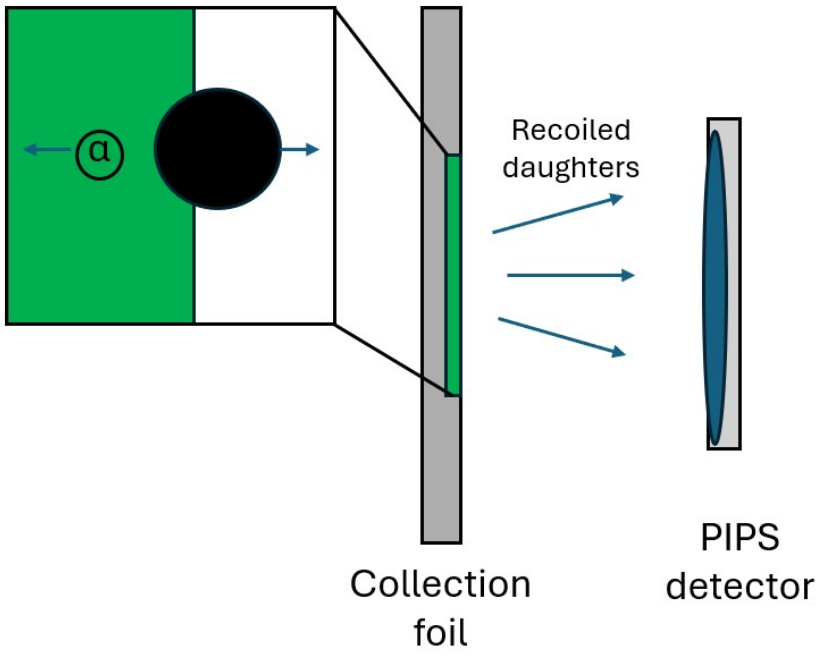

Figure 5.18: Visual representation of recoil implantation. The collection foil is removed from its position after implantation, such that a spectrometry measurement can be performed on the recoiled isotopes to quantify the ^{227}Ac on the collection foil.

Other contaminants

As mentioned earlier, ^{227}Ac was not the only contaminant identified on the collection samples (see figures 5.11 and 5.12). On both foils, the decay chain of ^{226}Ra was identified. This was unexpected for the extraction run of December, as only actinium was deposited on a thorium-carbide target. This suggests that the target contained ^{226}Ra prior to preparation. Using the prominent peak of ^{214}Po in the decay chain, the original activity of ^{226}Ra could be determined in the same way as with ^{227}Ac, which suggested an original activity of 67 ± 7 mBq of ^{226}Ra. For the December run, the peak of ^{226}Ra itself could also be used for determining the initial activity, but a low count rate and relative high background rendered it difficult to gain good results. For the May run, the high background made it difficult to identify the contribution of ^{226}Ra directly. As the prominent peak of ^{214}Po had a low count rate, the activity of ^{226}Ra was not estimated.

For the May run, more contaminants were identified. Relative high count rates were detected from ^{208}Po, an isotope unexpectedly present in the sample. By examining possible channels for ^{208}Po production, no feasible parent nuclei could be identified which could be collected on the foil. For the ASET setup at KU Leuven, a background measurement was performed, but no significant counts were present to explain the unexpected counts. Due to peak overlap, it was challenging to isolate counts solely from ^{208}Po to give an accurate activity estimate. The origin of this isotope is still under investigation.

To summarize, in every run, unexpected contaminants such as ^{226}Ra and ^{208}Po were identified. Background measurements can be taken before extraction runs to prevent such situations. However, performing these for every target would be time-inefficient, especially as production scales up. The unexpected contaminants could originate from the target before extraction, from preparation at the external facilities, previous runs in the mass separation setup, or from the ISOLDE setup (as the May target originated from there). By keeping these factors in mind, future experiments can be better prepared for and adapted to avoid unexpected contaminants. However, it should be noted that the unexpected isotopes would be separated from the medical end product of ^{225}Ac via radiochemistry.

Time evolution of alpha peaks

As the two experiments lasted four and six days respectively, the time behavior of the alpha peaks was analyzed. Figure 5.19 shows the time evolution of the centroid values μ of the prominent ^{215}Po peak, which was used for the determination of the ^{227}Ac activity. It can be seen that the centroid value is increased by 3 channel numbers over six days. This time evolution is not due to variations in alpha energy but is inherent to the functioning of the electronics in the experimental setup. This behavior is likely associated with the preamplifier, given its high sensitivity, though it could also be related to the digitizer's functionality, such as imperfect baseline restoration. If high precision is required, the data for these peaks could be corrected and shifted to eliminate this electronic effect. However, such precision was unnecessary for this work, as isotope identification remained possible. The same issue was observed in the calibration measurement, where an increase of two channels was noted overnight. Correcting for this effect would reduce the error in the calibration parameters.

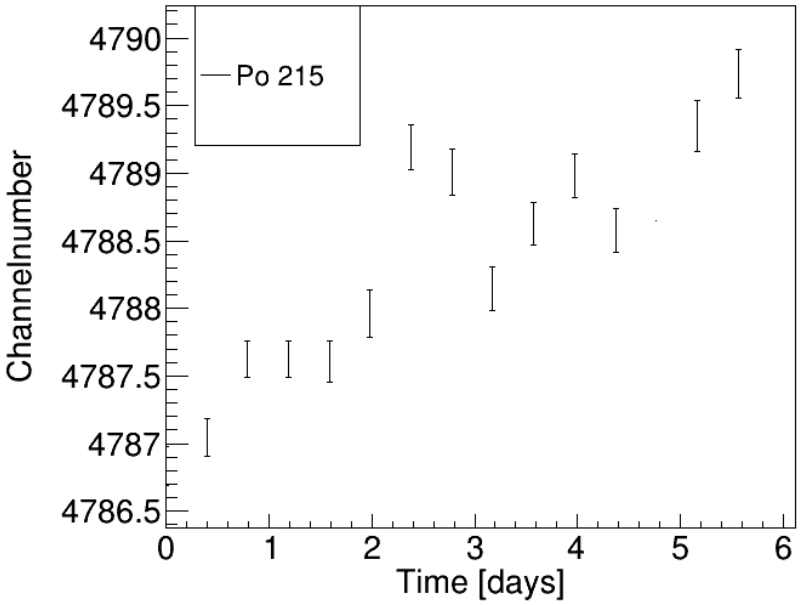

Figure 5.19: Time behavior of the mean of the peak values from the alpha decay of ^{215}Po of the sample of May.

Geometric efficiency

The geometric efficiency was determined by using the triple alpha source in the same experimental configuration. By determining the rate and using the known activities, the efficiency was determined to be 0.146 ± 0.012 (using no correction factor), which could be compared with theoretically determined efficiencies. The expression for a point source is given by:

$$\Omega_{point} = \frac{1}{2}(1 - \frac{d}{\sqrt{d^2 + R^2}}), \tag{5.8}$$

where d is the distance from source to detector and R the radius of the detector. A larger geometric efficiency is determined using a point source, which may suggest a point source approximation is not ideal. Different expression for a circular source were used, but no physical results were determined [77]. This could suggest an off axis placement of the source w.r.t. the detector or the dimensions of the setup are not ideal for the used expressions. No further analysis is done of the geometric efficiency. Possible solutions to validate the geometric efficiency is by using the simulation program SRIM. As the error on the geometric efficiency is the main contributor to the activity determination, it could be beneficial to increase the precision of this value. This could either be done by increasing the time of measurement or by a more precise determination of the activity on the calibration source.

Table 5.8: The geometric efficiency ϵ_{geo}, where the distance $d = 9 \pm 0.01$ mm, $A_{det} = 300 \pm 1$ mm^2 . The calibration value comes from equation 5.4, where the error comes from the Poisson noise of the data and the activity of the calibration source.

Calibration	Point source
0.146 ± 0.012	0.161 ± 0.002

6. Conclusions

The goal of this work was to determine the feasibility of the production pathway of high energy proton irradiation of a thorium based target. This production pathway necessitates mass separation, as ^{227}Ac is co-produced. This step in the production process is discussed by an analysis the ion beam current measured by a PAM in the experimental setup and by determining the separation enhancement factor of the mass separation.

Based upon the data of the ion beam current, an estimation was done for the collected activity on the foils of three different experimental runs at CERN-MEDICIS. To achieve this, the background current had to be estimated, coming from the decay of collected radioactive isotopes. This was done either via an empirical fit (polynomial or exponential) or by linear interpolation. Both methods did not capture the complex behaviour of the background data, but however gave relative good agreement with the values of the gamma spectrometry measurement done after collection. However, the determined values underestimated the measured values by gamma spectrometry. On top of the underestimation of the activity, the error determined is also expected to underestimate the real uncertainty on the activity. A deeper analysis in the workings of the PAM placed in the experimental setup or analysis in the background current could clarify the determined estimations. The correlation between beam current and background current can be modelled using the Bateman equation, simulating the effect of emitted or recoiled particles from the foil.

For foils MS-021 (May run) and MS-022 (June run), a larger underestimation can be noted. This was expected, as both ^{225}Ra and ^{225}Ac were collected on those foils and the activity of ^{225}Ac measured by gamma spectrometry does not distinguish between the generated ^{225}Ac coming from the parent nucleus ^{225}Ra on the foil and the ^{225}Ac coming directly from the ion beam. The analysis of the ion beam current data thus allows for the determination of solely extracted ^{225}Ac, excluding the feeding effect of ^{225}Ra. This allows for a better understanding of the properties needed to increase the efficiency of extracted ^{225}Ac. The feeding effect of the ^{225}Ac was simulated for both foils, but as the original amount of ^{225}Ra was underestimated, the resulting activity of ^{225}Ac were underestimated by $65.1 \pm 1.9\%$ and $14.3 \pm 9\%$ for foils MS-021 and MS-022 respectively. The high underestimation for foil MS-021 is still under investigation.

Still, despite the underestimations, the determined values of directly collected ^{225}Ac could be compared between the run of May and June. It was expected that the extraction efficiency was lower for the second run, due to the sintering of the target after the May run. Even though more ^{225}Ac is extracted in the run of June due to the twice as long duration, the extracted ^{225}Ac per hour was more than halved. For the parent nucleus of ^{225}Ra, less than half of the amount of Ra was collected in the June run. This suggests that sintering prevented some ^{225}Ra from escaping the target.

By investigating the laser on/off effect on the collected current, the apparent laser enhancement could be calculated. The calculated values suggested that the laser ionization at least doubles the collected current. The time evolution of the enhancement depended on the viability of the background fit, which is worse for relative long time periods and low amount of background data.
Besides the apparent laser enhancement, estimations could be made on the collected activity solely coming from the laser ionization. This was done in a similar way as for the activity estimations on the foils, which gave approximately 1 MBq for the run of May and June. It could be seen that the rate of collection decreased towards the end of the collection, which makes sense as the most isotopes are already released from the target. For the foils which were put in after the first observation of the laser on/off effect, the true laser enhancement could be determined using the values from gamma spectrometry and the determined gain in activity from the lasers. This was calculated for two foils in the May run and one foil in the June run, which resulted in values ranging from 1.7 to 1.9. It was expected that the apparent laser enhancement would be larger, suggesting that either the background estimation in not accurate enough, the gain in activity is underestimating the real activity or that the laser powers changed during the run.

A necessary prerequisite for performing this analysis was access to the logbook and collection reports from the various extraction runs. These documents provided crucial information about the isotopes collected and the timings of collection. Since this information was not available in the logbook for August, no analysis could be performed for that run. This highlights the importance of maintaining accurate and thorough documentation.

In the second part of the thesis, the separation enhancement factor was determined for two experimental runs performed at CERN-MEDICIS (December and May). This was done by performing an alpha spectrometry measurement, where the activity of the ^{227}Ac was determined using prominent peaks of the daughter nuclei ^{215}Po and ^{219}Rn. The activity of collected ^{225}Ac after separation was determined using gamma spectrometry and was performed after collection. The activities of actinium in both targets were calculated in different ways. This is because target preparation differed, as for in December, the target was not irradiated but ^{225}Ac and ^{227}Ac were deposited on the thorium-based target. For the run of May, FLUKA simulations were performed to estimate the produced actinium in the target. The preparation of December would result in a higher extraction efficiency, as the actinium does not have to diffuse out of the target material. However, due to experimental issues, the extraction efficiency of this run was lower than expected, which ultimately influenced the value of the separation enhancement factor. For the two different runs, a separation factor of 150 ± 14 and 646 ± 59 was determined for respectively December and May. This thus emphasizes the dependence on experimental conditions.
The determination of the separation enhancement factor relied on the activity estimation of ^{227}Ac. Alpha spectrometry for assessing the ^{227}Ac activity can only be performed when the decay chain of ^{225}Ac is sufficiently suppressed. This requires a relatively long waiting period, making it not time-efficient. Specifically for these foils, the ^{225}Ac activity was 10% of the activity of ^{227}Ac after approximately 171 and 218 days after EOC for December and May, respectively. Therefore, alternative methods should be explored to quantify the ^{227}Ac contaminant, with the method used in this work serving only as a validation tool. Two possible approaches are discussed in section 5.5.The first approach utilizes conservation of

momentum in alpha emission, which can result recoiled daughter nuclei being collected on the detector. This method allows for the calculation of ^{227}Ac contamination after approximately one day. This analysis was performed by J. D. Johnson et al. and the values from this work were compared with this method [67]. Another approach is decay energy spectroscopy, which quantifies ^{227}Ac using an ultra-sensitive microcalorimeter. In the work of Tollefson et al., ^{227}Ac contamination was assessed 30 days after collection [10].

In addition to ^{227}Ac, two unexpected contaminants were identified: ^{208}Po and ^{226}Ra. The origins of these contaminants are still under investigation. It should be noted that these isotopes can be separated from actinium using radiochemistry, so this would not influence the purity of the medical product. However, this should be carefully addressed towards waste management.

The goal of the separation process could be assessed, which is patient administration. The maximum allowable ratio of ^{227}Ac to ^{225}Ac in patient doses is determined to be 0.01%, which is based on a 10 MBq patient dose of ^{225}Ac and Europe's exemption level of 1 kBq of ^{227}Ac. Using this limit, the suitability of the collected samples for patient administration can be evaluated. Figure 5.17 demonstrates that, for both runs, the extracted product meets the medical standards, indicating that the separation process is successful. However, this does not imply that the separation process is ready for scaling up production, as extraction efficiencies need to be improved. This can only be achieved through further research.

Even though the current separation meets medical requirements, the extent of separation was expected to be higher based on the magnet's mass resolving power (approximately 400). A potential hypothesis for this discrepancy is the presence of non-ionized residual gas in the experimental setup, which scatters the incoming ion beam. Parameters, such as the energy spread, magnification, emittance and dispersion influence the separation of the isotope of interest [78]. Further research is required to identify the underlying cause of this issue.

To summarize this thesis, two separate analyses were performed. The measured ion beam current provided systematic information about the collection properties. The determined activities on the collection foils were in relative good agreement with the measured values determined with gamma spectrometry, but a consistent underestimation in the activity is observed. Additionally, this technique enabled to distinguish the origin of collected ^{225}Ac, which can either be generated by the collected parent nucleus ^{225}Ra on the foil or directly collected from the ion beam. It was observed that for the runs in May and June, the majority of collected ^{225}Ac was generated from its parent. Besides the total activity collected on the foil, the influence of the lasers was determined. An estimate of the total collected activity from the ionizing lasers could be determined and the apparent/true laser enhancement. The determined values in this analysis serve to deepen the understanding of the collection conditions, ultimately aiming to increase extraction efficiency. However, other properties of the experimental setup should also be investigated due to the complexity of the experiment. Regarding the second part of the analysis in this thesis, the separation of actinium isotopes obtained in this work suggest a separation enhancement factor that is sufficient for medical applications. This indicates that the challenge associated with the production pathway for irradiating a thorium-based target can be resolved. However, further research is needed to validate the consistency of the separation factor and ultimately to increase the extraction efficiency to meet global demand.

Bibliography

[1] World Health Organization. Global Cancer Burden Growing, Amidst Mounting Need for Services. https://www.who.int/news/item/01-02-2024-global-cancer-burden-growing--amidst-mounting-need-for-services, February 2024. Accessed: 2024-05-30.

[2] David A. Olle. *Chapter 8: Chemotherapy*, pages 67–70. Mercury Learning and Information, Berlin, Boston, 2022.

[3] Jeantine de Feijter, Hilda Houwer, and Anouk Meekel. Wat is chemotherapie? kanker.nl, May 2021. https://www.kanker.nl/soorten-behandelingen/chemotherapie/algemeen/wat-is-chemotherapie.

[4] Xiaojuan Hou, Jinghua Jiang, Zhiqiang Tian, et al. *Autophagy and Tumour Chemotherapy*, pages 351–374. Springer Singapore, Singapore, 2020.

[5] Karolien Goffin. Session 1: Technology and Techniques in Nuclear Medicine. [*Course presentation*], February 2024. KU Leuven.

[6] Jake D. Johnson, Michael Heines, Frank Bruchertseifer, et al. Resonant laser ionization and mass separation of Ac-225. *Scientific reports*, 13(1):1347–1347, 2023.

[7] Alfred Morgenstern, Christos Apostolidis, and Frank Bruchertseifer. Supply and Clinical Application of Actinium-225 and Bismuth-213. *Seminars in nuclear medicine*, 50(2):119–123, 2020.

[8] Frank Bruchertseifer, Alban Kellerbauer, Rikard Malmbeck, et al. Targeted alpha therapy with bismuth-213 and actinium-225: Meeting future demand. *Journal of labelled compounds radiopharmaceuticals*, 62(11):794–802, 2019.

[9] George Sgouros, Bin He, Nitya Ray, et al. Dosimetric impact of Ac-227 in accelerator-produced Ac-225 for alpha-emitter radiopharmaceutical therapy of patients with hematological malignancies: a pharmacokinetic modeling analysis. *EJNMMI physics*, 8(1):60–60, 2021.

[10] A.D. Tollefson, C.M. Smith, M.H. Carpenter, et al. Measurement of Ac-227 impurity in Ac-225 using decay energy spectroscopy. *Applied radiation and isotopes*, 172:109693–109693, 2021.

[11] C. Bernerd, J.D. Johnson, E. Aubert, et al. Production of innovative radionuclides for medical applications at the CERN-MEDICIS facility. *Nuclear instruments methods in*

physics research. Section B, Beam interactions with materials and atoms, 542:137–143, 2023.

[12] Rebecca Abergel, Dahlia An, Andrew Lakes, et al. Actinium Biokinetics and Dosimetry: What is the Impact of Ac-227 in Accelerator-Produced Ac-225? *Journal of medical imaging and radiation sciences*.

[13] MEDICIS. Overview of the CERN-MEDICIS facility, 2024. `https://medicis.cern/overview-of-the-MEDICIS-facility`.

[14] Stanley J. Goldsmith. Targeted Radionuclide Therapy: A Historical and Personal Review. *Seminars in nuclear medicine*, 50(1):87–97, 2020.

[15] Koen Vermeulen, Mathilde Vandamme, Guy Bormans, et al. Design and Challenges of Radiopharmaceuticals. *Seminars in Nuclear Medicine*, 2019.

[16] Andrea Galindo. What are radiopharmaceuticals? IAEA, 2024. Figure 2: components of a radiopharmaceutical.

[17] Shankar Vallabhajosula. *Molecular imaging and targeted therapy: Radiopharmaceuticals and clinical applications*, chapter 1, pages 12–18. Springer Nature Switzerland AG, Cham, Switzerland, second edition edition, 2023.

[18] Russ F. Knapp and Ashutosh Dash. Alpha Radionuclide Therapy. In *Radiopharmaceuticals for Therapy*, chapter 3, pages 37–53. Springer India, New Delhi, 1st edition, 2016.

[19] Suliman Salih, Ajnas Alkatheeri, Wijdan Alomaim, et al. Radiopharmaceutical Treatments for Cancer Therapy, Radionuclides Characteristics, Applications, and Challenges. *Molecules (Basel, Switzerland)*, 27(16):5231–, 2022.

[20] Torgny Stigbrand, Gregory P. Adams, and Jörgen Carlsson. Radiation Induced DNA-Damage/Repair and Associated Signaling Pathways. In *Targeted Radionuclide Tumor Therapy: Biological Aspects*, chapter 13, pages 250–265. Springer Netherlands, Dordrecht, 1. aufl. edition, 2009.

[21] Katalin Balázs, Lilla Antal, Géza Sáfrány, et al. Blood-Derived Biomarkers of Diagnosis, Prognosis and Therapy Response in Prostate Cancer Patients. *Journal of personalized medicine*, 11(4):296–, 2021.

[22] Jean-Pierre Pouget and Julie Constanzo. Revisiting the Radiobiology of Targeted Alpha Therapy. *Frontiers in medicine*, 8:692436–692436, 2021.

[23] Torgny Stigbrand, Gregory P. Adams, and Jörgen Carlsson. High-LET-Emitting Radionuclides for Cancer Therapy. In *Targeted Radionuclide Tumor Therapy: Biological Aspects*, chapter 9, pages 175–180. Springer Netherlands, Dordrecht, 1. aufl. edition, 2009.

[24] Joseph G. Jurcic, Steven M. Larson, George Sgouros, et al. Targeted alpha particle immunotherapy for myeloid leukemia. *Blood*, 100(4):1233–1239, 2002.

[25] C. Parker, S. Nilsson, D. Heinrich, et al. Alpha Emitter Radium-223 and Survival in Metastatic Prostate Cancer. *The New England journal of medicine*, 369(3):213–223, 2013.

[26] National Library of Medicine. ClinicalTrials.gov. `https://clinicaltrials.gov/search`, 2024. Accessed: 2024-05-30.

[27] Clemens Kratochwil, Frank Bruchertseifer, Frederik L. Giesel, et al. Ac-225-PSMA-617 for PSMA-Targeted alpha-Radiation Therapy of Metastatic Castration-Resistant Prostate Cancer. *Journal of Nuclear Medicine*, 57(12):1941–1944, 2016.

[28] Martina Benesová, Martin Schäfer, Ulrike Bauder-Wüst, et al. Preclinical evaluation of a tailor-made DOTA-conjugated PSMA inhibitor with optimized linker moiety for imaging and endoradiotherapy of prostate cancer. *Journal of Nuclear Medicine*, 56(6):914–920, 2015.

[29] Dayana Castillo Seoane, Marijke de Saint-Hubert, Melissa Crabbe, et al. Targeted alpha therapy: a critical review of translational dosimetry research with emphasis on actinium-225. *Quarterly Journal Of Nuclear Medicine And Molecular Imaging*, 2020.

[30] Sven van den Berghe. Pantera. In *9th ISMERAD — Alpha Therapy: New approaches in radionuclide therapy*, Gent, Belgium, April 2024. SCK CEN.

[31] Robin M. de Kruijff, Hubert T. Wolterbeek, and Antonia G. Denkova. A critical review of alpha radionuclide therapy-how to deal with recoiling daughters? *Pharmaceuticals (Basel, Switzerland)*, 8(2):321–336, 2015.

[32] Stephen Tronchin, Jake Forster, Kevin Hickson, et al. Modeling the effect of daughter migration on dosimetry estimates for unlabeled actinium-225. *Medical physics (Lancaster)*, 2024.

[33] Clemens Kratochwil, Frank Bruchertseifer, Hendrik Rathke, et al. Targeted -Therapy of Metastatic Castration-Resistant Prostate Cancer with Ac-225-PSMA-617: Dosimetry Estimate and Empiric Dose Finding. *Journal of Nuclear Medicine*, 58(10):1624–1631, 2017.

[34] Meltem Ocak, Türkay Toklu, Emre Demirci, et al. Post-therapy imaging of Ac-225-DOTATATE treatment in a patient with recurrent neuroendocrine tumor. *European journal of nuclear medicine and molecular imaging*, 47(11):2711–2712, 2020.

[35] Edmond Sterpin. Techniques in radiotherapy: basic radiation oncology. Lecture, UC Louvain, 2023. Slide 41: The deal of RT.

[36] Robert Alvarez. Managing the Uranium-233 Stockpile of the United States. *Science global security*, 21(1):53–69, 2013.

[37] J. D. Johnson and C. Bernerd. Optimized Production Scheme for Ac-225. Review Report D3.2, KU Leuven and CERN, Leuven, Belgium, August 2023. Deliverable for the LISA project under the Marie Sklodowska-Curie Actions, Grant Agreement No. 861198.

[38] Andrew K. H. Robertsona, Caterina F. Ramogidaa, and Pauland R. Schaffera. Development of Ac-225 Radiopharmaceuticals: TRIUMF Perspectives and Experiences. *Current radiopharmaceuticals*, 2018.

[39] Pantera. About actinium-225, 2024. https://pantera-life.com/about-actinium-225/.

[40] Pantera. TerraPower Isotopes, 2024. https://www.terrapower.com/our-work/terrapower-isotopes/.

[41] Fusion Pharmaceuticals. Fusion Pharmaceuticals Strengthens Actinium Supply With Onsite Isotope Production Through Expanded BWXT Medical Collaboration, 2024. https://ir.fusionpharma.com/2023-11-16-Fusion-Pharmaceuticals-Strengthens-Actinium-Supply-with-Onsite-Isotope-Production-through-Expanded-BWXT-Medical-Collaboration.

[42] Actinium Parmaceuticals. Actinium-225 Technology, 2024. https://www.actiniumpharma.com/actinium-225-technology.

[43] Spectronx. Global Isotope Procurement, 2024. https://www.spectronrx.com/home/contract_manufacturing/isotopes/.

[44] Northstar. Development: Northstar's manufacturing, 2024. https://www.northstarnm.com/development/manufacturing/.

[45] Prismap. Project description, 2024. https://www.prismap.eu/about/project/.

[46] C. Apostolidis, R. Molinet, J. McGinley, et al. Cyclotron production of Ac-225 for targeted alpha therapy. *Applied radiation and isotopes*, 62(3):383–387, 2005.

[47] H. Kumawat and S. V. Suryanarayana. Accelerator Based Production of ^{225}Ac for Cancer Treatment. *arXiv.org*, 2020.

[48] IAEA. Cyclotrons used for Radionuclide Production, October 2023. https://nucleus.iaea.org/sites/accelerators/Pages/Cyclotron.aspx.

[49] Jonathan Morrell. Next-Generation Isotope Production via Deuteron Breakup, 2021.

[50] Justin R. Griswold, Carola U. Jost, Daniel W. Stracener, et al. Production of Th229 for medical applications: Excitation functions of low-energy protons on Th232 targets. *Physical review. C*, 98(4), 2018.

[51] Matthias Englert, Lindsay Krall, and Rodney C. Ewing. Is nuclear fission a sustainable source of energy? *MRS bulletin*, 37(4):417–424, 2012.

[52] George Sgouros, Bin He, Nitya Ray, et al. Dosimetric impact of Ac-227 in accelerator-produced Ac-225 for alpha-emitter radiopharmaceutical therapy of patients with hematological malignancies: a pharmacokinetic modeling analysis. *EJNMMI physics*, 8(1):1–16, 2021.

[53] E. Kugler, D. Fiander, B. Johnson, et al. The new CERN-ISOLDE on-line mass-separator facility at the PS-Booster. *Nuclear instruments methods in physics research. Section B, Beam interactions with materials and atoms*, 70(1):41–49, 1992.

[54] Yisel Martinez Palenzuela, Vincent Barozier, Eric Chevallay, et al. The CERN-MEDICIS Isotope Separator Beamline. *Frontiers in medicine*, 8:689281–689281, 2021.

[55] Bertrand Simon V Dewit and Thomas Elias Cocolios. Towards the first collection of 44Sc at CERN MEDICIS, 2017.

[56] Marie Deseyn and Thomas Elias Cocolios. Maximizing the radionuclide collection efficiency at CERN-MEDICIS: A case study on terbium collections and sputtering, 2023.

[57] Reis E. Radioactive Ion Beam Production via the ISOL method. In *IO meeting*, IKS, Leuven, February 2024. CERN.

[58] Paul Heitjans and Jörg Kärger. *Diffusion in condensed matter: methods, materials, models* . Springer, Berlin, 2005.

[59] L. Egoriti, S. Boeckx, L. Ghys, et al. Analytical model for release calculations in solid thin-foils ISOL targets. *Nuclear instruments methods in physics research. Section A, Accelerators, spectrometers, detectors and associated equipment*, 832:202–207, 2016.

[60] J.P. Ramos, A. Gottberg, T.M. Mendonça, et al. Intense 31–35Ar beams produced with a nanostructured CaO target at ISOLDE. *Nuclear Instruments and Methods in Physics Research Section B: Beam Interactions with Materials and Atoms*, 320:83–88, 2014.

[61] J.S Al-Khalili and Ernst Roeckl. *Nuclear Physics, Heavy Ions, Hadrons*, chapter 2, pages 37–75. Lecture Notes in Physics. Springer-Verlag, Berlin, Heidelberg, 2006 edition edition, 2006.

[62] J.P. Ramos. Thick solid targets for the production and online release of radioisotopes: The importance of the material characteristics – A review. *Nuclear instruments methods in physics research. Section B, Beam interactions with materials and atoms*, 463:201–210, 2020.

[63] R. Kirchner. On the thermoionization in hot cavities. *Nuclear instruments methods in physics research. Section A, Accelerators, spectrometers, detectors and associated equipment*, 292(2):203–208, 1990.

[64] Y. Liu, Y. Kawai, and H.Z. Bilheux. Characterization of A Tubular Hot-Cavity Surface Ionization Source. In *Proceedings of the 2005 Particle Accelerator Conference*, volume 2005, pages 1581–1583. IEEE, 2005.

[65] Helmut Liebl. *Lenses: Basic Optics*, pages 1–43. Springer Berlin Heidelberg, Berlin, Heidelberg, 2008.

[66] Charles A. Bishop. Chapter 7 - Mass Spectrometers, Helium Leak Detectors, and Residual Gas Analyzers. In Charles A. Bishop, editor, *Vacuum Deposition Onto Webs, Films and Foils (Third Edition)*, pages 139–145. William Andrew Publishing, Boston, third edition edition, 2015.

[67] Jake D. Johnson, Cyril Bernerd, Frank Bruchertseiffer, et al. Ac-227 Content of Resonance-Laser-Ionized and Mass-Separated Ac-225 Samples from Proton Spallation of Thick Th-Based Targets at CERN-MEDICIS. Technical report, KU Leuven, JRC, CERN, Leuven, Belgium; Karlsruhe, Germany; Geneva, Switzerland, 2023.

[68] Nuclear-Power. Radium – Melting Point – Boiling Point, November 2021. https://www.nuclear-power.com/radium-melting-point-boiling-point/.

[69] Jerzy Cetnar. General solution of Bateman equations for nuclear transmutations. *Annals of nuclear energy*, 33(7):640–645, 2006.

[70] E. Cortina. Semiconductor Detectors, Ionizing Radiation Detection and Nuclear Instrumentation. [*Course presentation*], February 2024. UCLouvain.

[71] Steven H. Simon. *The Oxford solid state basics*. Oxford university press, Oxford, 2013.

[72] CAEN. *MC2Analyzer User Manual, software for digital Multi Channel Analyzer*, 2023. User Manual UM3182.

[73] IAEA. Live Chart of Nuclides, November 2023. https://www-nds.iaea.org/relnsd/vcharthtml/VChartHTML.html.

[74] R. Dmitry. Crystal ball function. https://www.jlab.org/primex/weekly_meetings/slides_2009_07_17/dmitry/crystalball.html, February 2024. Accessed: 2024-05-30.

[75] William R. Leo. *Techniques for nuclear and particle physics experiments: a how-to approach*. Springer, Berlin, 2nd rev. ed. edition, 1994.

[76] Jake D. Johnson, Cyril Bernerd, Frank Bruchertseiffer, et al. Supplementary material: Ac-227 Content of mass separated Ac-225 samples from proton spallation of thick Th-based targets at CERN-MEDICIS. *Supplementary Material*, 2024.

[77] Eduardo Galiano and Matthew Rodrigues. A comparison of different analytical methods of determining the solid angle of a circular coaxial source–detector system. *Applied Radiation and Isotopes*, 64(4):497–501, 2006.

[78] Julien Michaud. Separators, Mass Separation on Radionuclides. Presentation at PRISMAP Summer School, May 2024. Slide 24: Spectrometer Resolution.

[79] CAEN. *Electronic instrumentation, Register Description and Data Format*, 2020. User Manual UM5407.

Appendices

A. Alpha spectrometry

Below, extra information can be found about the alpha spectrometry measurement. The signal processing of the digitizer is influenced by various parameters, which can be adjusted using the Compass software for data display. Table A.1 explains the parameters for the timing branch, while table A.2 details those for the energy branch of the digitizer. In table ?? and ??, concrete values are given for each experimental run.

Table A.1: Explanation of input parameters of the timing branch, which influences the shape of the bipolar signal. These parameters could be adjusted in the software Compass.

Parameter	**Explanation**
Threshold	Minimum energy required for registration/trigger of a timestamp.
Trigger holdoff	Dead time interval where no other signals are accepted.
Fast discriminator smoothing	Smoothes the waveform signal generated. Increasing the number of samples results in stronger smoothing.
Input rise time	Determines the duration of the two 'Gaussians' of the bipolar shape. Ideally, it should be kept low, but not too low to ensure the formation of a well-shaped waveform.

Table A.2: Explanation of the input parameters of the energy branch, which determines the shape of the trapezoid and the sampling for binning. These parameters could be adjusted in the software Compass.

Parameter	**Explanation**
Trap rise time	Determines the width of the time windows.
Trap flat top	Specifies the distance between the two windows, affecting the top surface of the trapezoid.
Trap pole zero	Corrects the exponential decay of the input signal, ensuring the top surface of the trapezoid remains flat.
Peaking time	Specifies when to smaple values from the top surface. Since there are signal ripples (ringing) at the beginning of the input signal, it is best to take values late in the top surface to associate an energy value with the signal.
N samples peak	Specifies the number of values to take from the top surface, giving an average value of the height.
Peak holdoff	Defines how close two trapezoids must be to be considered pilled-up. Starts at the end of the flat top. [79]

Table A.3: Values of the parameters used for the first and second Ac-227 samples.

Parameter	**First Sample (December)**	**Second Sample (May)**
Trap. rise time	1500.0	2400.0
Trap. flat top	300.0	1200.0
Trap. pole zero	194000.0	194000.0
Peaking time	80.0	80.0
N samples peak	1	4
Peak holdoff	960.0	960.0
Energy fine gain	4.0	4.0
Threshold	100.0	100.0
Trigger holdoff	200.0	496.0
Fast Discriminator smoothing	4	8
Input rise time	50.0	16.0
Voltage bias	60	60

A.1 Poster ISMERAD conference

On the next page, the poster is shown which was used for the 9th symposium of the ISMERAD conferrence.

Purity Analysis of Ac-225 Production at CERN-MEDICIS

M. Keppens[1], J. Johnson[1], C. Bernerd[2], F. Bruchertseiffer[3], T.E. Cocolios[1], M. Deseyn[1], C. Duchemin[2], L. Lambert[2], R. Mancheva[1,2], R. Rossel[2], T. Stora[2]
[1]KU Leuven, [2]CERN, [3]JRC
Max.keppens@student.kuleuven.be

Ac-225 purpose: TAT

Targeted alpha therapy (TAT) is a promising and innovative approach to fight cancer. In this type of therapy, a radio-pharmaceutical is injected into the human body that binds selectively to tumor cells, which reduces the damage to healthy tissue.

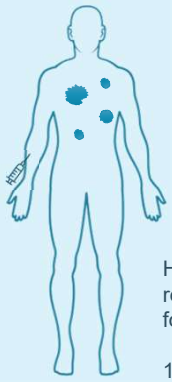

As Ac-225 has four alpha emissions in its decay chain, the isotope is highly cytotoxic, which makes it a promising candidate for TAT.

However, two main factors render the ongoing research for this isotope difficult:

1. production capability
2. contamination of co-produced isotopes

CERN-MEDICIS facility

CERN-MEDICIS (MEDical Isotopes Collected from ISolde) is a facility dedicated to produce novel radioisotopes for medical imaging and treatment.

- Extension of the ISOLDE (Isotope Separator OnLine DEvice) facility at CERN, which receives 1,4 GeV proton beams
- MELISSA: a laser ion source lab to induce fingerprint-like atomic transitions
- A KUKA ® robot handles the highly radioactive targets
- 32 projects have been approved by the members of the MEDICIS collaboration board [3]

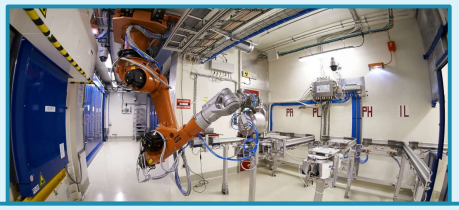

More info on the website!

Extraction isotopes

Target oven heated by putting a current through:

± 1400 °C → release of Ra-225
± 2250 °C → release of Ac-225

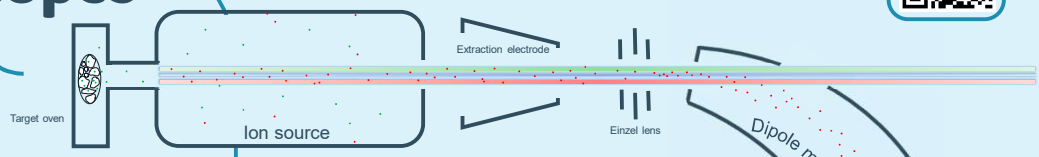

Target is externally prepared:
- JRC prepared target 1 with known ratios of $^{225}_{89}Ac$ and $^{227}_{89}Ac$
- Target 2 was irradiated at ISOLDE

Isotopes effuse out of the target to the ion source:
1. Surface ionization
2. Laser ionization (3 lasers)

An extraction electrode draws the ions out of the ion source (typically 60 kV).

The ion beam is focussed by an Einzel lens and mass seperated by a dipole magnet.

The goal is to filter out Ac-225 from the target. A typical contaminant is Ac-227, which is the focus of this work [4]. The separation enhancement factor (spf) quantifies:

$$spf = \frac{\left(\frac{^{225}Ac}{^{227}Ac}\right)_{\text{end}}}{\left(\frac{^{225}Ac}{^{227}Ac}\right)_{\text{start}}}$$

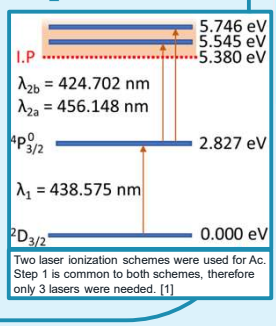

Two laser ionization schemes were used for Ac. Step 1 is common to both schemes, therefore only 3 lasers were needed. [1]

Quality control

Retrieved 2 foils for KU Leuven

$t_{\frac{1}{2}} {}^{225}_{89}Ac = 9{,}92$ d ⟷ $t_{\frac{1}{2}} {}^{227}_{89}Ac = 21{,}77$ y

→ Fraction Ac-225 remaining after decay: Foil 1: $9{,}07 \cdot 10^{-10}$, Foil 2: $4{,}21 \cdot 10^{-9}$
→ Ac-227 still measurable

Using alpha spectroscopy, prominent peaks of the daughter nuclei could be identified. Using the Bateman equation [2]:

$$N_n(t) = \frac{N_1(0)}{\lambda_n} \sum_{i=1}^{n} \lambda_i \alpha_i \exp(-\lambda_i t) \text{ with}$$

$$\alpha_i = \prod_{i=1, j \neq i}^{n} \frac{\lambda_j}{\lambda_j - \lambda_i},$$

the initial activity (end of collection) could be estimated of Ac-227 and the separation enhancement factor of the seperator.

	$A_{initial}$ of Ac-227 [Bq]	Separation enhancement factor
Foil 1	4.33 ± 0.36	$122{,}8 \pm 12{,}3$
Foil 2	0.28 ± 0.02	$546{,}0 \pm 122{,}8$

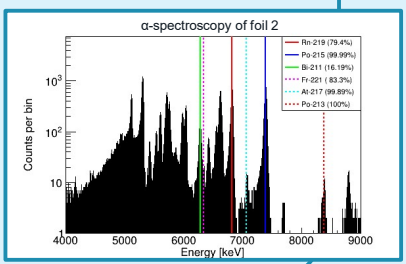

Conclusion

- Resonant ionization and mass separation effectively reduce Ac-227 contamination, but the separation factor varies between extraction runs.
- Separation enhancement factors are consistent with other quantification methods.
- Other contaminants are present in the foils (Ra-226, Po-208).

References

[1] Johnson, J. D., Heines, M et.al. (2023). Resonant laser ionization and mass separation of Ac-225. *Scientific Reports, 13*(1). https://doi.org/10.1038/s41598-023-28299-4
[2] Celnar, J. (2006). General solution of Bateman equations for nuclear transmutations. Annals of Nuclear Energy, 33(7), 640–645. https://doi.org/10.1016/j.anucene.2006.02.004
[3] MEDICIS, Overview of the CERN-MEDICIS facility, https://medicis.cern/overview-of-the-MEDICIS-facility
[4] ollefson, A. D., Smith, C. M et. al. (2021). Measurement of 227Ac impurity in 225Ac using decay energy spectroscopy. Applied Radiation and Isotopes, 172, 109693–109693. https://doi.org/10.1016/j.apradiso.2021.109693

B. MEDICIS data

Below, more information, figures and tables are given about the ion beam current analysis.

Table B.1: The data from a CERN-MEDICIS run used for analysis.

Name	Unit	Information
timestamp	year-month-day + time of day	Timestamp objects, corresponding to the time of the data below. $\Delta t = 0.5$ s
BX40/60	Ampère [A]	Current measured on the collimator/foil
FC30/FC70	Ampère [A]	Current measured in Faraday cup (FC) before (FC70) and after (FC30) the mass separator.
FC30/FC70 Position	-	Position of the Faraday cup: $0 \rightarrow$ FC out $1 \rightarrow$ FC in $2 \rightarrow$ FC moving
Line/Target I_{MEAS}	Ampère [A]	Current through the transfer line or target container for heating
Line/Target V_{MEAS}	Voltage [V]	Voltage difference over the transfer line or target container

B.1 Error determination

When a function is sampled at discrete time points, the integral of the function can be approximated using the trapezoidal rule. If the function values and their associated errors are known, the error propagation in the integral can be calculated. Let's consider the trapezoidal integration of the difference between two arrays: one from the experimental ion beam current data with errors (y_{up}) and one from a polynomial fit with parameter errors (y_{down}). The trapezoidal integral is given by

$$I = \sum_{i=0}^{N-1} \frac{(y_{\mathrm{up},i} - y_{\mathrm{down},i} + y_{\mathrm{up},i+1} - y_{\mathrm{down},i+1})}{2} \Delta t, \tag{B.1}$$

where Δt is the time step between adjacent data points. The polynomial fit of the background current provides a set of coefficients $\mathbf{a} = [a_0, a_1, a_2, ..., a_n]$ and their covariance matrix **pcov**. The fitted values at time t are given by

$$y_{\text{down}}(t) = \sum_{i=0}^{n} a_i t^i. \tag{B.2}$$

To propagate the errors from the polynomial fit parameters to the fitted values, the following equation is used

$$\sigma^2_{y_{\text{down}}}(t) = \sum_{i=0}^{n}\sum_{j=0}^{n}\left(\frac{\partial y_{\text{down}}(t)}{\partial a_i}\frac{\partial y_{\text{down}}(t)}{\partial a_j}\right)\text{pcov}[i,j], \tag{B.3}$$

where

$$\frac{\partial y_{\text{down}}(t)}{\partial a_i} = t^i. \tag{B.4}$$

This means that

$$\sigma^2_{y_{\text{down}}}(t) = \sum_{i=0}^{n}\sum_{j=0}^{n}(t^i \cdot t^j \cdot \text{pcov}[i,j]). \tag{B.5}$$

The total error in the difference $\Delta y = y_{up} - y_{down}$ at each time point is

$$\sigma_{\Delta y} = \sqrt{\sigma^2_{y_{\text{up}}} + \sigma^2_{y_{\text{down}}}}. \tag{B.6}$$

The error on y_{up} is determined by considering the release of particles as a stochastic process and the precision of the PAM (which was considered to be 0.5 pA). The number of ions N impinging on the collection foil is then approximated as a Poisson distribution, meaning that the error on the number of ions is given by $\sqrt{N}$. The current y_{up} is then correlated with the number of ions by

$$y_{up} = \frac{N \cdot e}{\Delta t} \tag{B.7}$$

The error is then determined by propagating the error from the equation above and the precision of the PAM. The integral's error is propagated using the errors in the differences and the time step. The trapezoidal rule for the integral's error includes the error in Δt:

$$\sigma_I^2 = \sum_{k=0}^{N-1}\left(\frac{\sigma^2_{\Delta y,k} + \sigma^2_{\Delta y,k+1}}{4}\Delta t^2\right) + \sum_{k=0}^{N-1}\left(\frac{\Delta y_k + \Delta y_{k+1}}{2}\right)^2 \sigma^2_{\Delta t}, \tag{B.8}$$

where $\sigma_{\Delta t}$ is the error in the time step. Error propagation for an exponential and linear interpolation is done similar. The error on $y_{\text{down}}(t)$ for linear interpolation is simply 0.5 pA.

B.2 Activity determination

Below, the figures are given showing the background fit and the corresponding values for the determination of the activity for the June run and September.

Table B.2: Summary of collected charges and activity when collecting Ra-225 using polynomial fits and linear interpolation in June. Figure B.1 shows the background fits.

Background	Charge Collected [µC]	Activity [MBq]	χ^2_ν
Polynomial 0	7.5279 ± 0.0001	20.6703 ± 0.0002	0.2399
Polynomial 1	7.5606 ± 0.0001	20.7582 ± 0.0004	0.1190
Polynomial 2	7.5522 ± 0.0054	20.7358 ± 0.0148	0.0197
Polynomial 3	7.5572 ± 0.7109	20.7494 ± 1.9657	0.0192
Linear interpolation	7.5413 ± 0.0001	20.7065 ± 0.0002	0.0160

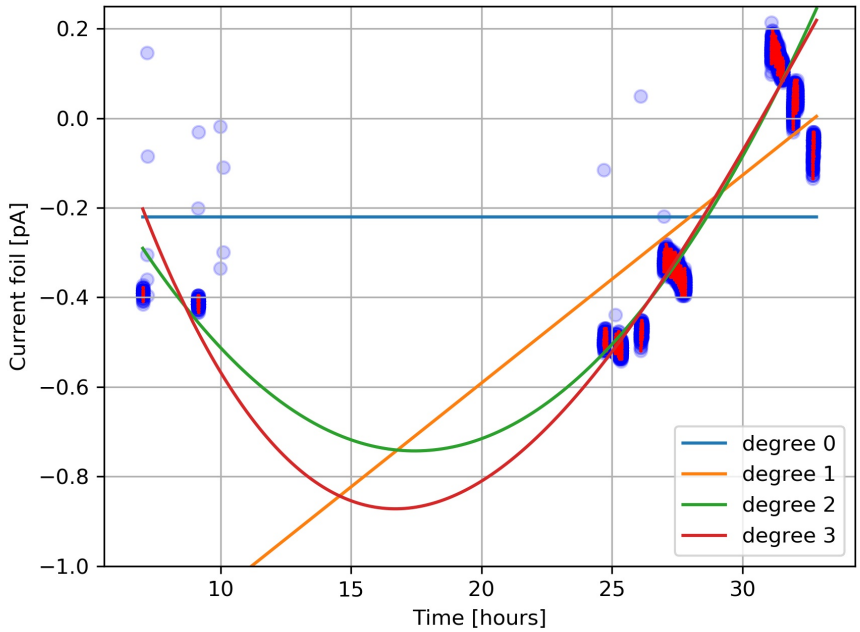

Figure B.1: Ion beam current on the foil over time during the collection of Ra-225 on foil MS-022. The red dots indicate the moments when a Faraday cup (FC) is in use. These points were fitted using multiple polynomials and an exponential. The results are shown in table B.2.

Table B.3: Summary of collected charges and activity when collecting Ac-225 using polynomial fits and linear interpolation. Figure B.2 shows the background fits.

Background	Charge Collected [µC]	Activity [MBq]	χ^2_ν
Polynomial 1	0.5565 ± 0.0004	2.3890 ± 0.0016	0.3053
Polynomial 2	0.5570 ± 0.1278	2.3514 ± 0.6034	0.0213
Exponential	0.5622 ± 0.0001	2.3808 ± 0.0006	0.0356
Interpolation	7.5413 ± 0.0001	2.5334 ± 0.0006	-

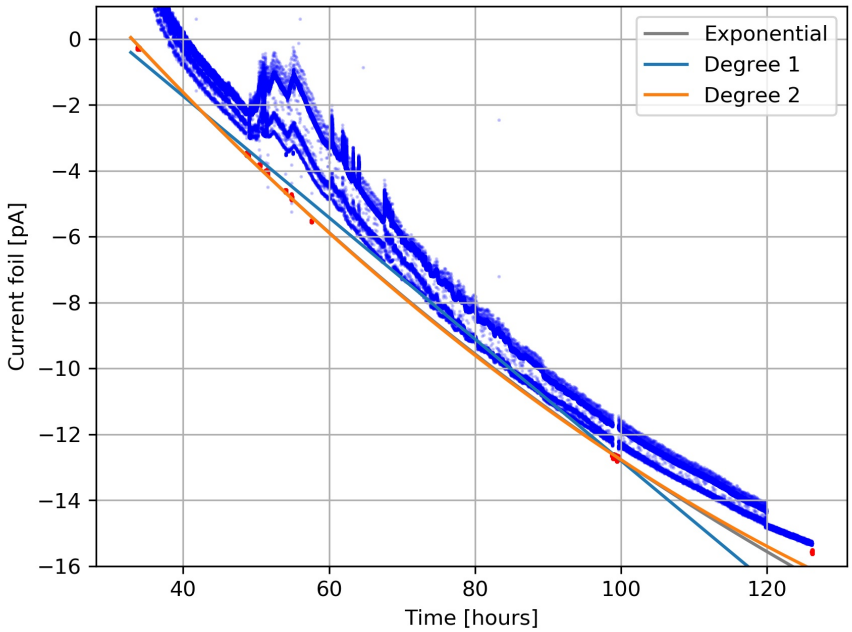

Figure B.2: Ion beam current on the foil over time during the collection of Ac-225 on foil MS-022. The red dots indicate the moments when a Faraday cup (FC) is in use. These points were fitted using multiple polynomials and an exponential. The results are shown in table B.3.

Table B.4: Summary of collected charges and activity when collecting Ra-224 on foil MS-020 using polynomial fits and linear interpolation in the June run.

Background	Charge Collected [µC]	Activity [MBq]	χ^2_ν
Polynomial 0	0.0037 ± 0.0000	19408.4 ± 50.7370	0.000317
Polynomial 1	0.0037 ± 0.0002	19306.0 ± 1252.0000	0.000142
Polynomial 2	0.0037 ± 0.1286	19319.0 ± 669420.0000	0.000141
Interpolation	0.0037 ± 0.0000	19282.0 ± 50.6790	-

Table B.5: Summary of collected charges and activity when collecting Ac-225 on foil M-288 using polynomial fits and linear interpolation in the June run. Figure B.3 shows the background fits.

Background	Charge Collected [µC]	Activity [MBq]	χ^2_ν
Polynomial 0	0.0358 ± 0.0000	145010.0 ± 106.9800	0.1642
Polynomial 1	0.0328 ± 0.0029	132780.0 ± 11933.0000	0.003225
Polynomial 2	0.0327 ± 7.8379	$132460.0 \pm 31739000.0000$	0.003048
Linear interpolation	0.0328 ± 0.0000	132650.0 ± 106.9000	-

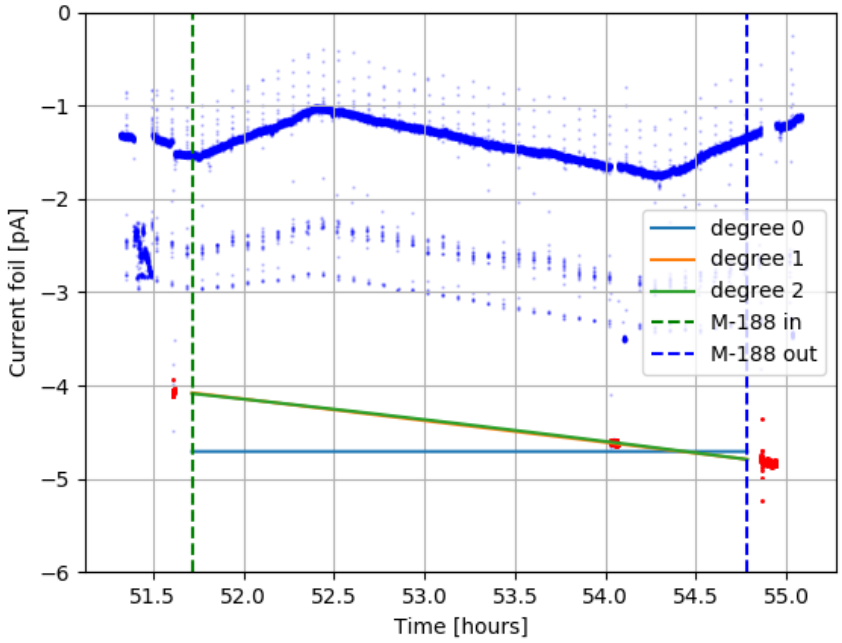

Figure B.3: Ion beam current is plotted against time when Ac-225 was collected on foil MS-288 in the June run. The red dots denote the moment when a FC is in, which were fitted by multiple polynomials and an exponential. Results are shown in table B.5.

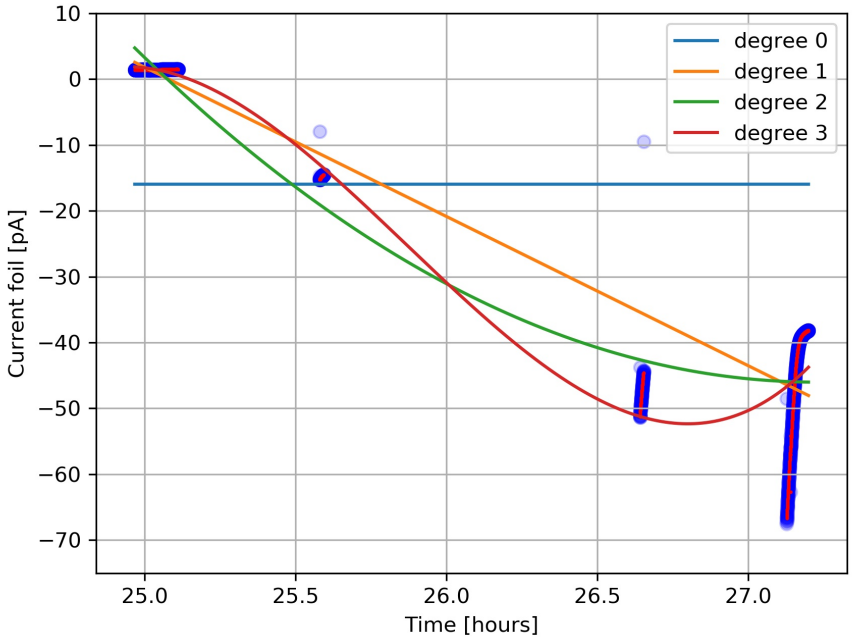

Figure B.4: Ion beam current is plotted against time when Ra-224 was collected on foil MS-035 in the September run. The red dots denote the moment when a FC is in, which were fitted by multiple polynomials and an exponential. Results are shown in table B.6.

Table B.6: Summary of collected charges and activity when collecting Ra-224 on foil MS-035 using polynomial fits and linear interpolation in the September run. Figure B.4 shows the fits.

Background	Charge Collected [µC]	Activity [MBq]	χ^2_ν
Polynomial 0	1.4363 ± 0.0000	10.1506 ± 0.0002	2070.687
Polynomial 1	1.4909 ± 0.0004	10.5410 ± 0.0027	134.5471
Polynomial 2	1.5403 ± 0.9387	10.8909 ± 6.6449	106.6255
Polynomial 3	1.5486 ± 1.0644	10.9505 ± 7536.9000	77.8703
Interpolation	1.5527 ± 0.0000	10.9801 ± 0.0002	-

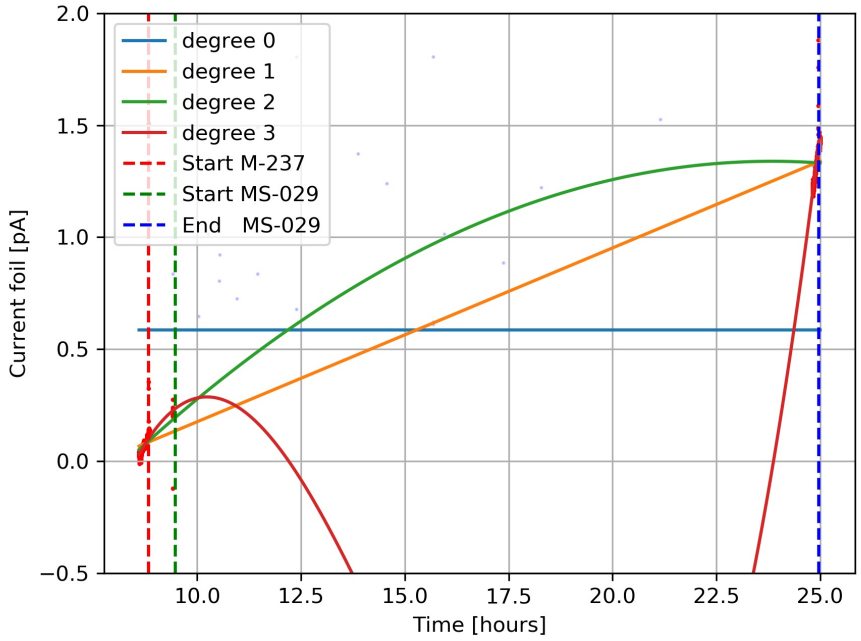

Figure B.5: Ion beam current on the foil over time during the first collection of Ra-225 on foils M-237 and MS-029 in the September run. The red dots indicate the moments when a Faraday cup (FC) is in use. These points were fitted using multiple polynomials and an exponential. The results are shown in tables B.7 and B.8.

Table B.7: Summary of collected charges and activity when collecting Ra-225 on foil M-237 using polynomial fits and linear interpolation for the first time interval in the September run. Figure B.5 shows the fits.

Background	Charge Collected [µC]	Activity [MBq]	χ^2_ν
Polynomial 0	0.0703 ± 0.0000	0.1941 ± 0.0000	1.6378
Polynomial 1	0.0713 ± 0.0000	0.1968 ± 0.0000	0.1285
Polynomial 2	0.0712 ± 0.0015	0.1967 ± 0.0049	0.1278
Polynomial 3	0.0711 ± 0.0419	0.1965 ± 0.1407	0.1175
Interpolation	0.0711 ± 0.0000	0.1964 ± 0.0000	-

Table B.8: Summary of collected charges and activity when collecting Ra-225 on foil MS-029 using polynomial fits and linear interpolation for the first time interval in the September run. Figure B.5 shows the fits.

Background	Charge Collected [µC]	Activity [MBq]	χ^2_ν
Polynomial 0	3.8534 ± 0.0001	10.8584 ± 0.0002	1.6378
Polynomial 1	3.8455 ± 0.0001	10.8359 ± 0.0002	0.1285
Polynomial 2	3.8316 ± 0.0317	10.7970 ± 0.0894	0.1278
Polynomial 3	3.9381 ± 2.1085	11.0972 ± 5.9686	0.1175
Interpolation	3.8456 ± 0.0001	10.8363 ± 0.0002	-

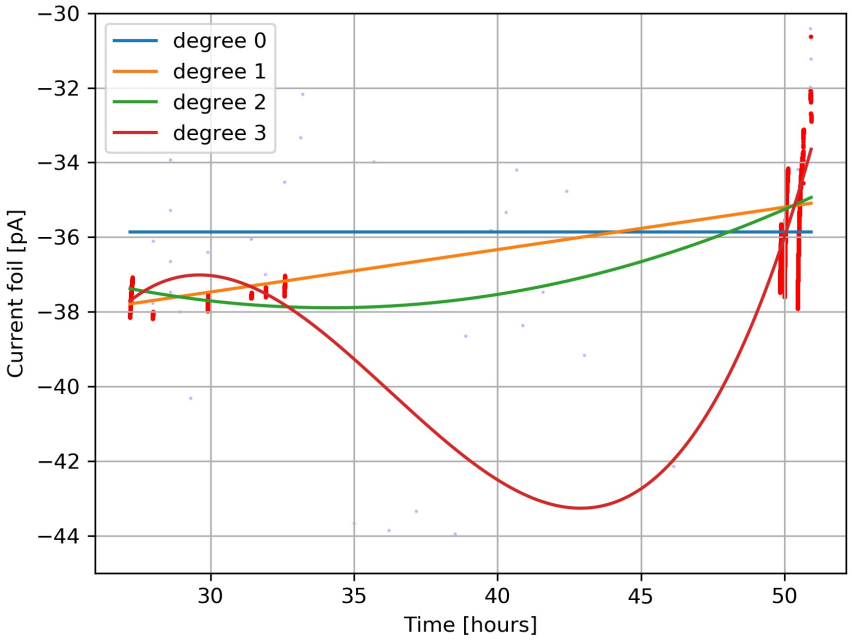

Figure B.6: Ion beam current is plotted against time when Ra-225 was collected on foil M-237 and MS-029 for the second time in the September run. The red dots denote the moment when a FC is in, which were fitted by multiple polynomials and an exponential. Results are shown in table B.9 and B.10.

Table B.9: Summary of collected charges and activity when collecting Ra-225 on foil MS-029 second time using polynomial fits and linear interpolation for the second time interval in the September run. Figure B.6 shows the fits.

Background	Charge Collected [µC]	Activity [MBq]	χ^2_ν
Polynomial 0	12.4280 ± 0.0001	36.3914 ± 0.0002	9.6856
Polynomial 1	12.4780 ± 0.0002	36.5370 ± 0.0007	4.8753
Polynomial 2	12.5390 ± 0.1103	36.7142 ± 0.3253	4.6100
Polynomial 3	12.7750 ± 33.7600	37.4098 ± 99.8750	3.2399
Interpolation	12.5511 ± 0.0001	36.7520 ± 0.0002	-

Table B.10: Summary of collected charges and activity when collecting Ra-225 on foil M-237 using polynomial fits and linear interpolation for the second time interval in the September run. Figure B.6 shows the fits.

Background	Charge Collected [µC]	Activity [MBq]	χ^2_ν
Polynomial 0	0.1175 ± 0.0000	0.3518 ± 0.0000	9.6856
Polynomial 1	0.1167 ± 0.0000	0.3494 ± 0.0001	4.8753
Polynomial 2	0.1166 ± 0.0194	0.3491 ± 0.0653	4.6100
Polynomial 3	0.1156 ± 6.9612	0.3463 ± 23.3780	3.2399
Interpolation	0.1143 ± 0.0000	0.3422 ± 0.0000	-

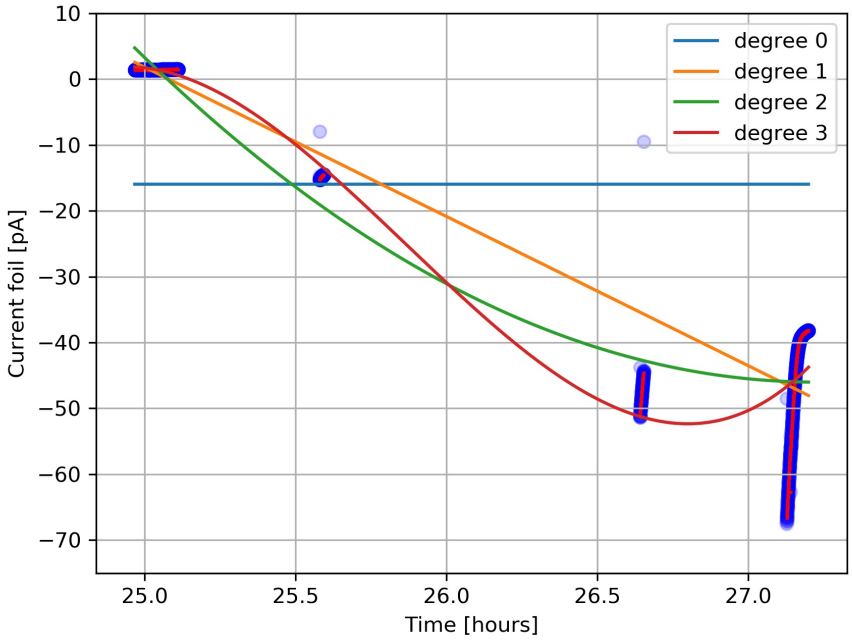

Figure B.7: Ion beam current is plotted against time when Ra-225 was collected on foil MS-029 for the third time in the September run. The red dots denote the moment when a FC is in, which were fitted by multiple polynomials and an exponential. Results are shown in table B.11.

Table B.11: Summary of collected charges and activity when collecting Ra-225 on foil MS-029 using polynomial fits and linear interpolation for the third time interval in the September run. Figure B.7 shows the fits.

Background	Charge Collected [µC]	Activity [MBq]	χ^2_ν
Polynomial 0	9.0481 ± 0.0001	27.7085 ± 0.0003	70.5996
Polynomial 1	8.4241 ± 0.0005	25.8399 ± 0.0017	4.2537
Polynomial 2	8.6162 ± 0.3255	26.4198 ± 1.0488	2.3430
Polynomial 3	8.6262 ± 133.8600	26.4473 ± 434.1400	1.8302
Interpolation	9.0045 ± 0.0001	27.6241 ± 0.0003	-

B.3 Fits of Laser OFF data

Below, figures are given regarding the empirical fits of the laser off states for the run of May and June.

Table B.12: The χ^2_ν values of the different empirical fits of the laser off data of the first region of the May run.

fit-function	χ^2_ν
exponential	5.49
polynomial degree 0	2080
polynomial degree 1	60.9
polynomial degree 2	9.79
polynomial degree 3	4.45
polynomial degree 4	3.84
polynomial degree 5	3.81

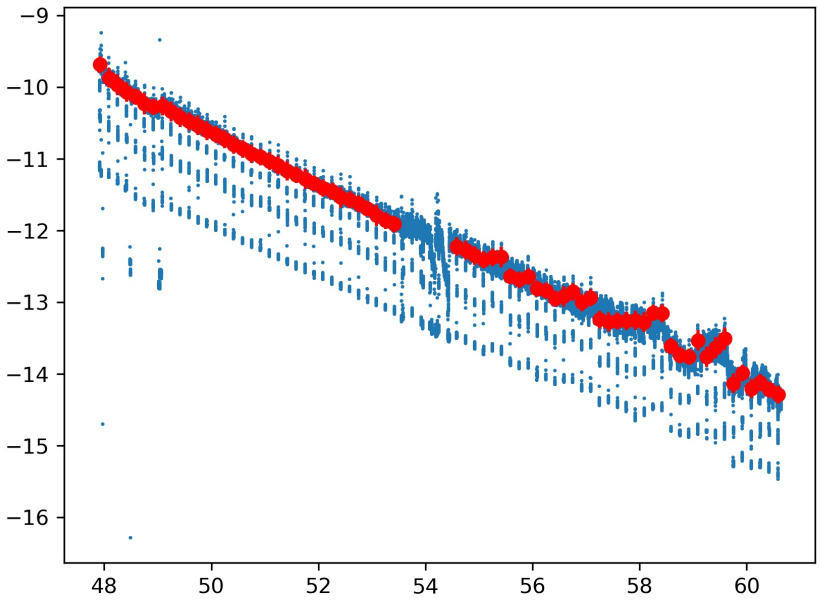

Figure B.8: The data points of the laser off states of the third region of the run in May, which were empirically fitted.

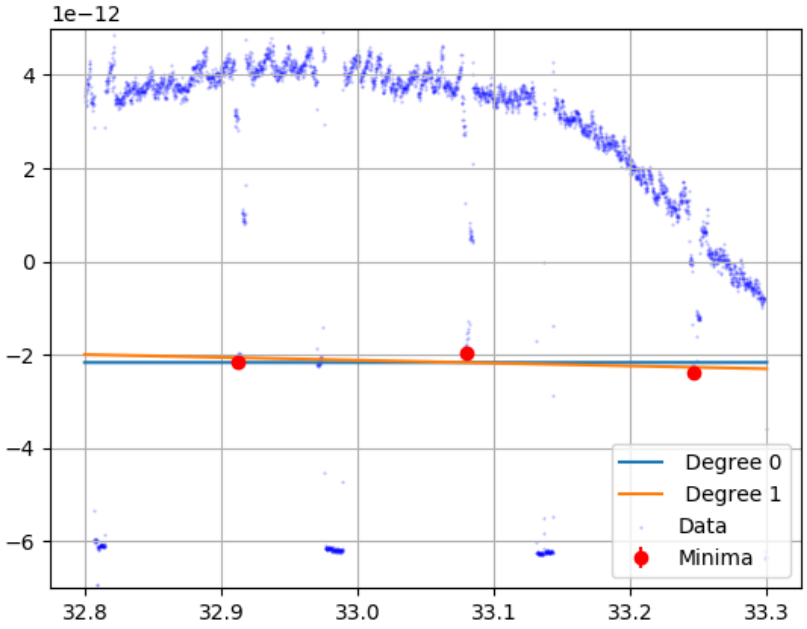

Figure B.9: The data points of the laser off states of foil M-233 of the run in May, which were empirically fitted.

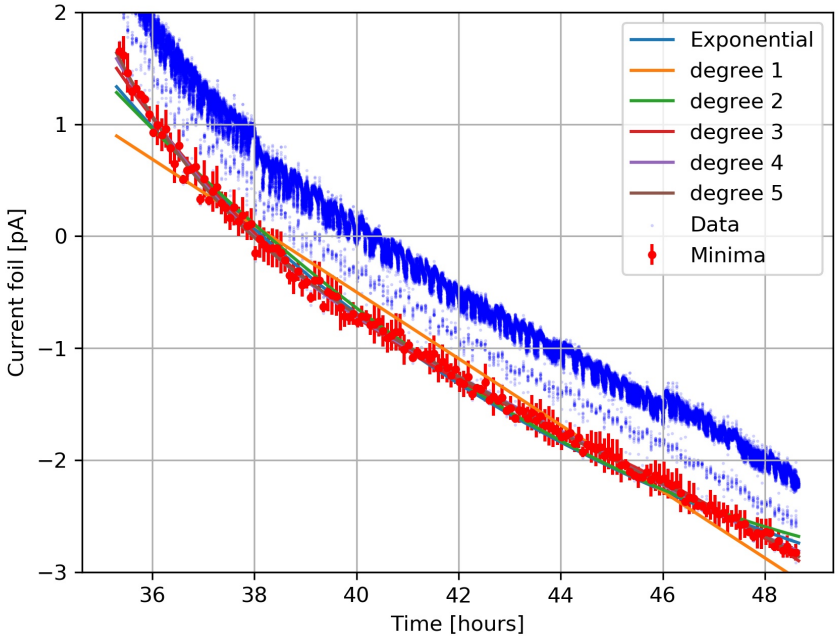

Figure B.10: The data points of the laser off states of the first region of the run in June, which were empirically fitted.

Table B.13: The χ^2_ν values of the different empirical fits of the laser off data of the first region of the June run. Fits visualized in figure B.11.

fit-function	χ^2_ν
exponential	1.54
polynomial degree 1	7.93
polynomial degree 2	2.09
polynomial degree 3	0.983
polynomial degree 4	0.807
polynomial degree 5	0.740

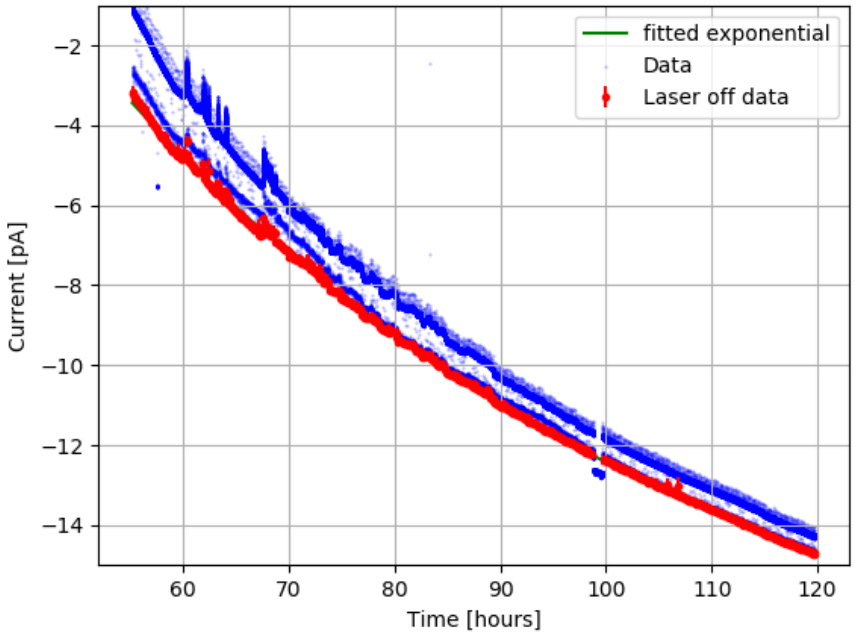

Figure B.11: The data points of the laser off states of the second region of the run in June, which were empirically fitted.

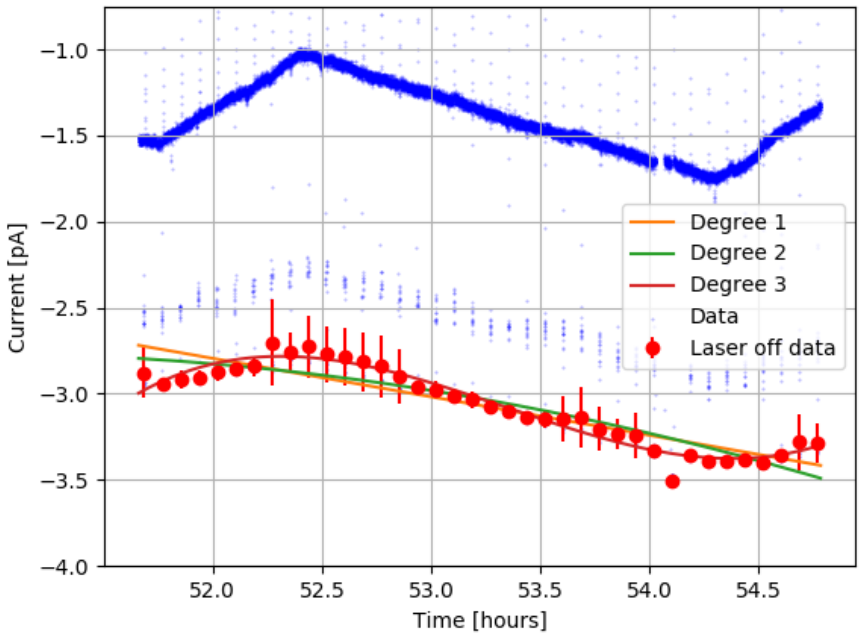

Figure B.12: The data points of the laser off states for foil M-288 in the June run, which were empirically fitted.

B.4 Apparent laser enhancement

Below, all the data points for the remaining regions are shown for the determination of the apparent laser enhancement.

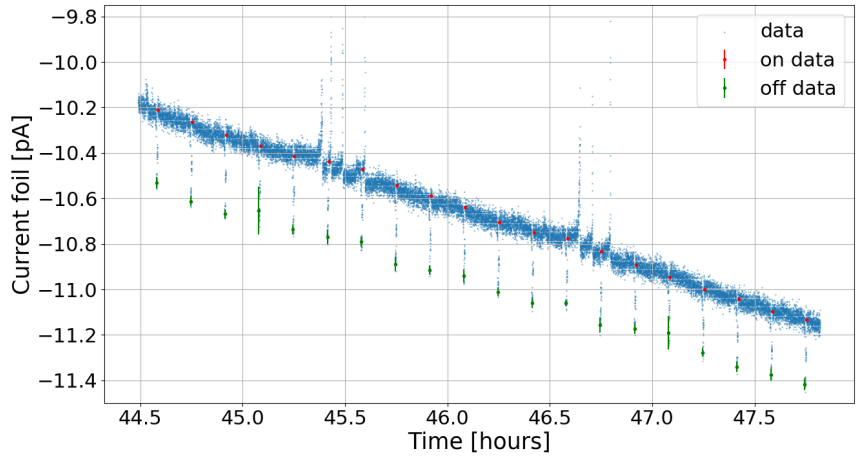

Figure B.13: The data points of the second region used to determine the apparent laser enhancement (see equation 4.14) of the run of May.

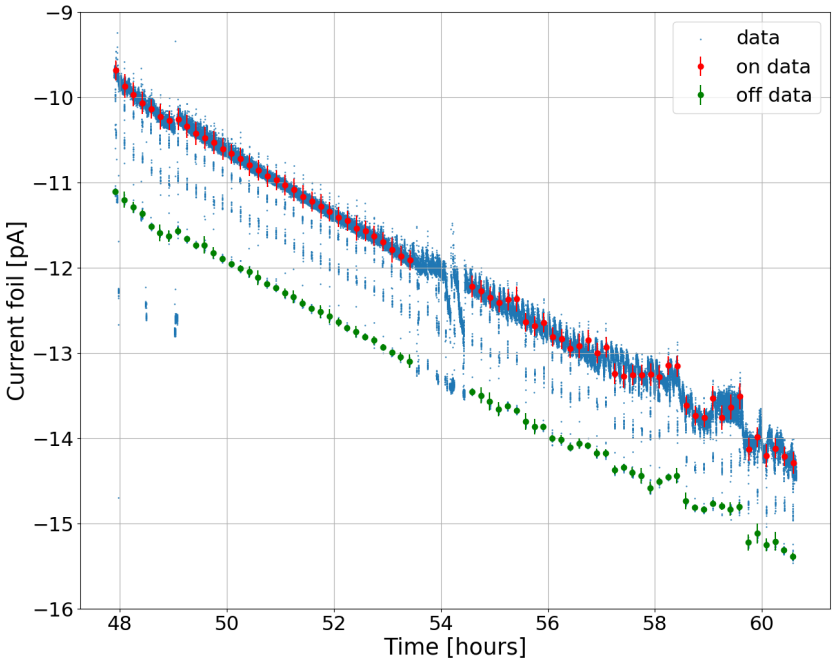

Figure B.14: The data points of the third region used to determine the apparent laser enhancement (see equation 4.14) of the run of May.

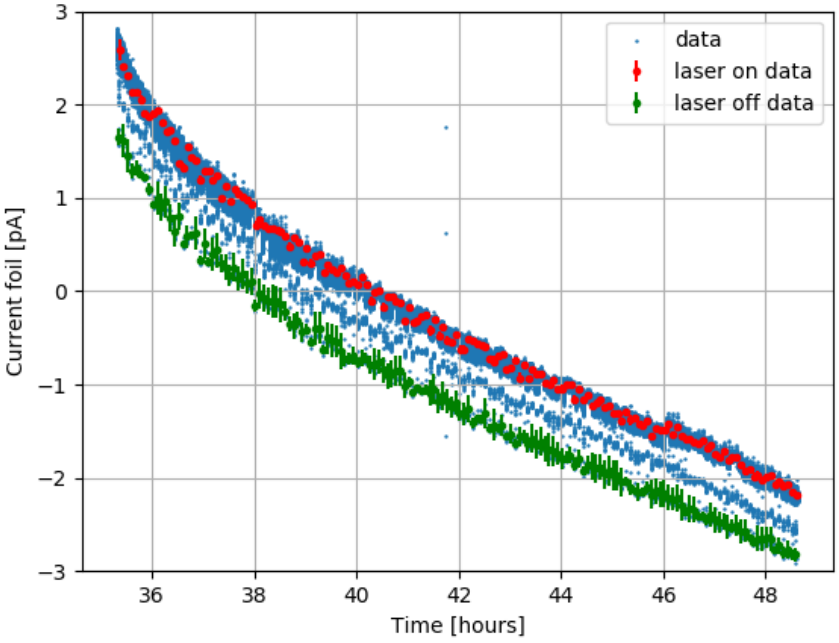

Figure B.15: The data points of the first region used to determine the apparent laser enhancement (see equation 4.14) of the June run.

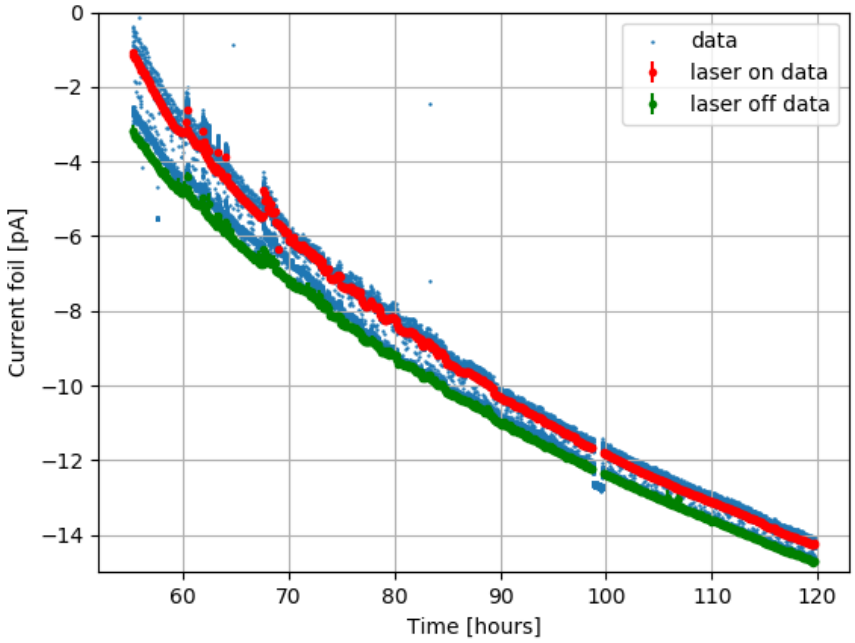

Figure B.16: The data points of the second region used to determine the apparent laser enhancement (see equation 4.14) of the June run.

Institute for nuclear and radiation physics
Celestijnenlaan 200D
3000 LEUVEN, BELGIE
tel. + 32 16 32 72 63
www.kuleuven.be